

UC Berkeley

UC Berkeley Electronic Theses and Dissertations

Title

Flexographically Printed Rechargeable Zinc-based Battery for Grid Energy Storage

Permalink

<https://escholarship.org/uc/item/3874c19s>

Author

Wang, Zuoqian

Publication Date

2013

Peer reviewed|Thesis/dissertation

Flexographically Printed Rechargeable Zinc-based Battery for Grid Energy Storage

by

Zuoqian Wang

A thesis submitted in partial satisfaction of the

Requirements for the degree of

Doctor of Philosophy

in

Engineering – Mechanical Engineering

in the

GRADUATE DIVISION

of the

UNIVERSITY OF CALIFORNIA, BERKELEY

Committee in charge:

Professor Paul K. Wright, Chair

Professor James W. Evans

Professor David A. Dornfeld

Spring 2013

Flexographically Printed Rechargeable Zinc-based Battery for Grid Energy Storage

Copyright 2013

by

Zuoqian Wang

Abstract

Flexographically Printed Rechargeable Zinc-based Battery for Grid Energy Storage

by

Zuoqian Wang

Doctor of Philosophy in Engineering - Mechanical Engineering

University of California, Berkeley

Professor Paul K. Wright, Chair

This study examines the feasibility of utilizing traditional flexographic printing technology for large-scale zinc-based battery manufacturing for grid energy storage applications. The design and development of functional flexographic inks is the main goal of this study. Printed battery electrochemical performance is also a focus area.

Long-life, energy dense, cost effective electrochemical energy storage systems for power grid applications have become a fast-emerging industry in recent decades. Grid energy storage is widely regarded as an important component of the smart grid, because of its potential role in complementing intermittent renewable energy sources. However, battery technologies have not improved much over the past few decades. Both new battery chemistries and fabrication processes are needed to significantly reduce battery cost and to allow for easy integration with renewables.

Printable batteries were designed based on fundamental electrochemical principles governing the battery performance, including thermodynamics, reaction kinetics as well as transport properties. With cost and application factors taken into account, practical battery system design criteria were also summarized with regard to battery geometry, chemistry and fabrication technology.

A survey of current main printing technologies was conducted. Based on the criteria developed for functional printing process design and selection, a comparison of the technologies was made and a roll-to-roll flexographic printing process for rechargeable zinc-based battery manufacturing was proposed. Based on the fundamental operating mechanism of flexography, key criteria for developing functional flexographic printing inks were established, including composite ink rheology (steady-state viscosity and yield stress), ink wettability as well as ink dispersing qualities. The ink viscosity significantly influences the ink transfer efficiency while the yield stress critically determines its structural integrity once transferred on flexible substrate. The ink wettability indicates the ink spreading properties and film uniformity while the ink dispersing quality affects the ink homogeneity from before printing through the printing process. A variety of MnO_2 cathode inks were formulated and analyzed based on these criteria. A novel type of aqueous cathode ink based on PSBR polymeric binder showed excellent flexographic printability.

Extensive electrochemical characterizations with the flexographically printed PSBR-based composite MnO_2 cathode were then conducted. Full cells consisting of dispenser-printed

electrolytes and zinc foil anodes were assembled. The cyclic voltammetry method was used to study the reversible zinc intercalation through ionic liquid electrolyte into the aqueous-based cathode. Galvanostatic cycling showed that the cell capacity stabilized after about twenty cycles and the capacity varied significantly with discharge current density. Electrochemical impedance spectroscopy measurements revealed the interfacial resistance between the gel electrolyte and zinc foil, as well as the evolution of impedance components through cycling, for a full zinc-based cell system. Coin cells based on zinc/ionic liquid electrolyte/MnO₂ chemistry were made in an inert argon environment and then characterized to study zinc-based chemistry performance in this controllable environment. The coin cells showed comparable behavior to batteries printed in the ambient environment. Printable PSBR-based nickel current collector inks have also been developed for an entirely printable zinc-based battery, to conveniently integrate with other electronics on non-conductive, flexible substrates.

An integrated energy-harvesting prototype was fabricated, which consisted of dispenser-printed thermoelectric energy harvesting and electrochemical energy storage devices with a commercial voltage step-up converter. Parallel-connected thermoelectric devices with low internal resistances were designed, fabricated and characterized. The use of a commercially available DC-to-DC converter was explored to step-up a 27.1mV input voltage from a printed thermoelectric device to a regulated 2.34V output. The voltage step-up circuit efficiency reached as maximum of 32.4% during the battery charging process while the battery charging efficiency was approximately 67%. The prototype presented in this study demonstrates the feasibility of deploying a printable, cost-effective and perpetual power solution for practical wireless sensor network applications. This work paves the path for potential integration of printable photovoltaic cell, zinc-based battery as well as relevant electronics for grid energy storage applications.

Dedication

The work is dedicated to my beloved parents, Huaixing Wang and Xiuduo Ma, and the whole family!

Table of Contents

Chapter 1 Introduction to Printed Rechargeable Zinc-based Battery for Grid Energy Storage.....	2
1.1. Introduction.....	2
1.2. Grid Energy Storage Technologies.....	3
1.3. Battery Operating Principles.....	5
1.4. Battery Design.....	7
1.4.1. Geometric Structure.....	8
1.4.2. Battery Chemistries.....	9
1.4.3. Fabrication.....	11
1.5. Printed Rechargeable Zinc-based Battery.....	13
1.6. Chapter Summary.....	15
Chapter References.....	16
Chapter 2 A Survey of Functional Printing Techniques for Scaled-up Battery Fabrication.....	19
2.1. Introduction To Printing Technologies.....	19
2.2. Battery Printing Technology Design and Selection.....	21
2.3. Chapter Summary.....	23
Chapter References.....	23
Chapter 3 Functional Flexographic Inks for Battery Electrode Fabrication: Printability.....	25
3.1. Introduction.....	25
3.2. Flexographic Printing Process and Ink Design.....	26

3.3. Aqueous Functional Inks.....	29
3.4. Ink Rheology.....	30
3.4.1. Ink Preparation and Rheological Measurements.....	30
3.4.2. Steady-state Viscosity.....	31
3.4.3. Yield Stress Measurement.....	33
3.5. Wetting Properties.....	35
3.5.1. Introduction.....	35
3.5.2. Surface Tension of Inks.....	36
3.5.3. Contact Angle Measurements.....	39
3.6. Ink Dispersing Qualities.....	41
3.7. Physical Characterizations of the Printed Films.....	43
3.7.1. Introduction.....	43
3.7.2. Printed Cathode Film Surface Profile and Roughness.....	44
3.8. Chapter Summary and Future Work.....	47
Chapter References.....	48

Chapter 4 Electrochemical Characterizations.....51

4.1. Introduction.....	51
4.2. Experimental.....	52
4.3. Reversible Zinc Ion Intercalation in the Flexographically Printed MnO ₂ Cathode.....	53
4.4. Galvanostatic Characterization of the Flexographically Printed MnO ₂ Cathode.....	56
4.4.1. Discharge Capacity.....	56
4.4.2. Galvnostatic Cyclability.....	57
4.4.3. Rate Performance.....	59
4.5. Electrochemical Impedance Spectroscopy.....	60

4.5.1. Introduction to Principles of AC Impedance Measurement.....	60
4.5.2. Interfacial Properties between Zinc and Gel Electrolyte.....	61
4.5.3. Impedance Analysis of the Assembled Full Cell.....	66
4.6. Zinc-based Battery Characterization in Controlled Environment.....	68
4.6.1. Introduction to Low Cell Yield and Performance Variations.....	68
4.6.2. Experimental for Making Coin Cells.....	70
4.6.3. Discharge Capacity and Rate Performance.....	70
4.6.4. Water Influence on the Coin Cell Performance.....	72
4.6.5. Current Collector Effect.....	73
4.7. Printable Current Collectors.....	73
4.7.1. Entirely Printed Zinc-based Battery.....	73
4.7.2. Optimization of the Printable Nickel Composite Ink.....	75
4.8. Chapter Summary and Future Work.....	78
Chapter References.....	78

Chapter 5 Integration of Printable Ultra-low-voltage Thermoelectric and Energy Storage Devices.....80

5.1. Introduction.....	80
5.2. Printed Thermoelectric Devices.....	81
5.2.1. Thermoelectric Device Design.....	81
5.2.2. Experimental.....	84
5.2.3. Thermoelectric Device Characterization.....	84
5.3. Dispenser Printed Micro-batteries on PCB.....	86
5.3.1. Printable Zinc-based Batteries.....	86
5.3.2. Fabrication.....	87

5.3.3. Printable Batteries Characterization.....	87
5.4. Integrated Energy Harvesting System.....	88
5.4.1. Power Management Introduction.....	88
5.4.2. Voltage Step-up Conversion.....	89
5.4.3. Printed Battery Charging.....	90
5.5. Chapter Summary and Future Work.....	91
Chapter References.....	92
Chapter 6 Discussion and Future Outlook.....	94
6.1. Printability.....	94
6.2. Electrochemistry.....	94
6.3. Applications	95

Acknowledgements

This Ph.D. study was made possible through financial support from California Energy Commission. I would like to thank all my colleagues and friends at Berkeley Manufacturing Institute, Department of Mechanical Engineering, Department of Material Science and Engineering, CITRIS, and Lawrence Berkeley National Lab for their kind help and support.

I would like to express my deepest gratitude to Professor Paul K. Wright and Professor James W. Evans, who have been wonderful advisors of me for five years. Only with their excellent guidance, constant encouragement and support, I was able to keep focusing on my Ph.D. research and get used to life in the United State. I want to thank Prof. David Dornfeld for serving in both my qualifying exam and Ph.D. dissertation committee.

I appreciate the generous help and guidance from Prof. Malcolm Keif and Prof. Xiaoying Rong at Cal Poly State University, San Luis Obispo. Many thanks to Dr. Vince Battaglia, who kindly supported my coin cell research at EETD, Lawrence Berkeley National Lab. I would like to acknowledge the contributions of Dr. Rei-Cheng Juang and Dr. Chun-Hsing Wu from ITRI to the study.

I want to especially thank Rich Winslow, Jay Keist, Christine Ho, Deepa Madan, Alic Chen, Bernard Kim and Mike Nill in the printer group. Without their kind help, the Ph.D. study would not be that easy for me.

I would like to thank my beloved parents and the whole family. Because of you, I never give up and keep working hard.

Finally, I want to express my great appreciation to my wife, Yu Liu. She has always been supportive and encouraging when I meet difficulties. I can't be luckier to have her in my life.

HYPOTHESIS

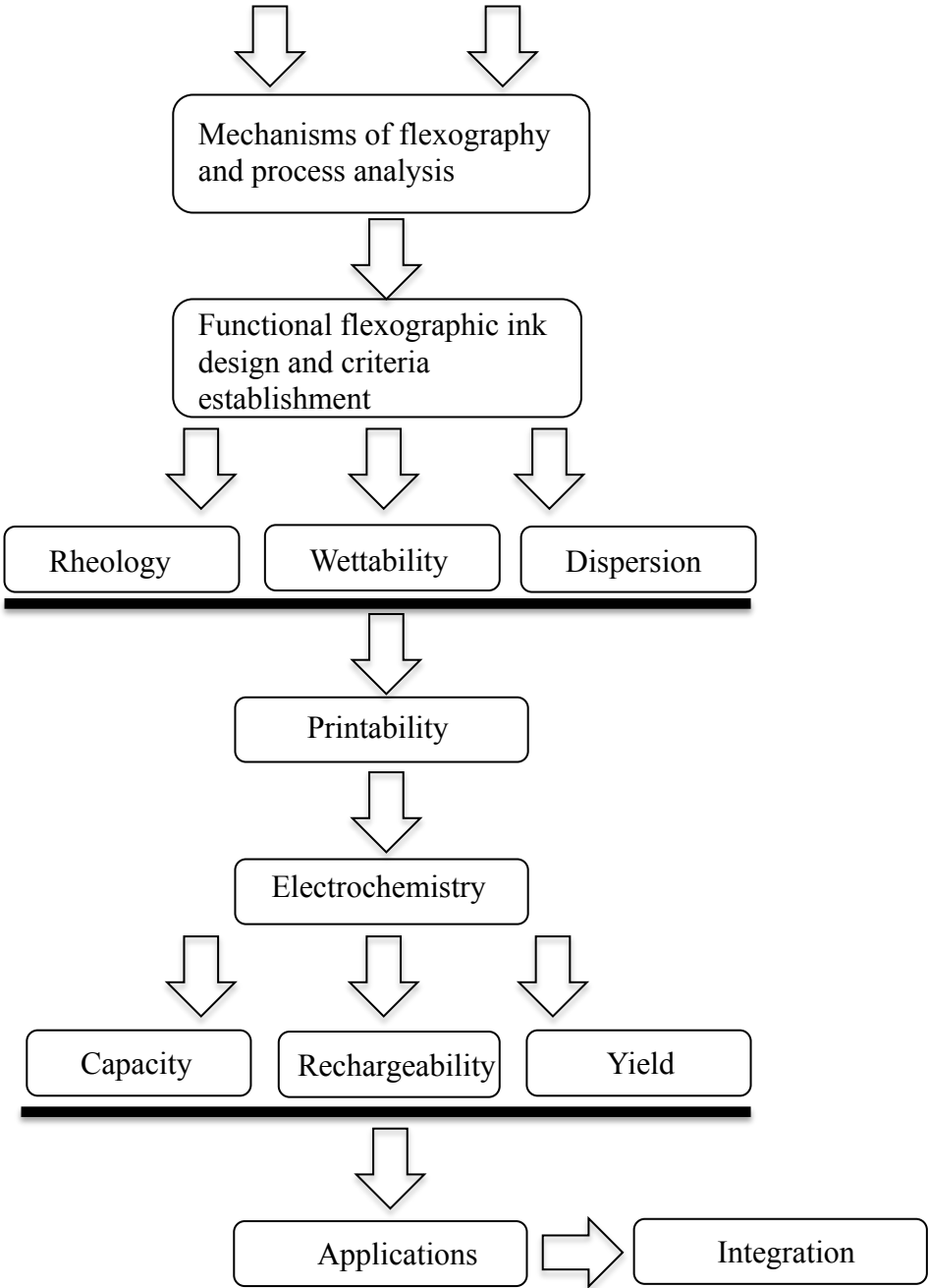
Zinc-based solid-state batteries can be fabricated using traditional flexographic printing technique for high throughput, cost effective energy storage manufacturing

BACKGROUND

Development of printable zinc-based battery chemistry

Available printing techniques and advantage of flexography

EXPERIMENT



CONCLUSIONS

Functional flexographic ink, developed from the fundamental operating mechanisms of flexography, achieved excellent printability as well as battery electrochemical performance.

Chapter 1

Introduction to Printed Rechargeable Zinc-based Battery for Grid Energy Storage

1.1. Introduction

Long-life, energy dense, low-cost, flexible electrochemical energy storage systems have become a fast-emerging industry in recent decades. In the wireless sensor network field, micro-batteries are needed to integrate with various energy harvesting devices to provide continuous power sources for reliable wireless sensor nodes applications[1]-[7]. In the portable electronics field, batteries have become the most significant obstacle to the availability of lighter, smaller consumer electronics, such as smart cell phones, tablet computers or traditional laptops. With the development of flexible electronics, such as flexible displays, flexible batteries are expected to become indispensable as power sources for fully flexible electronic systems. In the electric vehicle (EV) field, the performance of batteries will need to be improved and cost will need to be reduced significantly so that EVs can become competitive with traditional internal combustion engine vehicles. Currently, vehicle manufacturers entering this field are forced to choose between either the high-end luxury EV market or hybrid vehicles. In the electrical power grid field, an essential component for smart grid development is large-scale energy storage, needed in order to balance the variable supplies with variable demands. Variable demands come from global needs for renewable energy sources, such as solar and wind, which are widely known as "variable power sources" because they are inconstant in nature[8]-[11]. An illustration of emerging battery applications is shown in Figure 1.1.

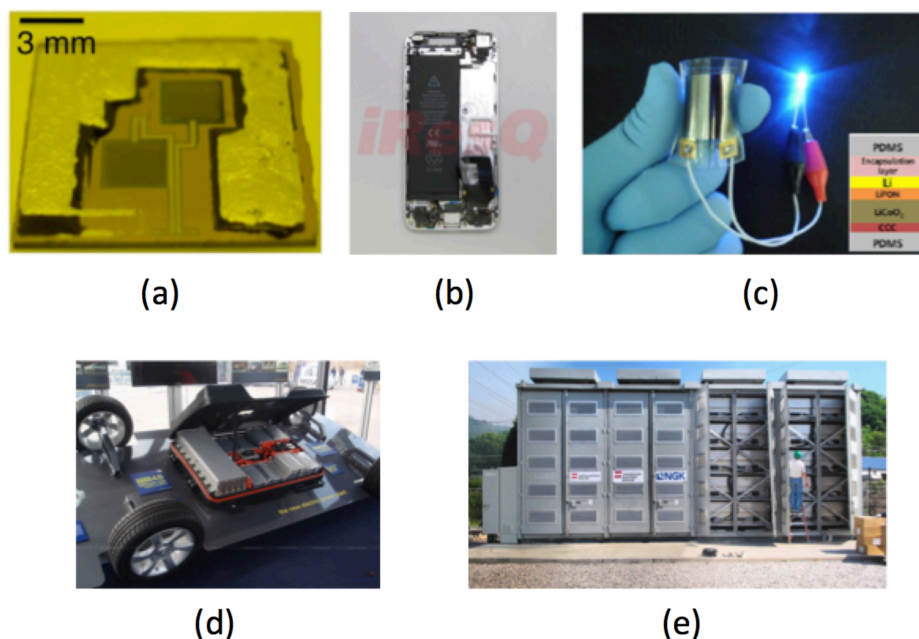


Figure 1.1. (a) Integration Concept of printed energy storage and MEMS piezoelectric energy harvesting device as a power supply system for wireless sensor nodes ([12]); (b) Lithium ion

batteries occupy almost half of the back space of iPhone 5; (c) Flexible Lithium ion batteries activating a blue LED in bent conditions ([13]); (d) 48 lithium ion battery modules in Nissan Leaf stores 24 kWh energy for powering 80 kW AC motors; (courtesy of Nissan) (e) Sodium sulfur battery with one megawatt of storage installed on AEP's grid. (courtesy of AEP)

In summary, high performance and cost effective batteries from mW to MW scales for various energy storage applications are expected to have a significant impact on products and markets in the near future. Therefore, numerous efforts initiated by the scientific and industrial communities have been devoted to fundamental and applied battery technologies research and development in recent years. This has especially been the case since 2000. Both a fundamental breakthrough in battery chemistry and major innovations in fabrication methods are needed to significantly reduce battery cost, and to allow for easier integration with such a wide variety of applications. The use of cost-effective, high-throughput flexographic printing technology to manufacture zinc-based solid-state batteries, as discussed in this dissertation, has the potential to disrupt the current battery landscape. As will be discussed in the following sessions, this is majorly because the flexibility of this method has the potential to create desired geometries at scalable power scales and integrate conveniently with other printable photovoltaic cells and electronics.

1.2. Grid Energy Storage Technologies

The need for electrical energy storage for utility applications has been discussed for decades, especially with regards to its potential economic benefits for various applications such as load leveling and grid reliability improvement. Grid-scale energy storage has particularly attracted public attention in recent years, and is regarded as one of the most important component of the “smart grid.” This is because of the potential role of grid-scale energy storage in complementing intermittent renewable energy sources[8], as illustrated in Figure 1.2[14]. In California, Renewables Portfolio Standard (RPS) was established by legislation; with the requirement that California’s electric utilities obtain 33% of their retail sales derived from eligible renewable energy resources in 2020 and all subsequent years. This decision offers great commercial opportunities for energy storage technologies.

Overviews on application benefits, advantages and limitations of various storage technologies have been presented in[8]-[10], [15]. The most promising storage technologies for electricity can be classified by the form of energy storage/conversion[16]: (1) kinetic energy conversion: flywheels; (2) potential energy conversion: pumped hydroelectric storage; (3) internal energy conversion: compressed air energy storage; (4) chemical energy conversion: batteries and fuel cells; (5) direct electricity storage: supercapacitors. Based on the individual mechanism, each storage technology offers its own advantage, and thus its own specific grid scale applications. Detailed discussions for each technology can be found in the above references. Currently, pumped hydroelectric systems account for 99% of a worldwide storage capacity of 17,000 MW of discharge power, with compressed air storage a distant second at 440MW[15]. Most of other technologies could still be considered in the research and development or demonstration stage.

Batteries based on electrochemical energy storage possess a number of unique advantages, including pollution-free operation, high energy efficiency, modular system characteristics to meet different grid storage functions[15]. It has been suggested that advanced batteries have the

potential to offer the broadest potential applications among the variety of storage technologies for the smart grid [1]. For example, flexible and modular battery systems have great potential in both centralized and distributed energy storage applications. A comparison of energy density and cost for the five different types of energy storage technologies is shown in Figure 1.3.

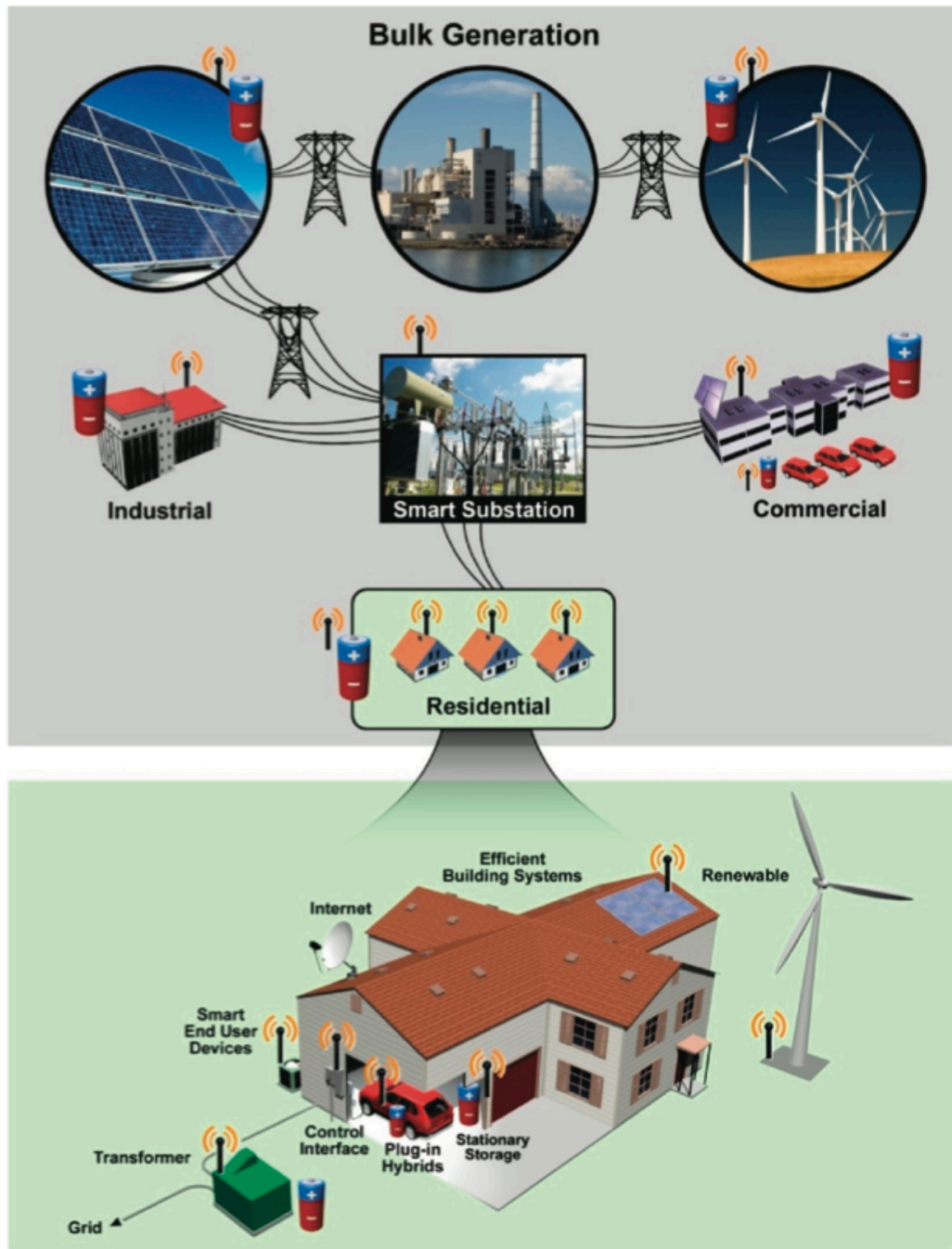


Figure 1.2. A schematic of substantial applications of electrical energy storage for power generation, transmission, distribution and consumption (industrial, commercial as well as residential) in future smart grid system with integration of both renewable energy sources and

plug-in hybrids and electrical vehicles, through two way digital communications between loads and generation in grid (courtesy of Yang[14]).

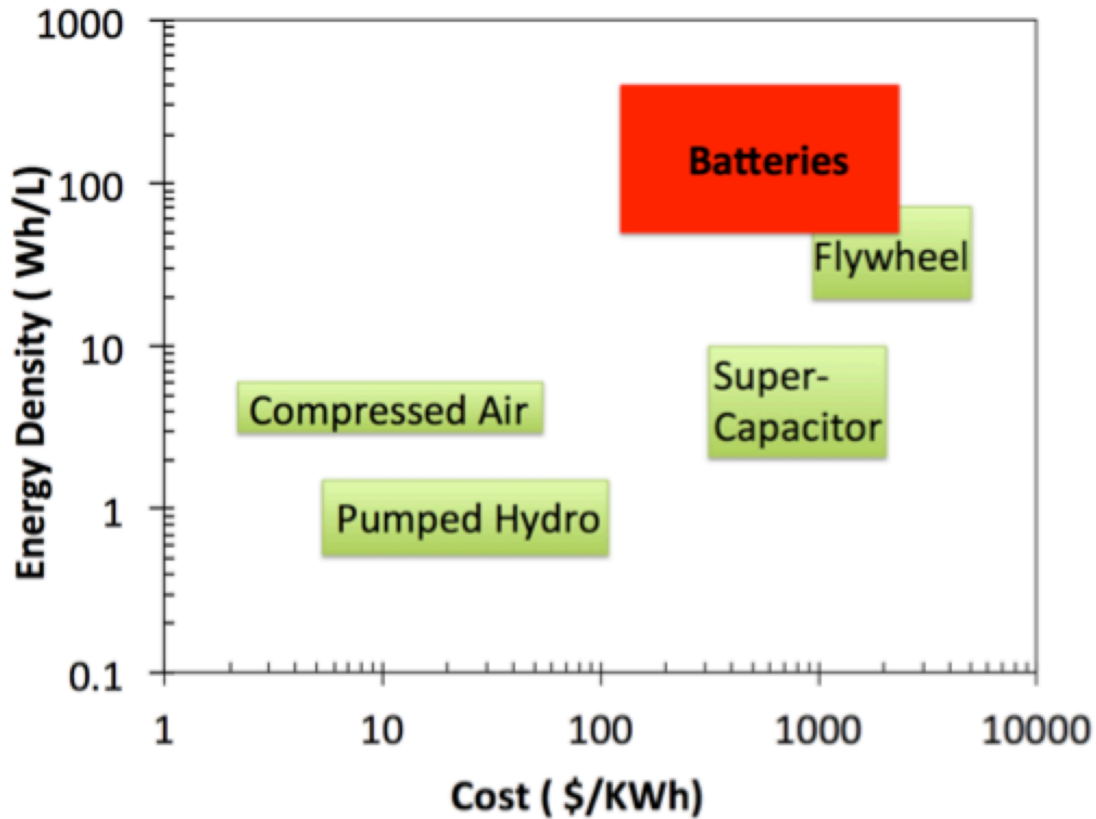


Figure 1.3. Comparison of energy density and cost for five different types of energy storage technologies.

1.3. Battery Operating Principles

Batteries store energy within their electrode structures through charge transfer reactions, based on fundamental electrochemical principles. As illustrated in Figure 1.4, a traditional battery cell consists of a negative electrode, a positive electrode, a separator as well as two current collectors, all of which are immersed in a liquid electrolyte chamber[17]. Both of the two electrodes are either porous or solid materials, which are electrically conductive. The separator is electrically nonconductive but ionically conductive.

The overall cell reaction can be described by two half-cell reactions: one for the negative electrode and one for the positive electrode. During cell discharge, the negative electrode becomes anode, where anodic reaction happens at the anode/electrolyte interface. Simultaneously, the positive electrode becomes cathode, where cathodic reaction happens. Anodic reaction process typically involves oxidation and dissolution of active materials in the electrode into the electrolyte at the interface, during which positive ions (as well as electrons) are formed. Cathodic reaction typically consumes the electronics by reduction and deposition of positive ions in the electrolyte. In the internal current circuit through the cell electrolyte, positive ions move from the anode to the cathode, while negative ions move in the opposite direction. In the external circuit, a potential difference builds up between the positive and negative electrodes

and electrons flows through the load from negative electrode to positive electrode. During cell charge, the processes discussed above are reversed, in which negative electrode becomes the cathode and the positive electrode becomes the anode.

For the purposes of this dissertation, the terms zinc anode and MnO₂ cathode are always used, representing respectively the negative and positive electrode. This remains constant, regardless of whether is the cell is in a charging or a discharging state.

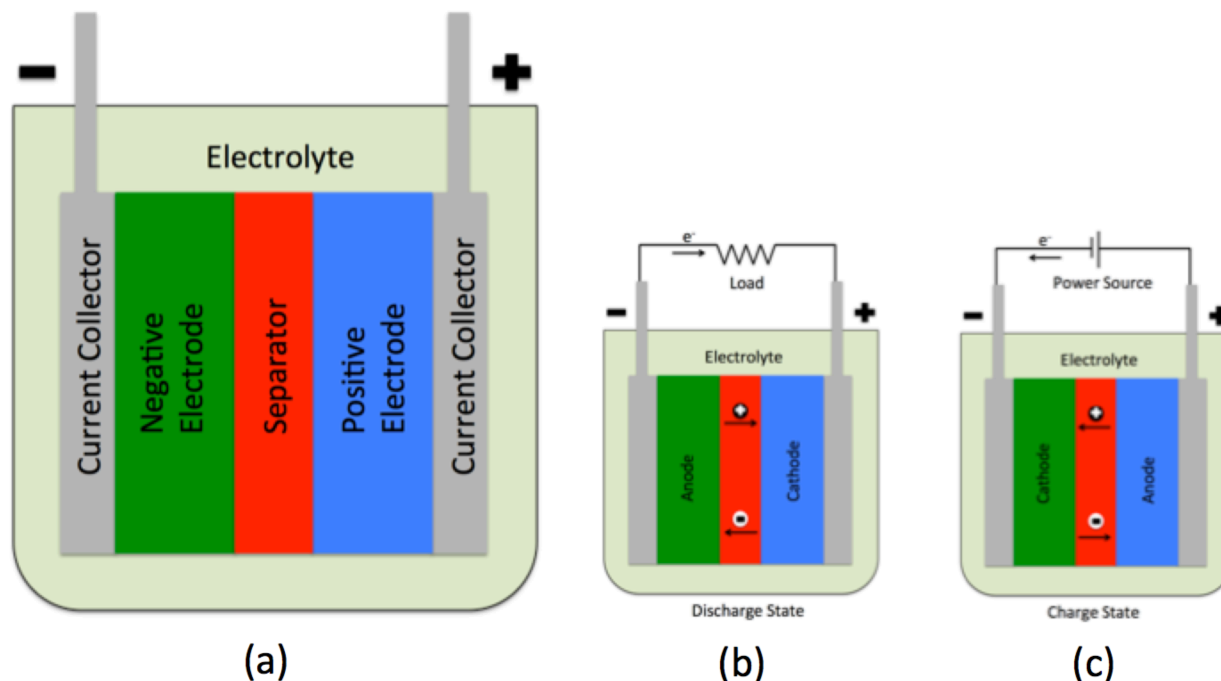


Figure 1.4. (a) Illustration of generic battery cell structure with a liquid electrolyte sealed in a closed system; (b) Battery cell operating in discharge state; (c) Battery cell operating in charge state. (adapted from [17])

The driving force behind both of the anodic and cathodic reactions is the change of standard free energy in the cell system based on thermodynamic theories[18]. The standard cell potential could be calculated based on the following equation:

$$V^{\circ} = -\frac{\Delta G^{\circ}}{nF} \quad (1)$$

where V° is the standard cell potential; n is the number of electrons transferred during the reaction, F is Faraday's constant, and ΔG° is the change of Gibbs free energy in standard state conditions (with electrolyte concentrations of 1 mole per liter (1 M) and pressures of 1 atmosphere at 25°C.) Standard electrode potentials for most half-cell reactions have been put together in tables, so researchers could conveniently search and calculate the overall cell potentials based on the known chemistry[18]. The Nernst equation is typically used to determine the cell potential when the conditions are other than standard state.

Thermodynamics can reveal the feasibility of a cell reaction occurring, as well as the theoretical cell voltage. However, it is equally important to consider electrode kinetics at the electrode/electrolyte interface in order to determine what the actual operating cell voltage may be. This is because the rates of charge transfer are usually the limiting factor. A first step to the

achievement of high power and superfast-charging batteries for electrical vehicles should be the creation of materials with superfast reaction kinetics. The Butler-Volmer equation is one of the most fundamental relationships in kinetics.

Mass transport is the third fundamental area governing the battery cell performance. This is because the ionic transport properties in the electrolyte due to diffusion (in response to concentration gradients), migration (in response to an electric field) as well as convection (bulk fluid motion) can directly influence the reaction kinetics by controlling the amount of reactants and products presented at the interface. The total cell resistance is a combination of the effects of reaction kinetics and mass and electron transfer. (For a detailed description of electrochemical principles, see “*Electrochemical Systems*” by Newman[18]). .

In addition to standard cell potential, the theoretical specific energy of batteries could be calculated based on the following equation:

$$SE^{\circ} = \frac{\Delta G^{\circ}}{m} = \frac{-nFV^{\circ}}{m} \quad (2)$$

where

SE° is the theoretical specific energy;

and m is the reactant weight.

Therefore, in order to pursue high specific energy battery system, it is necessary to achieve high specific charge storage capacity as well as high voltage materials. Similarly, volumetric energy density of batteries can be analyzed in terms of the density of the materials.

As for the cell rechargeability, batteries can be classified as primary (nonrechargeable) and secondary (rechargeable) batteries, based on whether the electrode reactions are reversible or not. While there are specific theoretical and engineering explanations regarding the nonrechargeability for each type of primary batteries, there is no universally applicable electrochemical theory, which is capable of accounting for all battery chemistries. For example, it is generally believed that zinc-based alkaline batteries are not rechargeable because zinc electrodes have serious problems with shape change, as well as with the growth of dendrites[19]. Likewise, it is widely understood that traditional lithium-sulfur batteries suffer from relatively brief life times primarily because of the volume expansion of sulfur during discharge[20]. Specific improvements or developments are therefore needed to transform each particular battery chemistry into a rechargeable system. In this thesis, the main focus will be upon rechargeable zinc-based batteries. .

1.4. Battery Design

In addition to cell operating principles just discussed determining performance, battery design must also take into account other important metrics. These additional considerations must include specific application, materials and manufacturing cost, as well as safety. An overview of battery design considerations, regarding the geometric structure, chemistry as well as fabrication, will now be presented.

1.4.1. Geometric Structure

Even though all battery cells have the same essential components, the actual cell formats vary significantly. Battery geometries, including shape and size, should be designed not only based on specific applications, but also upon the specific chemistries used. Batteries in the early days were designed in jars, but mass production transformed the packaging primarily to cylindrical cell structure design[21]. While the cylindrical cell continues to be one of the most widely used shape and packaging styles for both primary and secondary cells in market, new commercial battery formats utilizing other shapes have emerged. These include button cells, prismatic cells, as well as the pouch cell, as shown in Figure 1.5[17], [21]. Table 1.1 summarizes the four primary cell structure designs, including the advantages and disadvantages of each, suitable chemistries, as well as applications.

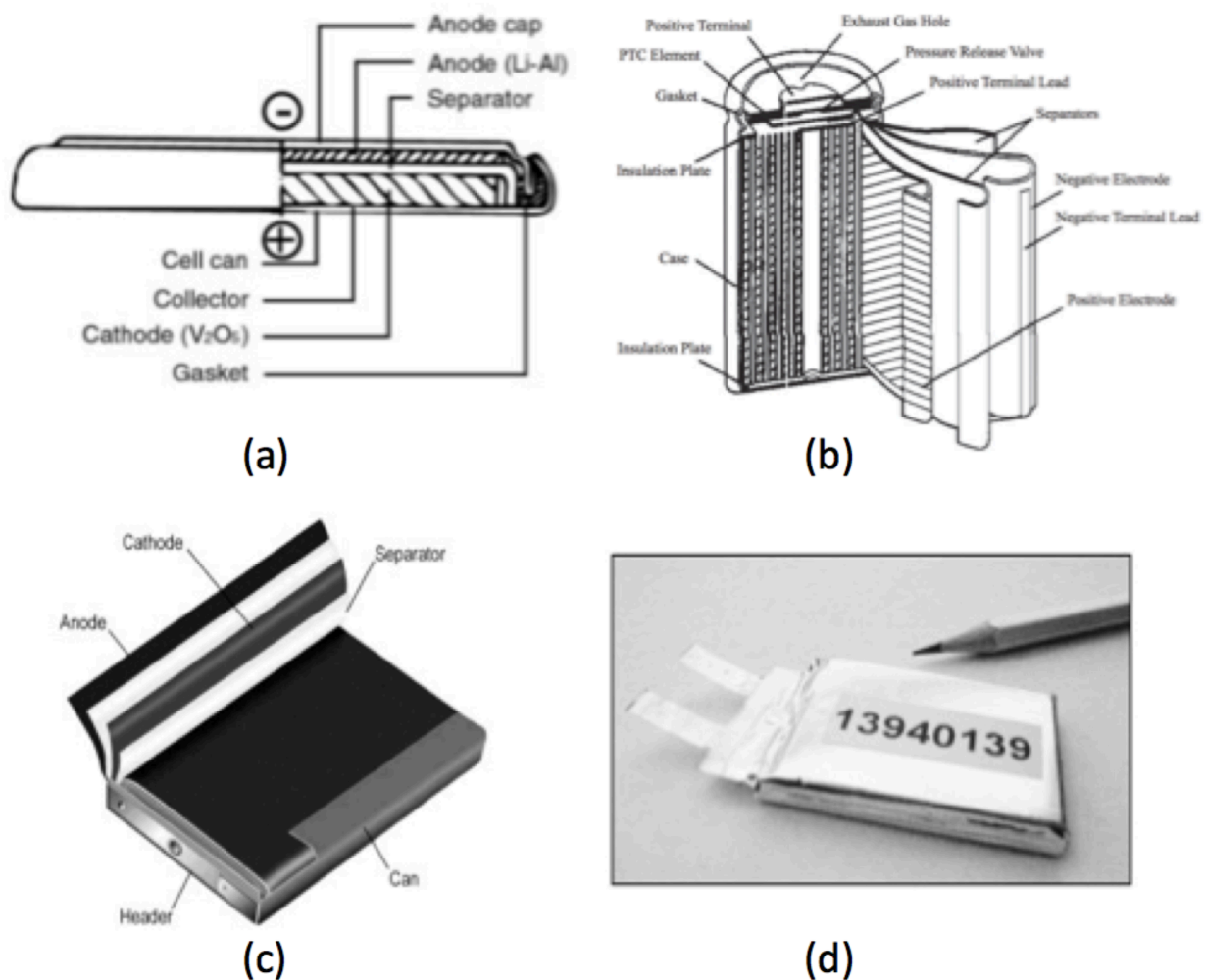


Figure 1.5. (a) Cross section of a button cell (courtesy of Panasonic); (b) Cross section of a Li-ion cylindrical cell (courtesy of Panasonic); (c) Cross section of a prismatic cell (courtesy of Polystor); (d) a pouch cell (courtesy of Cadex).

To achieve the desired operating voltage, a full battery pack usually has several cells connected in series, with each cell adding to the total voltage. At the same time, parallel connection of cells

can be added into the system to obtain higher capacity, with each cell adding to the total current handling capability. A combination of serial and parallel cell connections in the battery system should be also considered. For example, laptop batteries commonly use four 3.6V Li-ion cells in series to achieve 14.4V, and use two such sets of four cells in parallel to boost the capacity from 2,400mAh to 4,800mAh[21]. Most battery chemistries will allow cell serial and parallel configuration internally, but it is crucial to use the same battery type with equal capacity, as well as voltage, throughout and to never mix different makes and sizes. A weaker cell can cause an internal current and potential imbalance and reduce the battery efficiency and lifetime.

As will be discussed below, distinct from the traditional cell geometries, printable batteries present an innovative, more flexible, and simplified battery structural design for scalable applications. Utilization of gel electrolyte based solid-state battery chemistry also substantially minimizes the packaging requirements.

Table 1.1. Comparison of four different types of cell formats in respect to typical chemistry, advantages, disadvantages, and primary applications (adapted from [21]).

Cell Types	Typical chemistry	Advantages	Disadvantage	Applications
Cylindrical	<ul style="list-style-type: none"> Alkaline Lead Acid NiCd NiMH Li-ion 	<ul style="list-style-type: none"> Ease of manufacture Good mechanical stability Good cycling ability 	<ul style="list-style-type: none"> Heavy Low packaging density 	<ul style="list-style-type: none"> Power tools Medical Instruments Laptops
Button (Coin)	<ul style="list-style-type: none"> Alkaline 	<ul style="list-style-type: none"> Small size Inexpensive to build Ease of stacking 	<ul style="list-style-type: none"> Do not allow fast charging Mainly non-rechargeable 	<ul style="list-style-type: none"> Medical implants Watches Hearing aids Car keys Memory backup
Prismatic	<ul style="list-style-type: none"> Li-ion 	<ul style="list-style-type: none"> Improved space utilization Allows flexible design Lower manufacturing cost 	<ul style="list-style-type: none"> More expensive to manufacture Less efficient in thermal management Shorter cycle life 	<ul style="list-style-type: none"> Mobile phones Laptops Hybrid and electric vehicles
Pouch	<ul style="list-style-type: none"> Li-polymer 	<ul style="list-style-type: none"> Simple, flexible and light weight design Highest packaging efficiency 	<ul style="list-style-type: none"> Sensitive to high humidity and temperature environments Less durable 	<ul style="list-style-type: none"> Consumer electronics Military Automotive

1.4.2. Battery Chemistries

Rechargeable battery systems will be the main focus of this thesis. Each different type of battery chemistry has its own unique performance and cost advantages, as well as limitations. Thus, the battery chemistry should be carefully selected for each different type of application. Primary batteries can be used up to 10 years after manufacture, and generally have much higher energy densities than secondary batteries[21]. The main primary battery chemistries currently on the market include alkaline, lithium metal as well as zinc-air.

The four main types of commercially available rechargeable battery chemistries are compared in Table 1.2. Lead-acid batteries currently account for almost half the demand. These types are primarily used in automotive and stand-by applications. Because of low cost and reliable service in unfavorable environmental conditions[21], lead-acid cells are expected to continue to enjoy a steady increase in popularity in the near-term future. Nickel-cadmium (NiCd) batteries command a major market share in such applications as power tools, UPS, two-way radios, and medical devices. NiCd chemistry is preferred over nickel-metal-hydride (NiMH) for its high durability and reliability, but some countries have banned its use due to environmental considerations. The market for NiCd cells is slowly being taken over by NiMH and Li-ion batteries, because cadmium is highly toxic. In 1991, lithium-ion battery was introduced by Sony. Since that time, because of their high operating voltages and energy densities[22], lithium-ion batteries have significantly impacted the rechargeable battery industry. Li-ion batteries rapidly became the dominating power sources for portable electronic devices, especially for cell phones and laptop computers[23]. Three main types of lithium ion battery have been developed and commercialized. Each of these is based upon different transitional metal oxide materials used for the cathode, including cobalt oxide, manganese oxide, and iron phosphate [21][24].

Table 1.2. Comparison of the characteristics of four commonly used rechargeable battery systems, showing the average performance ratings at the time of publication (adapted from [21]).

Specifications	Lead Acid	NiCd	NiMH	Li-ion		
				Cobalt	MnO ₂	Phosphate
Specific energy (Wh/kg)	30-50	45-80	60-120	150-190	100-135	90-120
Internal resistance	<100 12V pack	100-200 6V pack	200-3000 6V pack	150-300 7.2V	25-75 Per cell	25-50 Per cell
Cycle life (80% discharge)	200-300	1000	300-500	500-1000	500-1000	1000-2000
Fast-charge time	8-16h	1h typical	2-4h	2-4h	1h or less	1h or less
Overcharge tolerance	High	Moderate	Low	Low. Cannot tolerate trickle charge		
Self-discharge/month(rt)	5%	20%	30%	<10%		
Cell voltage(V)	2	1.2	1.2	3.6	3.8	3.3
Peak load current	5C 0.2C	20C 1C	5C 0.5C	>3C <1C	>30C <10C	>30C <10C
Charge temperature	-20-50°C	0-45°C	0-45°C	0-45°C		
Discharge temperature	-20-50°C	-20-65°C	-20-65°C	-20-60°C		
Maintenance requirement	3-6 months	1-2 months	2-2.5months	Not required		
Safety requirements	Thermally stable	Thermally stable	Thermally stable	Protection circuit mandatory		
In use since	Late 1800s	1950	1990	1991	1996	1999
Toxicity	Very high	Very high	Low	Low		

It has largely been these small and light-weight Li-ion batteries which has made the proliferation of modern portable devices possible, such as the smartphones which give people convenient Internet access, multimedia entertainment, navigation and communication capabilities. However, the growing functionality of such devices requires the supply of ever-increasing levels of power

to support the operation of these devices. It is important to realize that even for the lithium-ion battery, energy density shows a slow growth rate—only about 10% per year. This is a much lower rate than that of the integrated circuits transistor density growth rate, which, following Moore’s Law, continues to double every two years. To keep pace with the state of the art IC development, the power and energy performance of Li-ion batteries needs to be significantly improved. Due to the highly reactive nature of the materials, safety issues have also always been (and continue to be) a problem for the Li-ion chemistry.

For grid storage applications, several other rechargeable battery chemistries are currently under development. This is being done with the aim to significantly reduce the cost to compete with fossil fuel power sources. These new technologies include sodium-sulfur, vanadium redox flow, sodium-metal chloride, as well as lithium metal polymer batteries. A comparison of the promising grid storage chemistries is presented in Figure 1.6, in terms of both gravimetric power and energy densities. Lithium-ion batteries have a great advantage in terms of both power and energy densities. However, as will be discussed in a later section, the capital cost per unit of power and energy are still relatively too high for grid applications. (The advantage of zinc-based chemistry for this application will be presented in detail below).

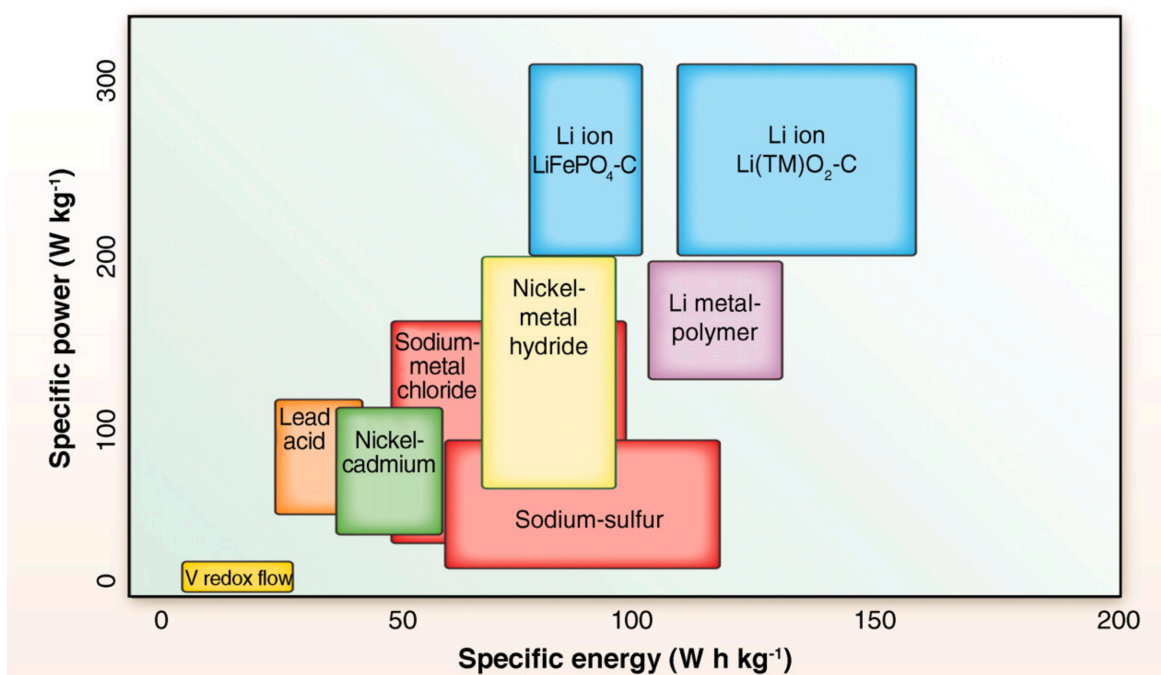


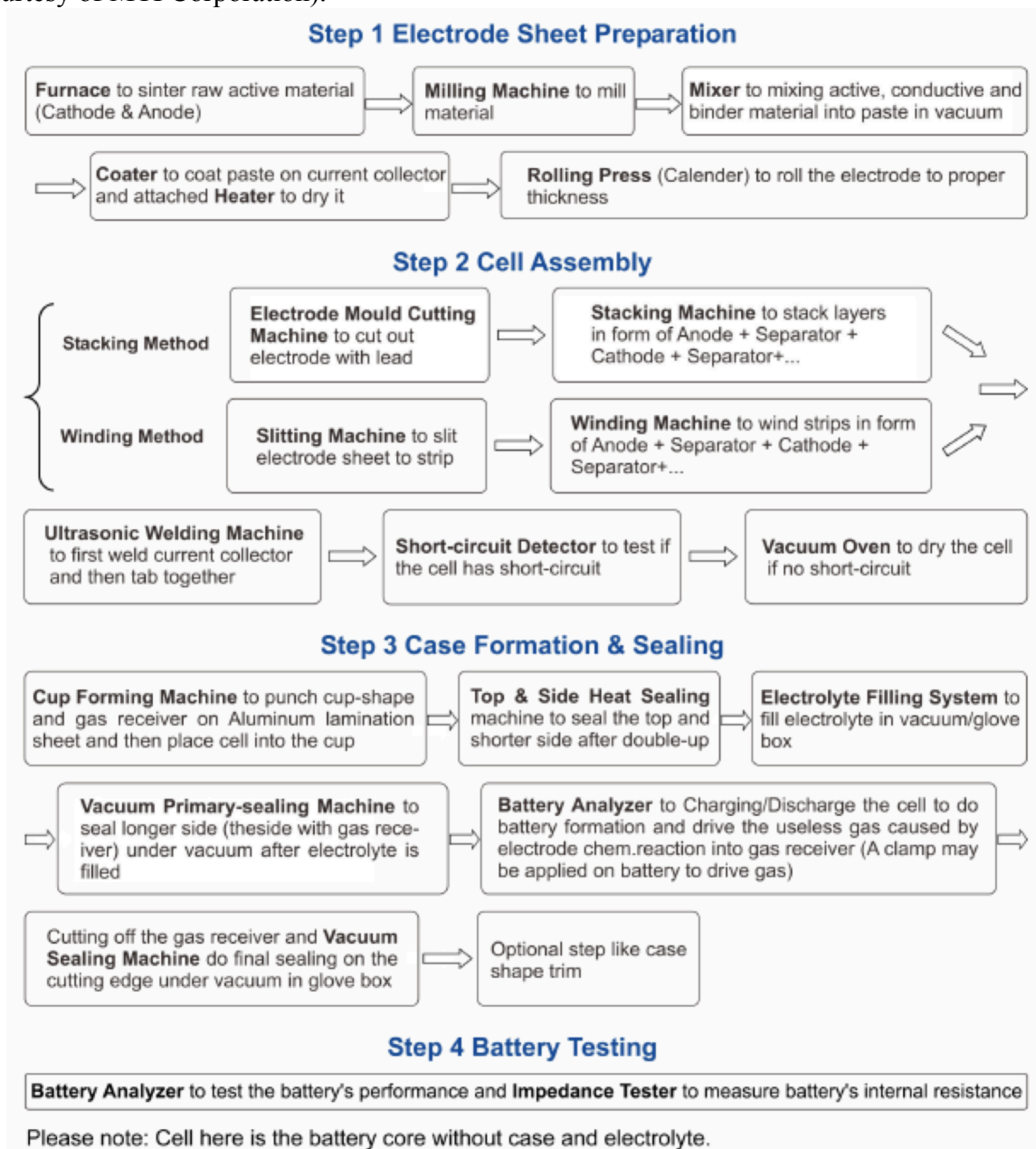
Figure 1.6. Specific power and specific energy for different rechargeable battery systems. Most of these chemistries are currently being investigated for grid storage applications (courtesy of Bruce Dunn[15]).

1.4.3. Fabrication

For each different type of battery cell system, a specific fabrication method needs to be designed for manufacturing them at different levels of scale. Manufacture of battery chemistries with highly air reactive materials, (for example, lithium), is extremely complicated and expensive. The typical fabrication process for lithium-ion pouch cells is shown below in Figure 1.7. At least

four major steps are involved: (1) Electrode sheet preparation; (2) Cell assembly; (3) Case formation & sealing; and (4) Battery testing. Within each major step, many small stages and a considerable amount of specific equipment are needed for the production of all components of the cells. Manufacturing environments need to be strictly controlled, including such factors as inert gas environments for lithium electrode storage and cell assembly and high vacuum oven environments for electrode drying and formation. Tight tolerances and strict process controls are crucial throughout the lithium-ion manufacturing process [25]. Any chemical contamination or physical flaws on the electrodes can cause fatal failure because they can potentially cause penetration of the thin, porous separator, giving rise to internal short circuits in the cell [25].

Figure 1.7. Diagram of Li-ion pouch cell fabrication process and equipment utilizations (courtesy of MTI Corporation).



While development and application of grid energy storage has been limited by many factors, including economic payback time, government policies, battery lifetime and reliability, the high cost of large-scale battery manufacturing is one of the most challenging problems[11]. This cost primarily consists of the materials costs and production costs for the system. In the future, the preferred energy storage technologies will need to be using low-cost, environmentally friendly materials that are developed into battery cells through a relatively simple manufacturing process[15]. In the following sections, both the novel rechargeable zinc-based battery chemistries and their fabrication using printing techniques will be discussed.

1.5. Printed Rechargeable Zinc-based Battery

Significant research efforts in the battery community have recently been made towards development of rechargeable zinc battery chemistries. These efforts have been motivated primarily by their high energy and power densities, inherent safety, low toxicity, relative ease in handling, and low cost[26]-[29]. Specifically, rechargeable nickel-zinc [30], [31], silver-zinc[32], alkaline manganese dioxide (MnO_2)-zinc [28], [33] and zinc-air[34], [35] batteries have been studied. All chemistries discussed above, however, share a common challenge regarding the weak rechargeability of the zinc electrode, predominantly due to unwanted shape changes, dendrite formation, as well as the solubility of reaction products within the typical alkaline electrolyte[36]. On the cathode side, the proton intercalation reaction based on alkaline electrolyte is not a reversible process. There are significant phase and structural changes happening to MnO_2 cathode, such as expansion and contraction during reaction, which leads to internal cell resistance increase. Researchers have thus been working towards solutions involving replaceable alkaline electrolytes, with special interest in ionic liquid electrolyte[27].

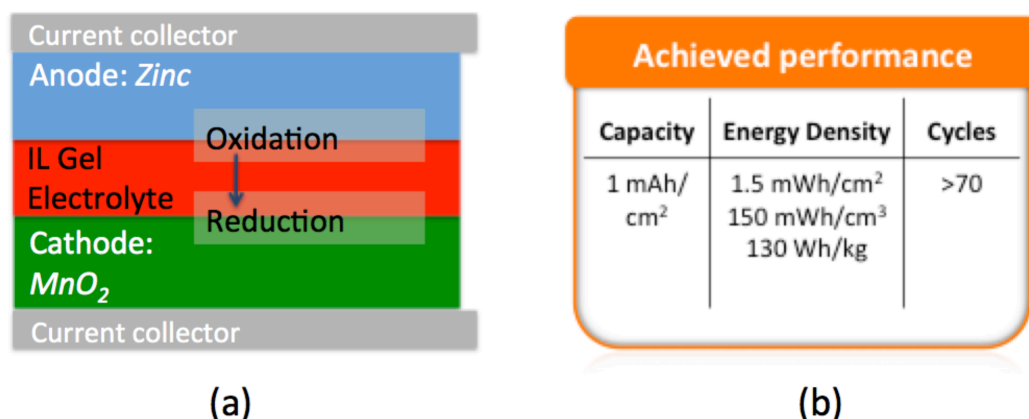


Figure 1.8. (a) Illustration of the cross section of a printable zinc-based microbattery[29]; (b) Electrochemical performance of the first prototype of the microbattery, including capacity per footprint area, energy density as well as cycle life[29].

Ionic liquid electrolytes were first used as promising electrolyte solvents for lithium-ion batteries[37], [38], supercapacitors[39], [40] and fuel cells[41], [42]. Ionic liquids are room-temperature molten salts, which are typically composed of asymmetric organic cations and inorganic anions. Ionic liquids possess many especially attractive properties, such as ultra-low volatility, ultra-low flammability, low viscosity, high thermal stability, high ionic conductivity,

and a wide electrochemical stability window[27]. It was first demonstrated by Xu et al.[27] that zinc ions are mobile in a polymer gel electrolyte (PGEs) based on ionic liquids, and that zinc metal is capable of dissolving into and depositing from the membranes. These membranes also exhibit wide electrochemical stability window. Dr. Christine Ho, from the same research group of this Ph.D. dissertation author, subsequently developed a printable zinc-manganese dioxide microbattery for wireless sensor network applications, based on a novel ionic liquid (BMIM⁺ Tf⁻) gel electrolyte. As shown in Figure 1.8(a), the microbattery is designed in a fully solid/semi-solid state with a gel electrolyte between the two electrodes, which eliminates (or at least significantly reduces) the need for complicated liquid electrolyte case sealing and packaging. The first microbattery prototype shows promising properties, with the cell exhibiting storage capacities of about 1 mAh/cm² over more than 70 cycles[29] as shown in Figure 1.8(b).

Because of this fully solid-state, flexible pattern structure design, a novel dispenser printing method was developed and utilized for additive manufacturing of the sandwich structured battery, as shown above. Composite inks for each component of the battery were developed and optimized in formulations for achieving good rheology for dispenser printing and electrochemical performance, as shown in Figure 1.9(a). Because zinc is not as air sensitive as lithium metal, the whole fabrication process was done in ambient environment, using a custom-built dispenser printer as shown in Figure 1.9(b). The custom-built dispenser printer demonstrated great flexibility and precision in energy harvesting and energy storage device fabrication for prototyping. For wireless sensor network applications, it provides a flexible method for integration with other energy harvesting, sensing, and data transmitting devices on a variety of substrates. A detailed introduction to its operating mechanism can be found in chapter 3.

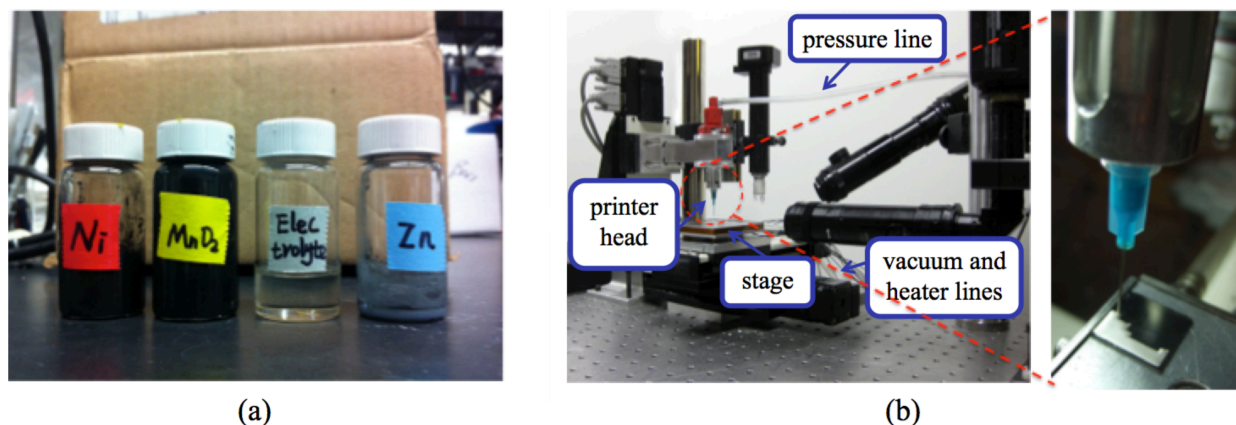


Figure 1.9. (a) Typical functional composite inks for the dispenser printing of different components of the zinc-based batteries: nickel ink for current collector, MnO₂ ink for cathode, ionic liquid ink for electrolyte and zinc ink for anode; (b) Custom built dispenser printer for microbattery prototyping (adapted from Ho[29]).

The printing technique is a highly scalable method, which offers great opportunities for large format zinc-based battery manufacturing for grid storage applications, using traditional screen, gravure, or flexographic printing techniques. The competitiveness of this technique both in terms of capital cost per unit power and per unit energy with other grid energy storage technologies is calculated and illustrated in Figure 1.10. Because of the low cost of the chemicals for zinc-based batteries, as well as for the flexographic printing cost utilized in the estimation, printable zinc-

based battery is promising for a variety of both power and energy related applications in future power grid.

It is important, however, to notice that although the initial zinc-based microbattery experimental results are encouraging, in addition to scaling up the fabrication, the printed rechargeable battery chemistry still needs to be significantly improved in a number of ways. This new chemistry still suffers from a variety of challenging problems, such as capacity fade, low yield and reliability, with contributions possibly coming from both of the materials formulation itself and from the printing process control. In chapter 4, the efforts to understand performance of these batteries in controlled inert environments by making coin cells will be discussed.

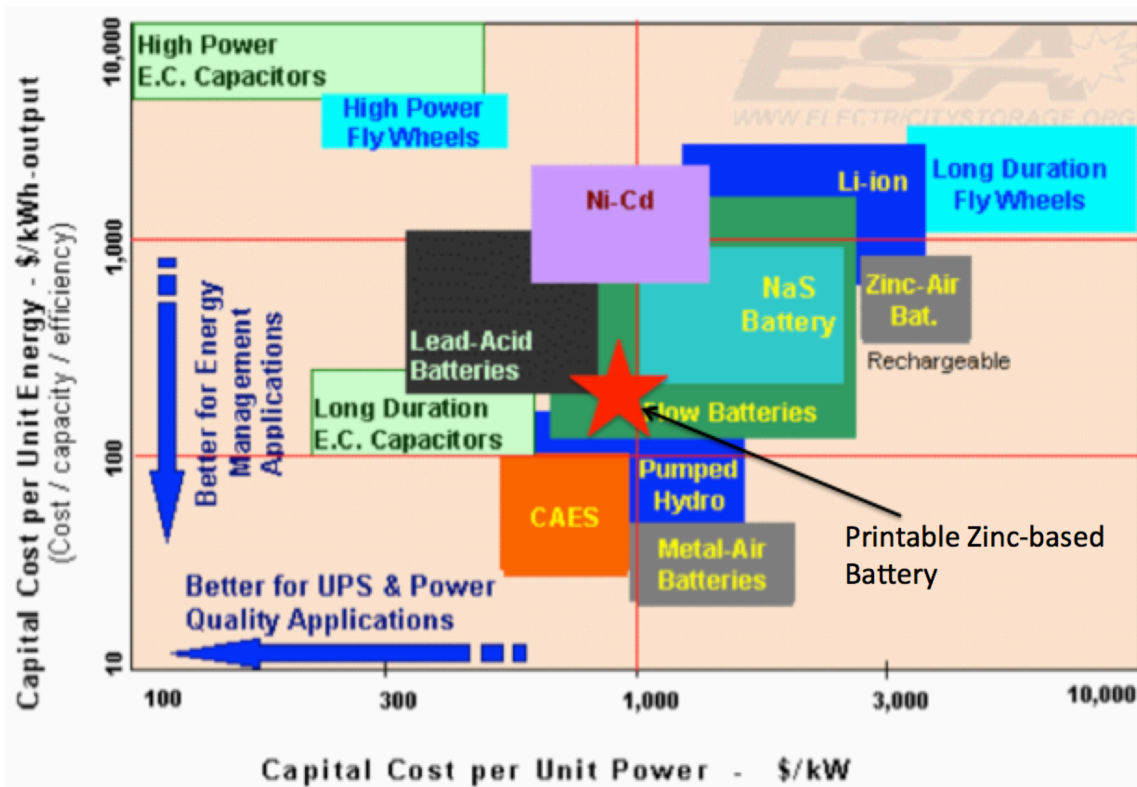


Figure 1.10. Comparison of roll-to-roll printable zinc-based battery with other energy storage technologies in both of capital cost per unit power and per unit energy. The estimation is based on the capital cost of both flexographic manufacturing and materials for the battery. The battery power cost is based on an average discharge rate of 0.1C (courtesy of ESA and Dr.James Evans).

1.6. Chapter Summary

1. Electrochemical energy storage has become a renascent and fast-growing industry, displaying rapid growth in the wireless sensor network, portable electronics, electric vehicles, and smart power grid fields. The current battery solutions have not changed significantly in recent decades, and this lack of improvement has gradually made batteries the limiting factor in technological advancement, and presented great challenges to widespread use of the new technologies. Disruptive battery technologies are needed to keep pace with other energy conversion and semiconductor technologies.

2. Although there are a variety of potential solutions to grid energy storage, batteries offer their own unique advantages, including pollution-free operation, high energy efficiency, and flexible, modular system characteristics to meet different grid functions. Advanced batteries have the potential to offer the broadest potential applications among the variety of storage technologies for the future smart grid.
3. Fundamental electrochemical principles governing the performance of batteries include thermodynamics, chemical reaction kinetics and transport properties. These principles ultimately determine the battery voltage, power density, and energy density. With performance, cost, and applications taken into account, practical battery systems can be designed with regard to structural geometry, chemistry, and fabrication techniques.
4. Printed rechargeable zinc-based batteries represent a promising technology for grid energy storage applications in terms of their performance and cost, as well as scalability in fabrication. While custom-built dispenser printing is great for prototyping, this technique has limitations that prevent it from being cost-effective for larger-scale production. Therefore, as a proposed solution to such limitations, a roll-to-roll, flexographic printing technique utilized for the large-scale zinc battery manufacturing and enhanced battery performance with new ink formulations, will be presented in the following chapters. .

Chapter References

- [1] E. P. James, M. J. Tudor, S. P. Beeby, and N. R. Harris, "ScienceDirect.com - Sensors and Actuators A: Physical - An investigation of self-powered systems for condition monitoring applications," *Sensors and Actuators A*, 2004.
- [2] J. Wilson, V. Bhargava, and A. Redfern, "A Wireless Sensor Network and Incident Command Interface for Urban Firefighting," *Mobile and Ubiquitous: Networking & Services*, 2007.
- [3] N. Ota, S. Ahrens, A. Redfern, P. Wright, and 2. I. I. C. O. Xin Yang Mobile Adhoc and Sensor Systems MASS, "An Application-Driven Architecture for Residential Energy Management with Wireless Sensor Networks," presented at the *Mobile Adhoc and Sensor Systems (MASS), 2006 IEEE International Conference on*.
- [4] A. Milenković, C. Otto, and E. Jovanov, "ScienceDirect.com - Computer Communications - Wireless sensor networks for personal health monitoring: Issues and an implementation," *Computer Communications*, 2006.
- [5] S. Roundy, P. K. Wright, and J. Rabaey, "ScienceDirect.com - Computer Communications - A study of low level vibrations as a power source for wireless sensor nodes," *Computer Communications*, 2003.
- [6] D. Madan, A. Chen, P. K. Wright, and J. W. J. O. A. P. Evans, "Dispenser printed composite thermoelectric thick films for thermoelectric generator applications," *J. Appl. Phys.*, vol. 109, no. 3.
- [7] A. Chen and P. K. Wright, "Medical Applications of Thermoelectrics," *researchgate.net*.
- [8] D. O. Energy, "Energy Storage-A Key Enabler of the Smart Grid," pp. 1–16, Sep. 2009.
- [9] I. Gyuk, P. Kulkarni, J. H. Sayer, J. D. Boyes, G. P. Corey, and G. H. P. A. E. M. I.

- Peek, "The United States of storage [electric energy storage]," *Power and Energy Magazine, IEEE*, vol. 3, no. 2, 2005.
- [10] K. C. Divya and J. Østergaard, "Battery energy storage technology for power systems—An overview," *Electric Power Systems Research*, vol. 79, no. 4, pp. 511–520, Apr. 2009.
 - [11] D. H. Doughty, P. C. Butler, and A. A. Akhil, "Batteries for large-scale stationary electrical energy storage," *The Electrochemical Society Interface*, 2010.
 - [12] L. M. Miller, P. K. Wright, C. C. Ho, J. W. Evans, P. C. Shafer, and R. Ramesh, "Integration of a low frequency, tunable MEMS piezoelectric energy harvester and a thick film micro capacitor as a power supply system for wireless sensor nodes," *Energy Conversion Congress and Exposition, 2009. ECCE 2009. IEEE*, pp. 2627–2634, 2009.
 - [13] M. Koo, K.-I. Park, S. H. Lee, M. Suh, D. Y. Jeon, J. W. Choi, K. Kang, and K. J. Lee, "Bendable Inorganic Thin-Film Battery for Fully Flexible Electronic Systems," *Nano Lett.*, vol. 12, no. 9, pp. 4810–4816, Sep. 2012.
 - [14] Z. Yang, J. Liu, S. Baskaran, C. H. Imhoff, and J. D. Holladay, "Enabling renewable energy—and the future grid—with advanced electricity storage," *JOM*, vol. 62, no. 9, pp. 14–23, Sep. 2010.
 - [15] B. Dunn, H. Kamath, and J. M. Tarascon, "Electrical Energy Storage for the Grid: A Battery of Choices," *Science*, vol. 334, no. 6058, pp. 928–935, Nov. 2011.
 - [16] H. Chen, T. N. Cong, W. Yang, C. Tan, Y. Li, and Y. Ding, "Progress in electrical energy storage system: A critical review," *Progress in Natural Science*, vol. 19, no. 3, pp. 291–312, Mar. 2009.
 - [17] C. D. Rahn and C. Y. Wang, "Battery Systems Engineering - Christopher D. Rahn, Chao-Yang Wang - Google Books," 2012.
 - [18] J. Newman and K. E. Thomas-Alyea, "Electrochemical Systems - John Newman, Karen E. Thomas-Alyea - Google Books," 2012.
 - [19] D. Rand, "ScienceDirect.com - Journal of Power Sources - Battery systems for electric vehicles — a state-of-the-art review," *Journal of Power Sources*, 1979.
 - [20] H. Wang, Y. Yang, Y. Liang, J. T. Robinson, Y. Li, A. Jackson, Y. Cui, and H. Dai, "Graphene-Wrapped Sulfur Particles as a Rechargeable Lithium–Sulfur Battery Cathode Material with High Capacity and Cycling Stability," *Nano Lett.*, vol. 11, no. 7, pp. 2644–2647, Jul. 2011.
 - [21] I. Buchmann, *Batteries in a Portable World: A handbook on non-rechargeable batteries for non-engineers*. 2011.
 - [22] T. Ohzuku and R. J. Brodd, "An overview of positive-electrode materials for advanced lithium-ion batteries," *Journal of Power Sources*, vol. 174, no. 2, pp. 449–456, Dec. 2007.
 - [23] C. Mikolajczak, M. Kahn, K. White, and R. T. Long, *Lithium-Ion Batteries Hazard and Use Assessment*. Springer Verlag, 2012.
 - [24] A. G. Ritchie, "Recent developments and likely advances in lithium rechargeable batteries," *Journal of Power Sources*, 2004.
 - [25] Electropedia, "Lithium Battery Manufacturing," www.mpoweruk.com, 14-Apr-2013. [Online]. Available: http://www.mpoweruk.com/battery_manufacturing.htm. [Accessed: 14-Apr-2013].
 - [26] A. P. Karpinski, B. Makovetski, S. J. Russell, J. R. Serenyi, and D. C. Williams,

- “Silver–zinc: status of technology and applications,” *Journal of Power Sources*, vol. 80, no. 1, pp. 53–60, Jul. 1999.
- [27] J. J. Xu, H. Ye, and J. Huang, “Novel zinc ion conducting polymer gel electrolytes based on ionic liquids,” *Electrochemistry Communications*, vol. 7, no. 12, pp. 1309–1317, Dec. 2005.
- [28] C. Xu, H. Du, B. Li, F. Kang, and Y. Zeng, “Reversible Insertion Properties of Zinc Ion into Manganese Dioxide and Its Application for Energy Storage,” *lib.ucdavis.edu*.
- [29] C. C. Ho, J. W. Evans, and P. K. Wright, “Direct write dispenser printing of a zinc microbattery with an ionic liquid gel electrolyte,” *J. Micromech. Microeng.*, vol. 20, no. 10, p. 104009, Sep. 2010.
- [30] P. H. Humble, J. N. Harb, and R. LaFollette, “Microscopic Nickel-Zinc Batteries for Use in Autonomous Microsystems,” *J. Electrochem. Soc.*, vol. 148, no. 12, p. A1357, 2001.
- [31] L. Zhang, H. Huang, W. K. Zhang, Y. P. Gan, and C. T. Wang, “Effects of conductive ceramic on the electrochemical performance of ZnO for Ni/Zn rechargeable battery,” *Electrochimica Acta*, vol. 53, no. 16, pp. 5386–5390, Jun. 2008.
- [32] L. R. Erisman and R. A. Marsh, “Patent US4091184 - High power, rechargeable, pile type silver zinc battery - Google Patents,” U.S. Patent 4,091,184/1978.
- [33] K. Kordesh and M. Weissenbacher, “Rechargeable alkaline manganese dioxide/zinc batteries,” *Journal of Power Sources*, vol. 51, no. 1, pp. 61–78, Aug. 1994.
- [34] P. N. Ross Jr, “Zinc electrode and rechargeable zinc-air battery,” U.S. Patent 4,842,963/1989.
- [35] S. Müller, F. Holzer, and O. Haas, “Optimized zinc electrode for the rechargeable zinc–air battery,” *J Appl Electrochem*, vol. 28, no. 9, pp. 895–898, 1998.
- [36] F. R. McLarnon, “The Secondary Alkaline Zinc Electrode,” *J. Electrochem. Soc.*, vol. 138, no. 2, p. 645, 1991.
- [37] A. Webber and G. E. Blomgren, “Ionic Liquids for Lithium Ion and Related Batteries,” in *Advances in lithium-ion batteries*, no. 7, Boston: Kluwer Academic Publishers, 2002, pp. 185–232.
- [38] J. Caja, T. D. J. Dunstan, and M. Caja, “Rechargeable, Lithium-ion Molten Salt Battery for High Temperature Applications,” 2012.
- [39] A. Balducci, U. Bardi, S. Caporali, M. Mastragostino, and F. Soavi, “Ionic liquids for hybrid supercapacitors,” *Electrochemistry Communications*, vol. 6, no. 6, pp. 566–570, Jun. 2004.
- [40] D. Wei and T. W. Ng, “Application of novel room temperature ionic liquids in flexible supercapacitors,” *Electrochemistry Communications*, vol. 11, no. 10, pp. 1996–1999, Oct. 2009.
- [41] H. Nakamoto, A. Noda, K. Hayamizu, S. Hayashi, H. Hamaguchi, and M. Watanabe, “Proton-Conducting Properties of a Brønsted Acid-Base Ionic Liquid and Ionic Melts Consisting of Bis(trifluoromethanesulfonyl)imide and Benzimidazole for Fuel Cell Electrolytes,” *J. Phys. Chem. C*, vol. 111, no. 3, pp. 1541–1548, Jan. 2007.
- [42] R. F. de Souza, J. C. Padilha, R. S. Gonçalves, and J. Dupont, “Room temperature dialkylimidazolium ionic liquid-based fuel cells,” *Electrochemistry Communications*, vol. 5, no. 8, pp. 728–731, Aug. 2003.

Chapter 2

A Survey of Functional Printing Techniques for Scaled-up Battery Fabrication

2.1. Introduction to Printing Technologies

To realize large-scale zinc-based battery manufacturing from prototyping at a dispenser printing level, a survey of available printing techniques is presented in this chapter. Traditional graphic printing is a reproduction process. Kipphan writes that¹ “*printing ink is applied to a printing substrate in order to transmit information (images, graphics, text) in a repeatable form using an image-carrying medium*”[1]. The graphic ink is typically a pigmented substance. An overview of most common printing technologies is given in Figure 2.1. A classification can be made based on whether the printing technologies require a printing plate or image carrier [1]. Conventional technologies developed over the past few centuries generally require a printing plate, while newly developed digital printing technologies are plateless.

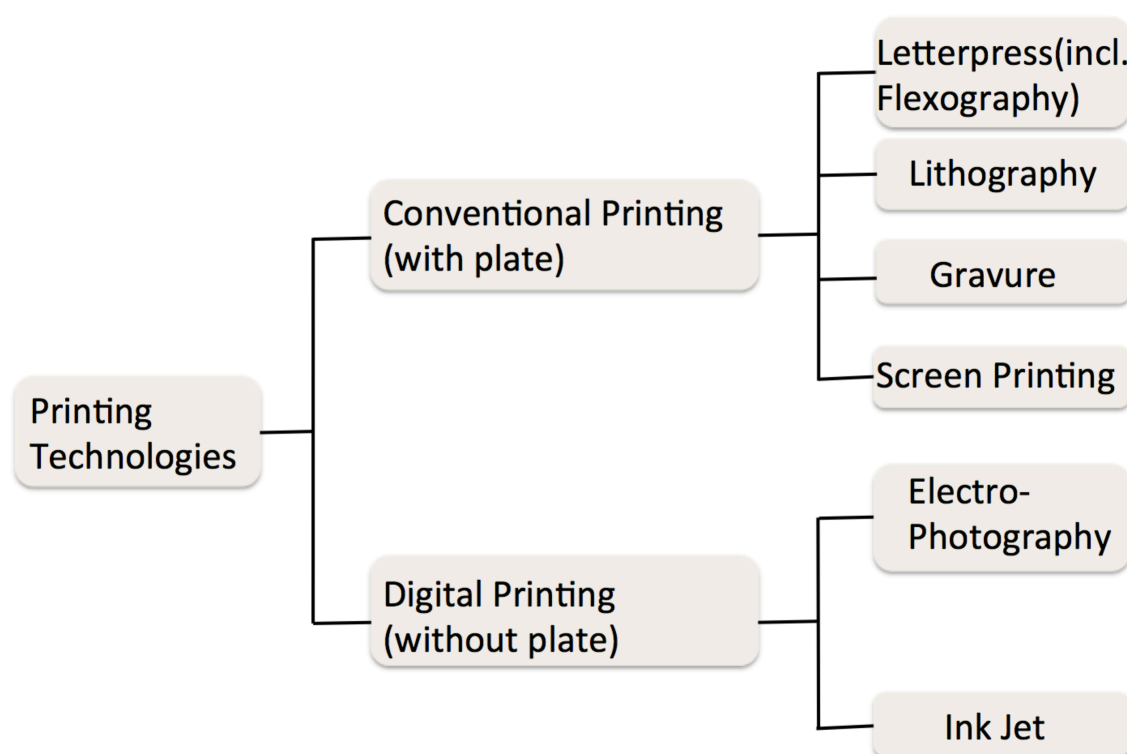


Figure 2.1. The main printing technologies: four conventional printing requiring a plate and two plateless digital printing (adapted from[1]) .

¹ Appears in [1]: page 40.

The main conventional technologies requiring printing plates are further divided according to the physical characteristics of the printing surface used[2], as shown in Figure 2.1.

Letterpress, including flexography, is an ink relief process. The image area is raised above the background materials. The raised printing surface is first inked by an anilox roller during the printing process, and then pressed against the printing substrate to finish the ink and image transfer.

Lithography utilizes a planographic (flat) printing surface. The image area is chemically treated so that it accepts inks (oleophilic), but rejects water (hydrophobic) during printing process. The non-image area is chemically treated to be oleophobic and hydrophilic.

Gravure printing is an intaglio process, in which the printing image is typically recessed into the surface of a metallic cylinder. Cells engraved on the metallic surface, are filled with ink, while the non-image area is wiped free of ink with a doctor blade during printing. The image is transferred to the printing substrate through the inks in the recessed cells.

In screen printing process, the image is printed in an open mesh area, where the ink is forced through the stencil printing plate when a squeegee is moved across the top of the screen stencil [1]. An illustration and comparison of the four main conventional printing technologies is shown in Figure 2.2.

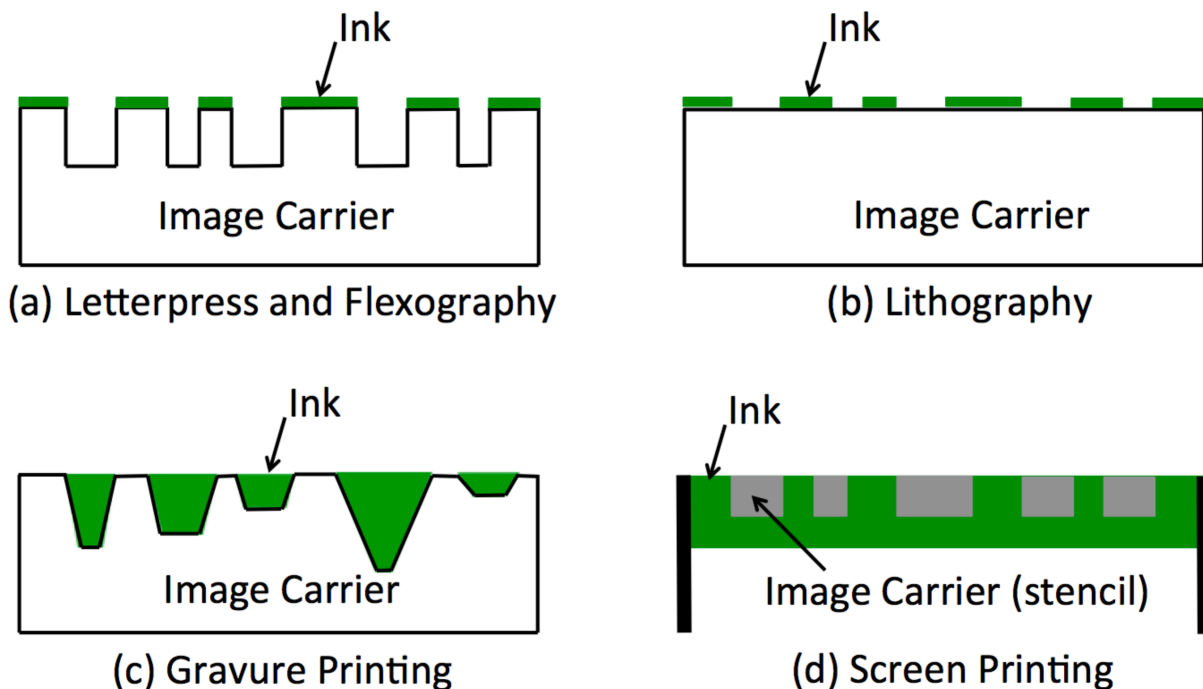


Figure 2.2. Illustration and comparison of the four main conventional printing plate or image carrier-based printing technologies (adapted from [1] and[2]).

Digital printing takes an electronic data file and transfers the printing image digitally to the designated printing device[2]. The dominant digital printing technologies are electrophotography (laser printing) and ink jet printing. Compared to conventional printing technologies, digital printing enables short run reprinting, personalized, and “print on demand” printing[2]. However, the printing quality of digital printing is slightly inferior to most conventional technologies, and it is less economical for large-scale printing, especially for web-fed printing process.

Each of the printing technologies has its own set of advantages and disadvantages. Therefore, each of them is found most suitable for certain applications and not others. This is true not only in the graphic printing field, but also in the emerging printed electronics industry, such as the manufacturing of OLED displays, photovoltaic cells, sensors, and logic memory. However, in general, printed electronics is based on functional electronic materials additive processes, in contrast to traditional subtractive batch processes. Typically, printed electronic processes could be performed in ambient temperature and pressure conditions, instead of the controlled environments required for most subtractive procedures[3]. In the following section, printing technology selection criteria and considerations for large-scale energy storage fabrication will be discussed.

2.2. Battery Printing Technology Design and Selection

A suitable functional printing technology should meet the requirements of being compatible with the print materials, capable of printing specific device structure, and being economically effective at desired manufacturing scales. For grid scale zinc-based battery manufacturing, the printing system components and process should be compatible with a variety of electrode slurries and electrolyte solutions. Such slurries and solutions consist of various polymeric binder materials, metal powders, conductive carbon blacks, solvents as well as surfactant additives. Battery printing has relatively low requirements regarding the printing resolution. The printing system should be able to print multilayer structures with desired film thickness and uniformity. For example, the battery electrodes are typically in a range of 20-100 μ m, and the gel electrolyte are typically in a range of 5-30 μ m. The printing system is required to manage the printing of large format batteries at high speed with low cost, so a roll-to-roll, web-fed printing process is desirable. A summary of printing process design and selection criteria as well as considerations for grid energy storage fabrication is shown in Table 2.1.

The various printing technologies will be discussed addressing these important aspects as well as their current applications in printed electronics field discussed for each. For a comprehensive introduction to each of these graphic printing technologies, it is recommended to refer to “*Handbook of Print Media*,” by Kipphan[1].

Because gravure printing typically uses a metallic printing plate, it has the disadvantage of being highly expensive in terms of the plate cylinder and printing plate preparations, and being not suitable for multilayer structure printing as is required for solid-state batteries. Research on using gravure printing for fabrication of ITO transparent electrodes[4], solar cells[5], and polymer field-effect transistors[6] has been conducted.

The plate chemical treatment and ink transfer principle make the offset lithography process unsuitable for functional battery ink printing. This is because these features interfere with the faithful reproduction of the chemical properties of the printed device, which is indispensable for the battery fabrication.

Table 2.1. Printing process design and selection criteria, and considerations for grid scale zinc-based battery fabrication.

Printing Process Design Criteria	Consideration for Grid scale Battery Fabrication
Ink compatibility	Slurry electrodes and ionic liquid solution electrolytes
Printing resolution	Low resolution requirements: around 20 μ m
Device component thickness	Electrodes:20-100 μ m; Electrolyte:5-30 μ m
Device structure	Sandwich structure with a gel in the center
Manufacturing scale	Centimeter to Meter
Manufacturing cost	Cost competitive with other battery systems

High viscosity inks can be used for screen printing, and thick films (up to hundreds of microns) can be printed, which is a great advantage for functional device printing. Screen printing has been explored for printed electronics manufacturing, such as with solar cells[7], organic light-emitting devices[8], and field emission display[9], etc. Because most current screen printing equipment is semi-automatic, requiring manual control, it cannot be readily adapted for the roll-to-roll printing of solid-state batteries.

Inkjet printing has a great advantage of enabling personalized, high resolution, large format as well as short run printing [1][2]. However, it is still an expensive process, and highly limited by its printing speed. Current research on ink-jet printed electronics includes all-polymer transistor circuits[10], organic light emitting devices[11] for flexible displays, RFID tags[12], etc.

Traditional letterpress typically uses metal type and blocks for creating the printing surface, which makes it expensive and not suitable for multilayer structure printing, especially on metal foil substrates. Most of the letterpress machines have relatively slow speed of printing, which makes this approach less than ideal for high throughput battery fabrication.

Flexography, however, widely employs flexible, soft photopolymer or rubber plate, which is less expensive and more convenient to design, prototype and manufacture [1]. The flexible plates also make large format, multilayer device printing possible on a variety of wide web substrates such as metal foils. High ink drying speed due to utilization of low viscosity inks and the rotary principle of flexography allows for high throughput battery printing with web-fed roll-to-roll presses. The rubber, ceramic as well as photopolymer materials the ink goes through during the ink transfer process are chemically inert, so the functional battery inks are compatible with the roller mediums in flexographic press. The roll-to-roll battery printing is capable of being conveniently integrated with other roll-to-roll process of printing organic based solar cells and

electronics in future, for combined grid energy conversion and storage system manufacturing. Although flexography suffers from low printing resolution (up to 30 μ m), this is not a serious issue because zinc-based battery fabrication has a relatively low requirement for the film resolution. The use of flexography has been investigated for low cost, high volume production of ZnO nanowire devices[13] and micro-scale conductive networks[14].

2.3. Chapter Summary

A brief overview of current main printing technologies available has been provided in this chapter. Based on the criteria developed for printing process design and selection, a comparison of the technologies is made, as shown in Table 2.2. Flexography appears to be the most suitable roll-to-roll printing technology for grid scale zinc-based battery manufacturing.

Table 2.2. Comparisons of five major printing technologies available for grid scale, zinc-based battery fabrication in terms of printing process design and selection criteria.

Printing Process Design Criteria	Letterpress/ Flexography	Offset Lithography	Gravure Printing	Screen Printing	Ink-jet Printing
Ink compatibility	✓		✓	✓	✓
Printing resolution	✓	✓	✓	✓	✓
Device component thickness	✓		✓	✓	
Device structure	✓			✓	✓
Manufacturing scale	✓	✓	✓		
Manufacturing cost	✓		✓	✓	

Chapter References

- [1] H. Kipphan, "Handbook of Print Media: Technologies and Production Methods " 2001.
- [2] D. Bann, "The all new print production handbook," 2006.
- [3] F. Alliance, "Flextech Alliance Graph Expo Report 2012," May 2012.
- [4] D. A. Alsaïd, E. Rebrosova, M. Joyce, M. Rebroso, M. Z. Atashbar, and B. Bazuin, "Gravure Printing of ITO Transparent Electrodes for Applications in Flexible Electronics," *Display Technology, Journal of*, vol. 8, no. 7, pp. 391–396, 2012.
- [5] M. M. Voigt, R. C. I. Mackenzie, C. P. Yau, P. Atienzar, J. Dane, P. E. Keivanidis, D. D. C. Bradley, and J. Nelson, "Gravure printing for three subsequent solar cell layers of inverted structures on flexible substrates," *Solar Energy Materials and Solar Cells*, vol. 95, no. 2, pp. 731–734, Feb. 2011.
- [6] M. M. Voigt, A. Guite, D.-Y. Chung, R. U. A. Khan, A. J. Campbell, D. D. C. Bradley, F. Meng, J. H. G. Steinke, S. Tierney, I. McCulloch, H. Penxten, L. Lutsen, O. Douheret, J. Manca, U. Brokmann, K. Sönnichsen, D. Hülseberg, W. Bock, C. Barron,

- N. Blanckaert, S. Springer, J. Grupp, and A. Mosley, "Polymer Field-Effect Transistors Fabricated by the Sequential Gravure Printing of Polythiophene, Two Insulator Layers, and a Metal Ink Gate," *Adv. Funct. Mater.*, vol. 20, no. 2, pp. 239–246, Jan. 2010.
- [7] D. Vak, S. S. Kim, J. Jo, S.-H. Oh, S.-I. Na, J. Kim, and D.-Y. Kim, "Fabrication of organic bulk heterojunction solar cells by a spray deposition method for low-cost power generation," *Appl. Phys. Lett.*, vol. 91, no. 8, p. 081102, 2007.
- [8] D. A. Pardo, G. E. Jabbour, and N. Peyghambarian, "Application of Screen Printing in the Fabrication of Organic Light-Emitting Devices," *Advanced Materials*, vol. 12, no. 17, pp. 1249–1252, Sep. 2000.
- [9] L. Yukui, Z. Changchun, and L. Xinghui, "Field emission display with carbon nanotubes cathode: prepared by a screen-printing process," *Diamond and Related Materials*, vol. 11, no. 11, pp. 1845–1847, Nov. 2002.
- [10] H. Sirringhaus, "High-Resolution Inkjet Printing of All-Polymer Transistor Circuits," *Science*, vol. 290, no. 5499, pp. 2123–2126, Dec. 2000.
- [11] T. R. Hebner, C. C. Wu, D. Marcy, M. H. Lu, and J. C. Sturm, "Ink-jet printing of doped polymers for organic light emitting devices," *Appl. Phys. Lett.*, vol. 72, no. 5, pp. 519–521, 1998.
- [12] L. Yang, A. Rida, R. Vyas, and M. M. Tentzeris, "RFID Tag and RF Structures on a Paper Substrate Using Inkjet-Printing Technology," *Microwave Theory and Techniques, IEEE Transactions on*, vol. 55, no. 12, pp. 2894–2901, 2007.
- [13] J. S. Lloyd, C. M. Fung, D. Deganello, R. J. Wang, T. G. G. Maffei, S. P. Lau, and K. S. Teng, "Flexographic printing-assisted fabrication of ZnO nanowire devices," *Nanotechnology*, vol. 24, no. 19, p. 195602, Apr. 2013.
- [14] D. Deganello, J. A. Cherry, D. T. Gethin, and T. C. Claypole, "Patterning of micro-scale conductive networks using reel-to-reel flexographic printing," *Thin Solid Films*, vol. 518, no. 21, pp. 6113–6116, Aug. 2010.

Chapter 3

Functional Flexographic Inks for Battery Electrode Fabrication: Printability

3.1. Introduction

Functional inks for all the three components of the battery have been developed and dispenser printed directly on current collectors such as aluminum and stainless steel foils. The custom prototype dispenser-printer used in previous work is shown in Figure 3.1(a). It consisted of a computer controlled 3-axis stage with a pneumatic pressure controller to dispense composite materials from standard syringes. The syringes tips use hypodermic needles with various inner diameters ranging from 0.0826 mm to 3.810 mm, providing feature sizes between 5-200 μm with 1 μm precision both in the lateral and vertical dimensions[1]. Previous studies on the printed microbatteries as shown in Figure 3.1(b) [2], [3], electrochemical capacitors [4], [5], thermoelectric generators [6]-[12] as well as MEMS current sensors [13] have been conducted using this versatile prototype dispenser-printer. However, due to the limitations of this printer, only mm to cm scale batteries can be printed, even then at relatively low throughput rates, which is good for device prototyping but not for large-scale manufacturing.

A roll-to-roll printing process has therefore been proposed for the developed battery technology using commercially available flexographic printing presses. Roll-to-roll methods, such as flexographic or gravure printing, are traditionally used for printing packages, newspapers and magazines. In recent years, these methods are emerging as cost effective large-scale fabrication technologies in the semiconductor and solar industry with the development of organic electronic systems[14], [15]. The technology is currently still under development, with many research papers from academia and research institutions worldwide reporting progress such as roll-to-roll printed RFID tags[16], flexible polymer solar cells[17]-[20], OLED displays [21]-[24] and sensors[25], [26]. However, as far as the author knows, there has been no publication of research on roll-to-roll printing process for large-scale battery fabrication, such as to provide energy storage for all these flexible electronics applications. This is partly because of the limitation of traditional battery chemistries, most of which requires sophisticated manufacturing processes with well controlled inert environments[27], [28].

An illustration of the proposed zinc-based battery printing process is shown in Figure 3.2. The printing process consists of a four-station flexographic (flexo) press printing directly on unwound metal foil webs. At each station, the inks are first picked up by a fountain roller from the ink reservoir and transferred to the “anilox” roll. This roll plays a key role in controlling the printed feature thicknesses; it has engraved cells with controllable volumes (measured in the printing industry in billions of cubic microns per square inch (BCM)). The inks are then transferred to the plate cylinder, which consists of the desired printed features on a photopolymer. Finally, the impression cylinder applies a certain pressure to the web and the plate cylinder to print the ink. As was discussed, flexography was specifically selected because of its great advantages: it is a fully automatic process with high throughput rate; it is a mature wide web process - thus it is good for large-format device printing; it has flexible, soft plates thus it

has great flexibility with the printing substrates including metal foils; it can print at resolution as low as 20 μm -30 μm , which is good enough for battery applications. Gravure printing, on the other hand, is not good for foil substrate or layered structure printing due to its expensive, rigid metallic pattern plates[29].

In the battery fabrication application, each station is designed to print or deposit the developed functional inks for the cathode, electrolyte, anode and current collector in series, respectively. Printing plates are designed to print the various components of custom-sized batteries, forming a sandwich-structured battery. This roll-to-roll manufacturing technology is capable of fabricating batteries with capacities ranging from mA-hrs (microbatteries) to A-hrs (grid-scale batteries). Different manufacturing process parameters, such as printing speed, drying techniques, intensity and times should be strictly controlled between each printing station depending on the formulations of the functional ink to provide optimized printing quality and battery performance. But what turns out to be more critical is to develop inks with suitable fluidic properties for this unique roll-to-roll high-speed ink transfer process in order to achieve excellent printing quality.

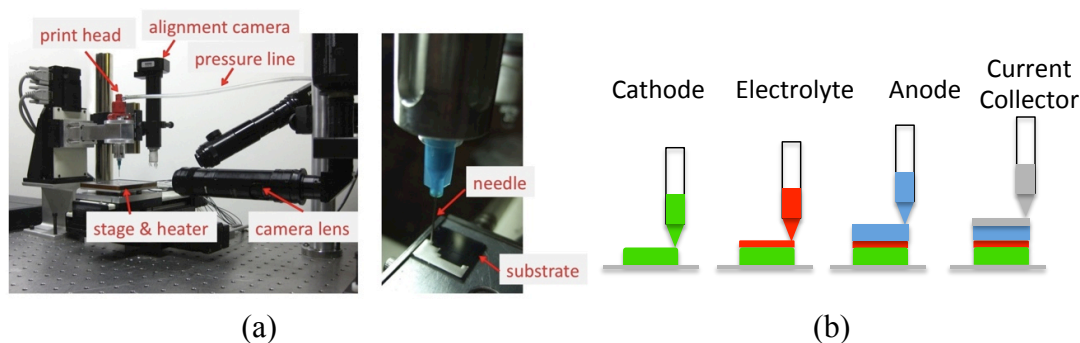


Figure 3.1. (a) Custom dispenser printer; (b) Dispenser printing solid-state batteries. (adapted from [2])

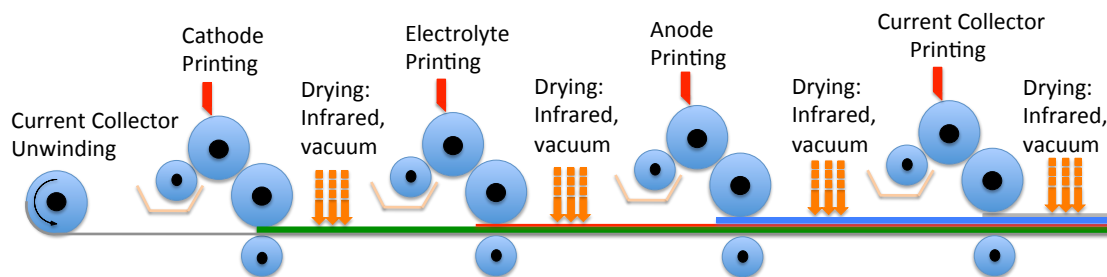


Figure 3.2. Proposed multi-station flexographic printing process for large-scale battery production.

3.2. Flexographic Printing Process and Ink Design

Dispenser printing is an ink extrusion method based on well-controlled compressed air pressure, thus the ink viscosities are in a large range between 0.1 Pa·s and 10 Pa·s[3]. A variety of

functional inks, including non-newtonian electrode slurries and newtonian solutions, all show excellent printing qualities achieved by controlling the process parameters for the dispenser printer. The printing speed, drop spacing, air pressure, and needle configurations show significant influence on the final printing precision and repeatability.

Flexography however requires much more careful design of its inks, due to the complex nature of the printing process as illustrated in Figure 3.3. Large volumes of inks (in liters) are typically needed to fill the ink reservoir for a cost effective roll-to-roll printing process, so the inks need to maintain high dispersing qualities and have minimal aging effect. Because the inks need to be transferred effectively at high speed from the ink reservoir to the substrate through multiple rollers and media, including rubber fountain rollers, ceramic anilox rollers as well as photopolymer plates, the viscosity and wetting properties must be well adjusted so that a high ink transfer rate and accuracy are achieved. Once the inks are transferred to a variety of substrates, both a compressive force from the impression cylinder as well as a shear force due to the relative motion of the substrates and plates are applied to the inks, so the inks need also to have proper structural properties to form desired pattern with high accuracy. Prior work at UCB has mostly employed organic-based inks. However because flexographic printing presses are designed for large volume manufacturing, aqueous-based inks are highly desired, compared to traditional organic solvent based formulations for battery chemistry and have therefore been the subject of this investigation.

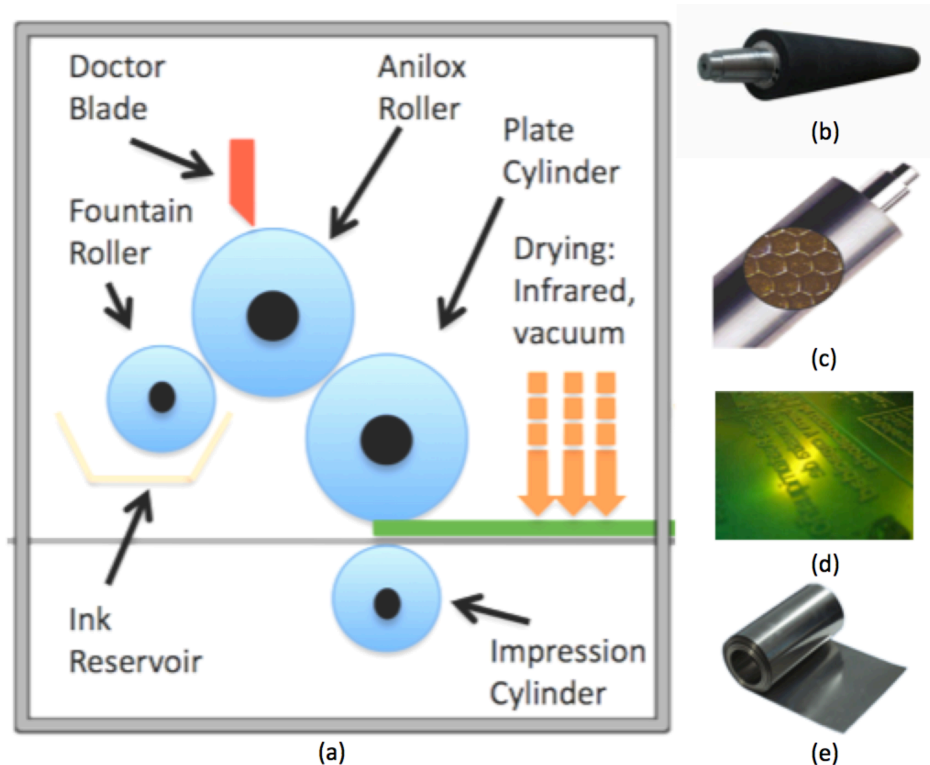


Figure 3.3. (a) Ink transfer process happens between multiple types of rollers before successful deposition; (b) Rubber fountain roller; (c) Anilox roller with engraved ceramic surface; (d) Photopolymer plates mounted on the plate cylinder; (e) Stainless steel foils where inks are finally deposited with plate patterns.

Typical commercial flexographic printing presses are equipped with multiple printing stations, which are not convenient for initial research and development at the laboratory stage. Consequently, an automatic single-color flexographic press (DOR-320A® from Ruian Inc.) has been set up in our research lab to study a single-layer flexographic printing process as well as the drying processes. It is a complete printing system with web winding, web rewinding and a controllable infrared drying station. Printing process parameters are easily adjustable; the printing speeds vary from 0 to 50 m/min, the printing widths vary from 0.05 to 0.31m, and the IR temperatures vary from 0 to 150°C. At an even smaller scale, an automated ink proofing system (Perfect Proofer ®) at the Graphic Communication Departments in California Polytechnic State University San Luis Obispo was used for developing and testing battery inks at the milli-liter scale. Instead of using ink reservoir and wide web substrate, manual ink dispensing test method was utilized for timesaving purposes and to minimize expenditure on inks. With accurately controlled inter-roller pressures and printing speed, it is easy to scale up the fabrication process once proof of a printable ink is obtained. The three representative pieces of equipment are shown in Figure 3.4.

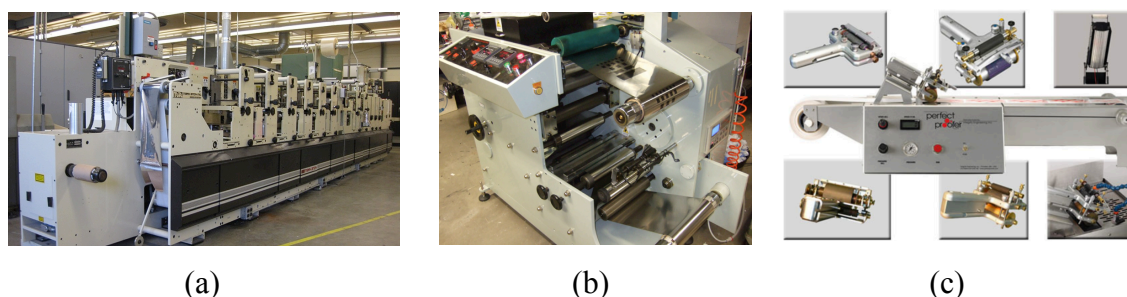


Figure 3.4. (a) Six-station flexographic press at Cal Poly State University; (b) Single-station flexographic printer at UC Berkeley; (c) Flexographic ink printability tester at Cal Poly State University.

Dispenser printable inks developed previously show various poor printing qualities. Among them, poor wetting shown in Figure 3.5(b) was typically due to the high surface tension of the inks relative to the low surface energy of the foil substrate, especially for some aqueous-based composite inks; Non-uniformity as shown in Figure 3.5(c) happened frequently with low viscosity inks with poor structural properties. Active particles in the cathode slurry were easily squeezed to the edge of the square on the stainless steel substrate instead of spreading uniformly. Comparing to what we obtained from using commercial graphic black inks (inks used for printing newspapers etc) in Figure 3.5(a), it is concluded that substantial ink fluidic property analysis and improvements, beyond inks developed for dispenser printing, are necessary to achieve high quality functional thick films from flexographic printing. In the following sections, the ink rheology and wettability as well as dispersion will be discussed. Finally, physical characterizations of the dried films were performed and correlated to the ink formulations and properties.

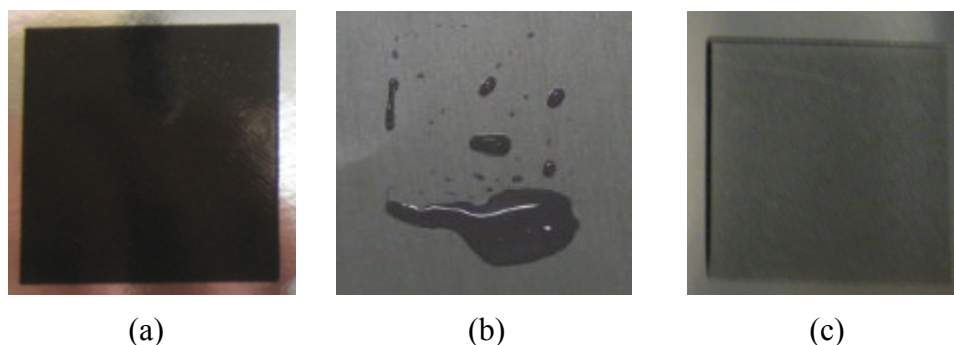


Figure 3.5. (a) Films printed from commercial flexographic inks on stainless steel foil; (b) poor wetting properties with aqueous based cathode inks on stainless steel foil; (c) non-uniform films printed with organic solvent based cathode inks.

3.3. Aqueous Functional Inks

Most of the work in this dissertation was focused on printing and developing cathode slurry inks typically consisting of manganese dioxide (MnO_2) powder, conductive carbon powder, a polymeric binder material as well as a solvent. However, the key criteria that were established apply to other ink formulation such as the inks for anode and current collector, and even potential slurry electrolytes.

In the previous work, a cathode slurry was developed based on traditional Poly(vinylidene fluoride-co-hexafluoropropene) (PVDF-HFP) binding material, which requires volatile *N*-methyl- 2-pyrrolidone (NMP) as the solvent[2]. The main function of the binder was to form inter-particle bridges/connections to promote particle adhesion after solvent evaporation. However, water-based flexographic inks are highly desirable for cost reduction as well as more environmentally friendly processing with diminished concerns about flammability and impact on the health of workers. This is particularly important for large scale printing processes due to large volumes of solvent evaporation into the ambient environment. Because water has lower normal boiling point than many organic solvents used for batteries, faster drying at lower drying temperature thereby become a reality, which is essential for roll-to-roll high production rate process. Even in the graphic printing industry, water-based inks with new surfactant, dispersant and formulations have quickly replaced traditional organic solvents based inks, due to the strict environmental regulations concerning using volatile organic compounds (VOCs) everywhere from paint to plastic manufacture[30].

Water-soluble binder systems such as sodium salt of carboxymethyl cellulose (CMC) and styrene-butadiene rubber (SBR) have been recently introduced in the manufacturing of lithium ion battery electrodes[31]-[33]. Typical chemical structures of CMC and SBR are illustrated in Figure 3.7. SBR is typically used as the primary binder for the composite electrode and CMC is used as a thickening/setting agent. This work explores the application of various CMC/SBR binder formulations as well as single SBR binding solution with high viscosities, in the zinc-based battery chemistry and electrode fabrication using flexographic printing technology. A certain formulation of the composite ink proves to give an optimized high film printing quality and electrochemical performance.

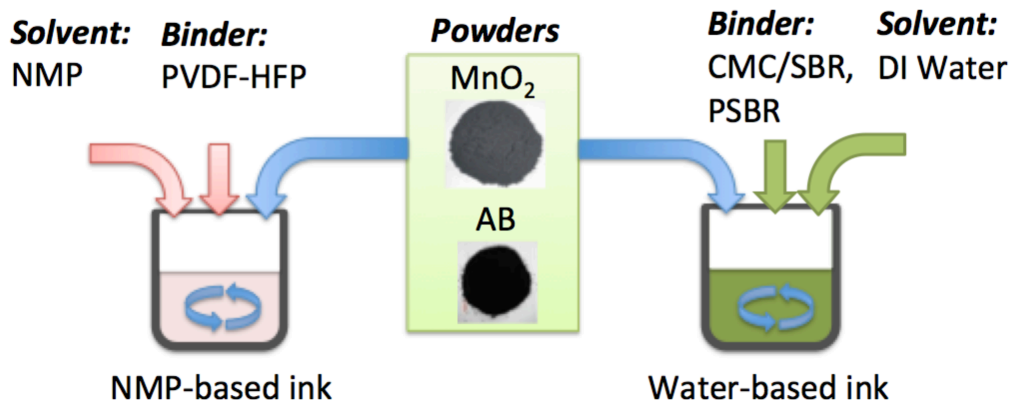


Figure 3.6. Cathode ink formulations based on different binders: PVDF-HFP is a traditional organic solvent soluble binder widely used in lithium ion and zinc battery electrodes with proven performance; CMC/SBR is a relatively new water-soluble binder with high promise for large-scale manufacturing.

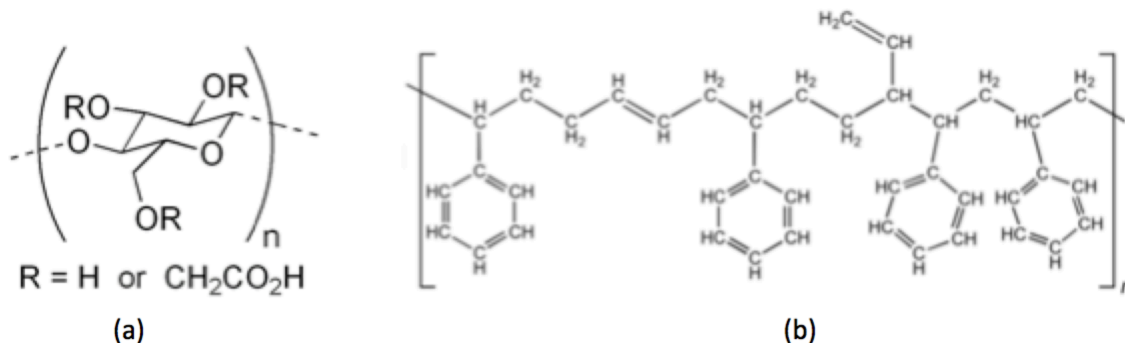


Figure 3.7. Chemical structures of carboxymethyl cellulose (CMC) (a) and styrene-butadiene rubber (SBR) (b).

3.4. Ink Rheology

3.4.1. Ink Preparation and Rheological Measurements

Five main types of inks were used for rheological characterizations and comparisons:

1. Commercial flexographic graphic inks (Performa Ink System) were directly ordered from Actega WIT, Inc. The specific graphic ink used for this work is water-based black ink.
2. A type of composite ink based on commercial extender solution was developed with active cathode powders. The formulation includes 90 wt% activated MnO_2 powder with particle sizes $< 5 \mu\text{m}$ (Sigma-Aldrich), 6 wt% acetylene black (AB) conductive filler (Alfa Aesar) and 4 wt% extender solutions.
3. The PVDF-HFP based MnO_2 ink contains 90 wt% activated MnO_2 powder, 6 wt% acetylene black and 4 wt% PVDF-HFP (Kynar Flex 2801). The PVDF-HFP solution was first formed by dissolving one part polymer powder in fifty parts NMP solvents (Sigma Aldrich) before mixing

with MnO₂ and AB powders. The mixing was done by placing the ink jars in a high-energy planetary ball mill (Torrey Hills ND 0.4L) and operating at rotational speeds of 210-280 rpm for 180 min.

4. The CMC/SBR based MnO₂ inks were composed of 90 wt% activated MnO₂ powder, 6 wt% acetylene black (AB), 2 wt% carboxymethyl cellulose, sodium salt (MTI) and 2 wt% styrene-butadiene rubber (MTI). The CMC solution was formed by dissolving one part of powder in ninety parts of DI water. The SBR solution used was a 50% emulsion as received.

5. The PSBR based MnO₂ inks were composed of 90 wt% activated MnO₂ powder, 6 wt% acetylene black (AB), and 4 wt% modified styrene-butadiene rubber (PSBR-100 from Tragray). This PSBR emulsion solution is more viscous than the typical SBR from MTI and provides high binding strength according to the emulsion manufacturer. Water-based ink with dispersing agents was formed by adding one part commercial dispersing agent for aqueous systems (W-28 from Nuosperse) to 7 parts MnO₂ and AB powders. The specific dispersing agent (a non-ionic surfactant) plays a role of being separator and preferentially adsorbs on the powder surface to provide an effective steric layer, which prevents agglomeration and sedimentation.

A series of rheological tests were performed at 25°C using a rheometer (HAAKE Rheoscope) with a standard cone and plate geometry (cone diameter = 60 mm, cone angle = 2° and gap = 150 μm). Among the tests performed in this study were steady state viscosity and yield stress measurements, introduced in the following sections. The steady state viscosity measurements established the thixotropic (shear thinning) behavior of the composite cathode inks, whereas the yield stress measurement were used to study the ink internal network structure. By performing both of the tests, the effects of polymeric binder and solvent type on the overall fluidic and structural properties of the flexographic inks were evaluated and compared.

3.4.2. Steady-state Viscosity

Classic viscosity-shear rate curves were obtained using the steady-state viscosity test. All composite ink samples (typically around 5ml for each experiment) were initially pre-sheared at 0.1 1/s for 60s, which was followed by a 60s equilibration time before conducting the viscosity measurements at shear rate ranges of 0.1 1/s to 1000 1/s increasingly, and each experiment was repeated at least three times for obtaining consistent results. As shown in Figure 3.8, all the inks demonstrate shear-thinning behavior to varying degrees. At low shear rate range, the PVDF-HFP and PSBR based inks show higher viscosity than other three inks including commercial flexographic black inks, CMC/SBR based inks as well as commercial extender based inks. All viscosities decrease with increasing shear rate, and keep below 1 Pa•s from 10 1/s to 1000 1/s, which is the typical operating shear rate range for a high speed flexographic press. This indicates that all the inks should have no problem with transfer processes from ink reservoir to foil substrates.

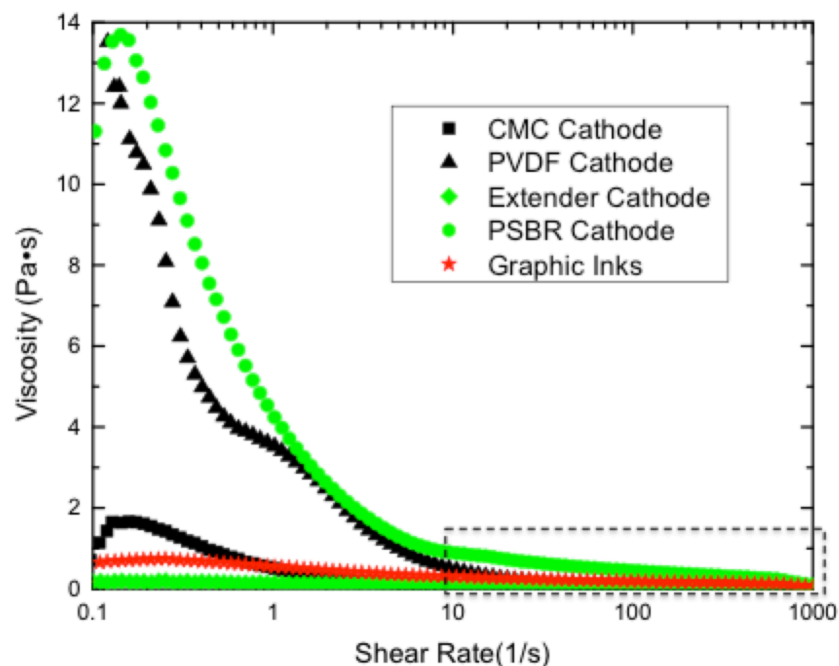


Figure 3.8. Viscosity as a function of shear rate for five different types of inks (four developed in this investigation for functional flexographic printing).

For comparison, steady state measurements of ionic liquid polymer electrolyte solutions were also conducted. The polymer electrolyte solution is composed of equal weight ratios of PVDF-HFP and BMIM+ Tf⁻ ionic liquid electrolyte. Samples with different ratios of the solvent to the PVDF-HFP binder were used to measured viscosity. As shown in Figure 3.9, most of the

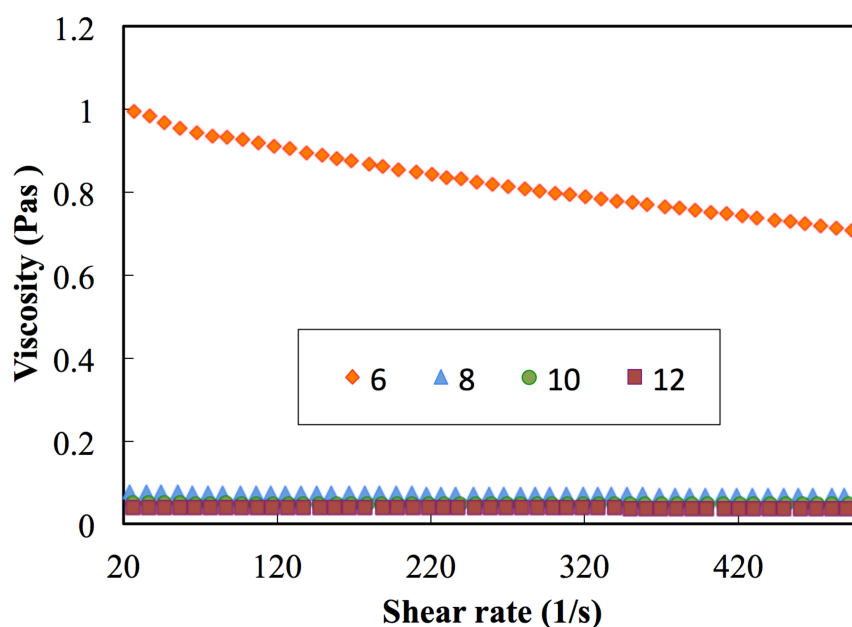


Figure 3.9. Steady-state viscosity of polymer electrolyte solutions. The values indicate four electrolyte solutions with different weight ratios of NMP solvent to the PVDF-HFP binder.

polymer electrolytes show Newtonian behavior with constant low viscosities within the range of shear rates applied. However, shear-thinning behavior is exhibited by the high viscosity sample. The low viscosity values at a wide range of shear rates show that the electrolyte solution should also transfer between rollers well.

The plots of shear stress-shear rate from the same sets of experiments are shown in Figure 3.10. The critical shear stress is reached at the peak of each curve. Both the CMC/SBR based cathode slurry and the PVDF-HFP based slurry showed much lower critical shear stress than other three inks, which gave much better printing quality as will be shown in the following sections. For “structural” fluids like these flexographic composite inks, the critical shear stress indicates the minimum shear stress required to initiate the deformation in the fluids. Below this critical stress, the ink behaves more as a solid, absorbing the stress without flow[34], [35]. But once the threshold of critical shear stress has been reached, the material yields to flow. The yield stress could thus be directly related to the structural behavior of flexographic inks under shear and compressive stress after they were transferred to the substrate. A standard way to measure the yield stress is described in the next section.

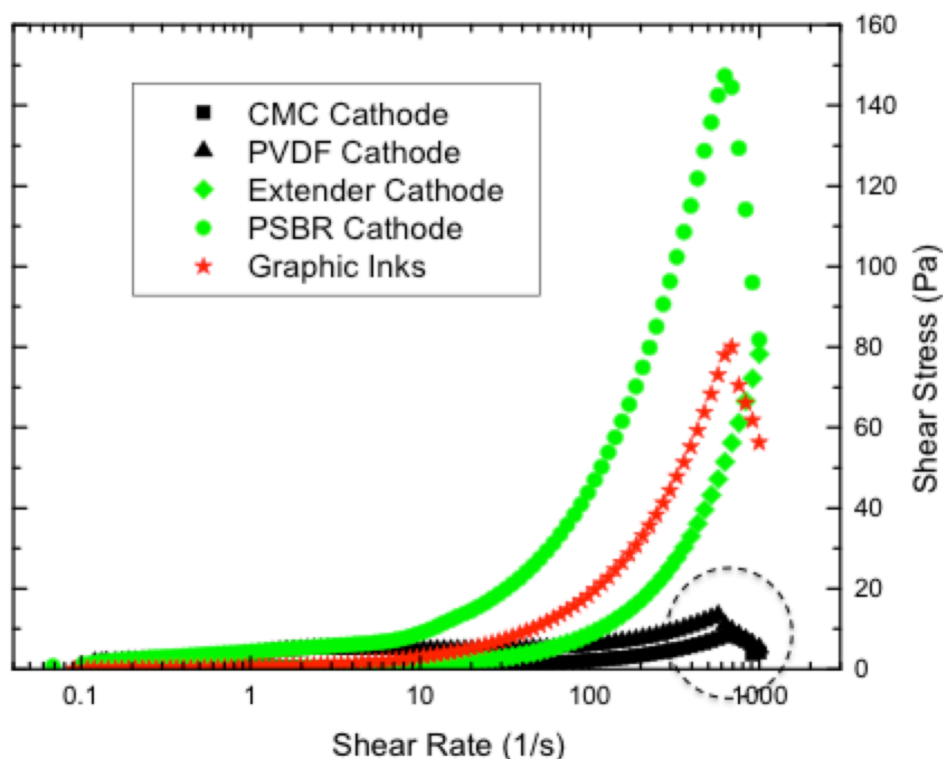


Figure 3.10. Shear stress as a function of shear rate for five different types of inks developed for flexographic printing.

3.4.3. Yield Stress Measurement

To determine the yield stress, five ink samples were initially pre-sheared for 60 seconds at 1 Pa followed by a 60 second equilibration time before performing a stress sweep from 1 to 300 Pa, over a time period of 300 seconds as shown in Figure 3.11. This controlled stress test was

repeated three times for each sample to obtain average values and standard deviations. As discussed earlier, yield stress is a critical parameter, which determines the flexographic ink transition point from a solid-like behavior to a liquid-like behavior in which the composite material's internal network structure starts to break down, and the material begins to flow[35], [36]. The yield stress indicates the relative structural strength of the particle network within the slurry ink and is closely related to the elasticity of the ink. As shown in Figure 3.12 below, due to the low yield stress of CMC/SBR based cathode slurry and the PVDF-HFP based slurry inks, their internal structure tends to easily get broken. Once a pressure or a shear stress is applied to the inks that have been transferred to the substrate, active particles could easily be squeezed to the edge of the film causing high non-uniformity. An even worse situation would be that inks flow without control at the edge of the printed area so that the film shape becomes irregular and pattern transfer becomes inaccurate. On the other hand, the PSBR based cathode slurry had similar yield stress as with commercial flexographic inks as well as extender based electrode inks, so it also achieved very good flexographic printability.

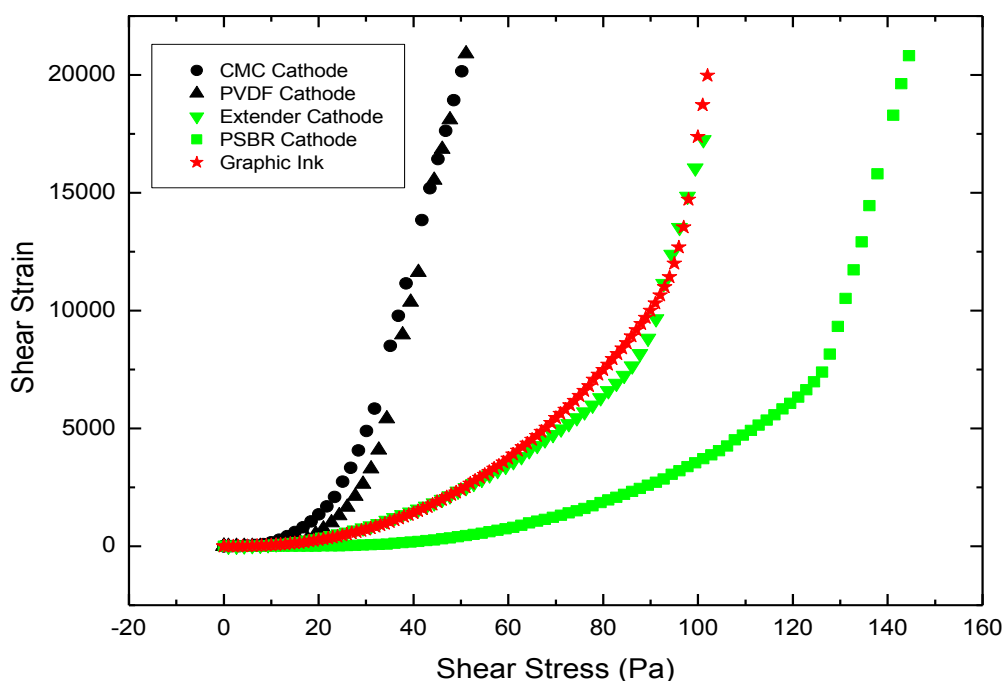


Figure 3.11. Shear strain versus shear stress for controlled stress sweep measurements for five different types of inks. The critical shear stress is reached at the end of each curve.

In most of studies of the rheology of fluids, it is quite common to just run steady-state viscosity measurements or even just simple single-point viscosity measurement (at a only one shear rate). For flexographic ink development, a yield stress study is equally, if not more, important due to the nature of the complicated printing process itself. It is concluded that both the viscosity and yield stress of a functional flexographic ink need to be well adjusted to guarantee there are both of a smooth ink flow and an accurate ink deposition as well as pattern transfer. The latter then will also be closely related what will be discussed next: ink wetting properties.

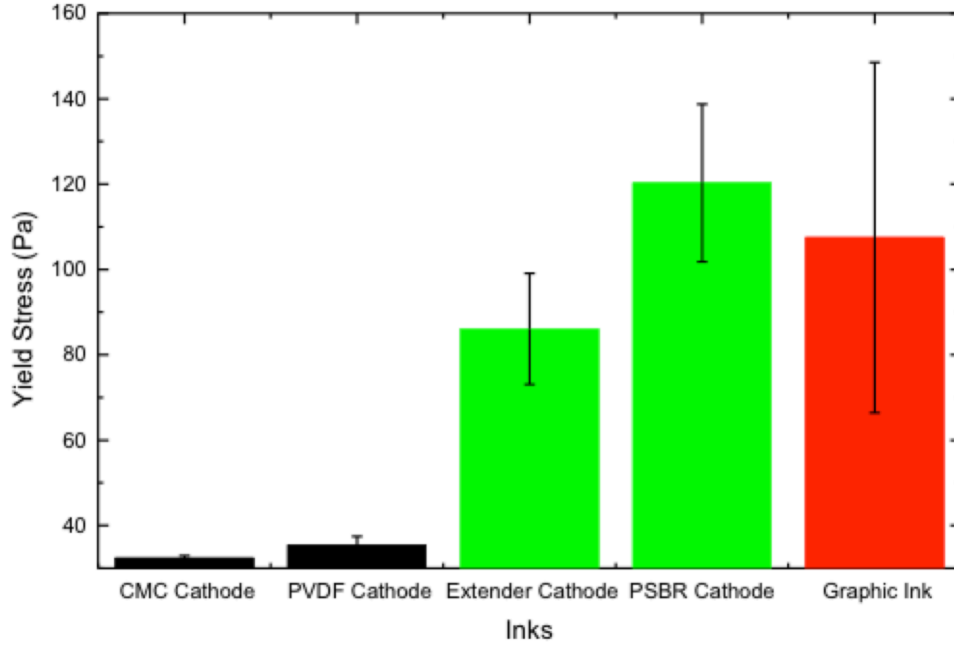


Figure 3.12. Yield stress for five different types of inks developed for flexographic printing.

3.5. Wetting Properties

3.5.1. Introduction

The wetting properties of the functional inks on various substrates are important because they greatly influence the ink adhesion and final feature formation after the flexographic ink gets transferred to the substrates, either before or after the stresses is released from the inks.

The fluid drop spreading on a solid substrate surface is determined by a competition between adhesive forces at the interface of liquid and solid as well as cohesive forces within the liquid[37], [38]. The interfacial adhesive forces promote drop spreading, while the internal cohesive forces within the liquid work against it. At equilibrium, the balance of forces on the liquid at the three-phase line (Figure 3.13) can be described using the Young's equation[39]:

$$\gamma_{sa} = \gamma_{sl} + \gamma_{la} \cos \theta \quad (1)$$

where θ is the Young's contact angle; γ_{sa} , γ_{sl} and γ_{la} represent the solid-air, solid-liquid and liquid-air interfacial tensions, respectively.

A spreading coefficient, S , is widely used for predicting whether a liquid drop will spontaneously spread on a solid substrate surface [40] and is defined as

$$S = \gamma_{sa} - (\gamma_{sl} + \gamma_{la}) \quad (2)$$

When $S > 0$, the ink spreading process is spontaneous and a uniform, thin liquid film will be formed at the equilibrium state; when $S < 0$, the liquid will eventually form a drop with above zero contact angles.

From an energy perspective, the final feature is determined by the surface energy of both of the fluid and the solid. Changing one or several of these surface energy components makes it possible to control the system to attain the wetting properties desired for a given system. Thus in the printing industry, to achieve the desired wetting properties, printers typically try to adjust the ink surface tension (more popular term than surface energy for fluids) through adding surfactant chemicals to the ink formulations; or modify the substrate surface energy by doing some surface pretreatment before printing, such as corona discharge treatment.

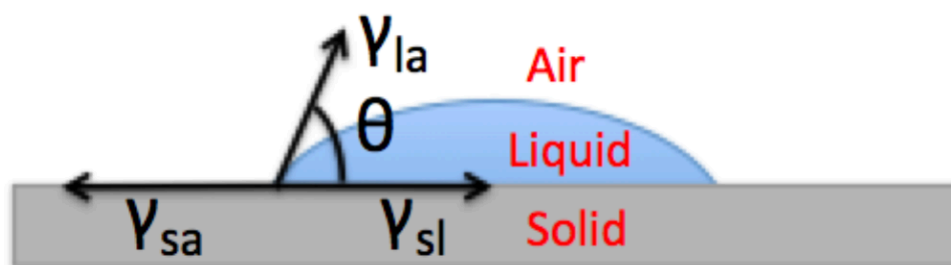


Figure 3.13. The balance of forces at equilibrium on the liquid drop at a three-phase line.

For the flexographically printed battery research, the main focus is on the ink formulations optimization for functional ink wettability improvement. Both ink surface tension characterizations and contact angle measurements will be presented here. Because of the limitations of equipment available for surface corona discharge pretreatment, no large spool of foils could be prepared for roll-to-roll printing tests.

3.5.2. Surface Tension of Inks

Surface tension of a liquid is believed to be caused by the unbalanced forces of liquid molecules at the surface when exposed to air (a more general term would be interfacial tension with any other phase/medium)[41]. As illustrated in the following Figure 3.14, inside a pure liquid or homogeneous solution, each molecule in the bulk is pulled equally in every direction by neighboring liquid molecules, which generally result in a net force of zero. However, the molecules exposed at the liquid surface to air do not have the same kind of neighboring molecules in all directions to provide a balanced force. Thus, the molecules at the surface tend to be pulled inward by the unbalanced force and create so-called “surface tension”. Because of this, a liquid drop, such as an ink, typically tends to contract its surface area by the cohesive force to reach its lowest surface free energy.

For various ink characterizations, the surface tension of ink measures the cohesive force present at the solution surface and it directly quantifies the wetting characteristic of the ink surface. All surface tension measurements were performed using a KSV Sigma 701 tensiometer using the Wilhelmy plate method[42]. Surface tension is mathematically defined as the amount of work that must be done in order to create unit area of surface. The SI units are J/m^2 (or N/m), but in this paper values are expressed in more commonly used unit mN/m .

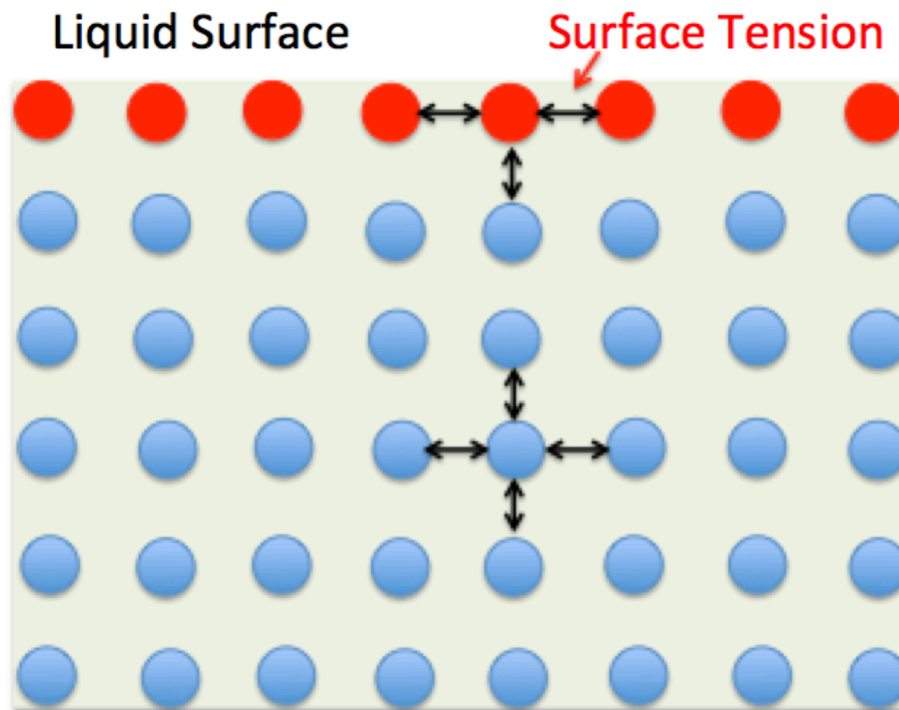


Figure 3.14. Illustration of surface tension caused by the unbalanced forces of liquid molecules at the surface.

The surface tensions of various inks made using the previously described formulations are presented in Figure 3.15 below. Both the NMP-based and water-based MnO_2 inks with dispersing agent have shown similar surface tension values to commercial flexographic inks, which are significantly lower than what is measured for pure water as well as water based CMC/SBR inks. The value for NMP-based inks is low because the organic solvent, NMP, mainly exposed at the surface of the slurry has much lower surface tension than pure water (72 mN/m). However, by adding dispersing agent consisting of a combination of non-ionic surfactants, even water-based slurry could achieve lower surface tension. The results also indicate the two most effective approaches in order to improving wetting properties of the inks: by controlling the contents of solvent or adding proper amount of surfactant additives. The detailed role of surfactant will be discussed.

The surface tension of ionic liquid electrolyte based on NMP solvent was also studied and shown in Figure 3.16. All the measured average surface tension values are between 30 mN/m and 35 mN/m, with only slight change due to the solvent content changes. It is thus concluded that NMP based electrolyte should have good wettability on general printing substrates. However, a solvent trapping system will need to be built for using organic solvent-based functional inks for large-scale flexographic printing.

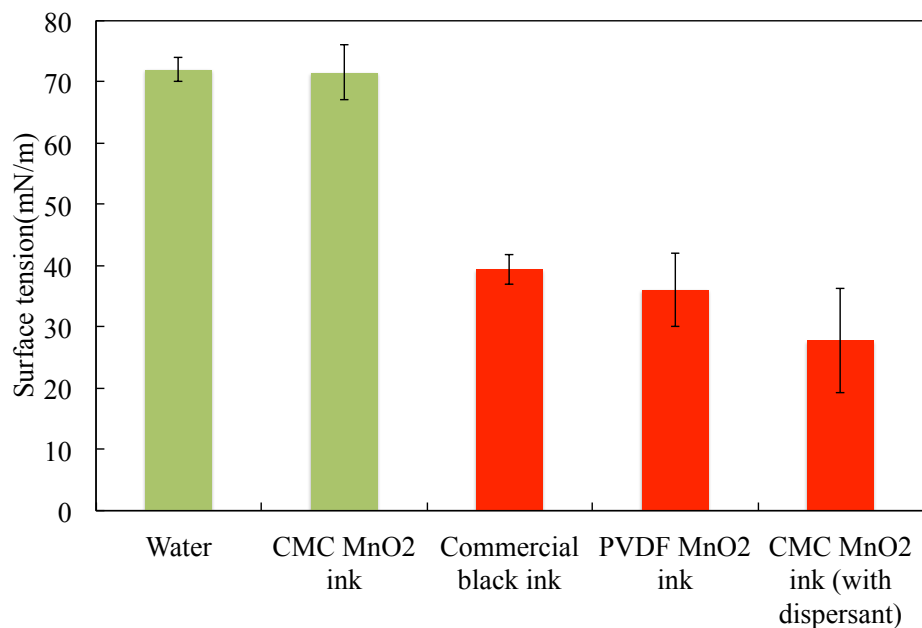


Figure 3.15. Surface tensions of water, water-based CMC/SBR ink slurry, a commercial water-based black ink, NMP-based PVDF ink slurry and water-based CMC/SBR ink slurry with dispersants. Dispersing agent has significantly improved the wetting properties of water-based ink on stainless steel substrate.

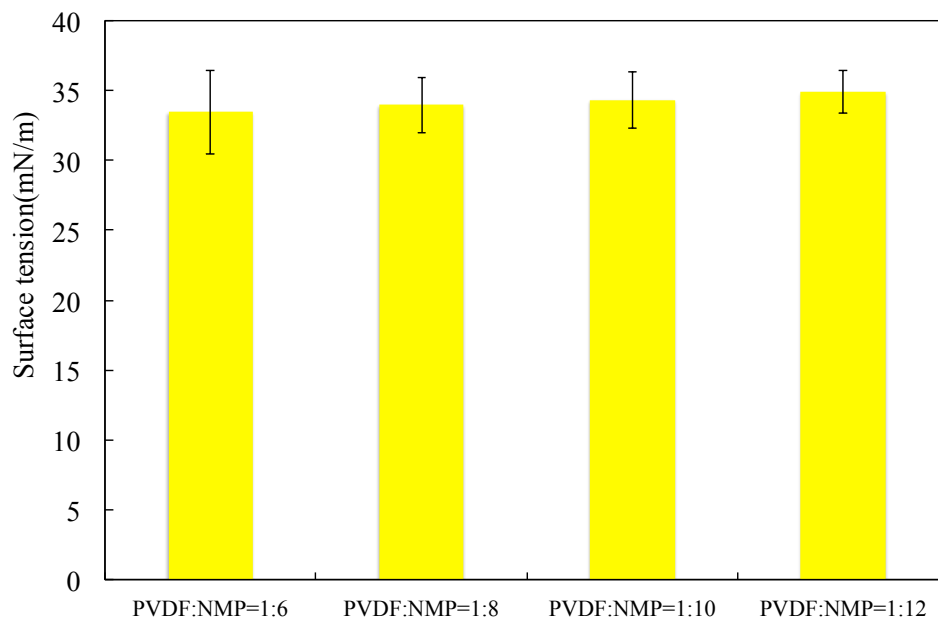


Figure 3.16. Surface tension varies little for polymer electrolyte inks with different amounts of solvents. With the solvent contents increase, surface tension of the electrolyte also increases slightly.

3.5.3. Contact Angle Measurements

While surface tension values can give a general idea of the liquid surface properties exposed to the air phase, the contact angle measurements have the advantage of giving a more intuitive assessment of the flexographic ink's wetting characteristics on specific substrates, providing information on the interaction between the ink and the substrate interface. Typically small contact angles (less than 90°) denote high grade of ink wettability while large contact angles (greater than 90°) stand for a low grade of ink wetting property.

Contact angles can be measured using various methods, including the telescope-goniometer method and the Wilhelmy balance method[43]. In this research, contact angle measurements of the various inks were performed using a photographic method using the custom-built dispenser printer, a technique based on the goniometer method. ImageJ software was used for captured image post-processing and contact angle analysis.

Figure 3.16 compares the contact angles of the inks on various substrates. The photopolymer on the plate cylinder plays a key roll in transferring the ink from the plate cylinder to the substrate. Good ink transfer requires similar wettability of the transferred ink on both the photopolymer and the metal substrate while maintaining low-viscosity to promote flow. In this experiment, the photopolymer plate was custom designed and ordered from Flexographic Printing Plate Co., Inc. Both the aluminum and stainless steel (type 304-full hard temper, $50\mu\text{m}$ thick) foils used in the following chapters are from McMaster-Carr. NMP based cathode ink have similar contact angles measured with commercial graphic inks on all three substrates, which implies wetting properties are good. The water-based CMC/SBR inks without dispersants, as shown from Figure 3.8, cannot be printed well due to its high contact angles.

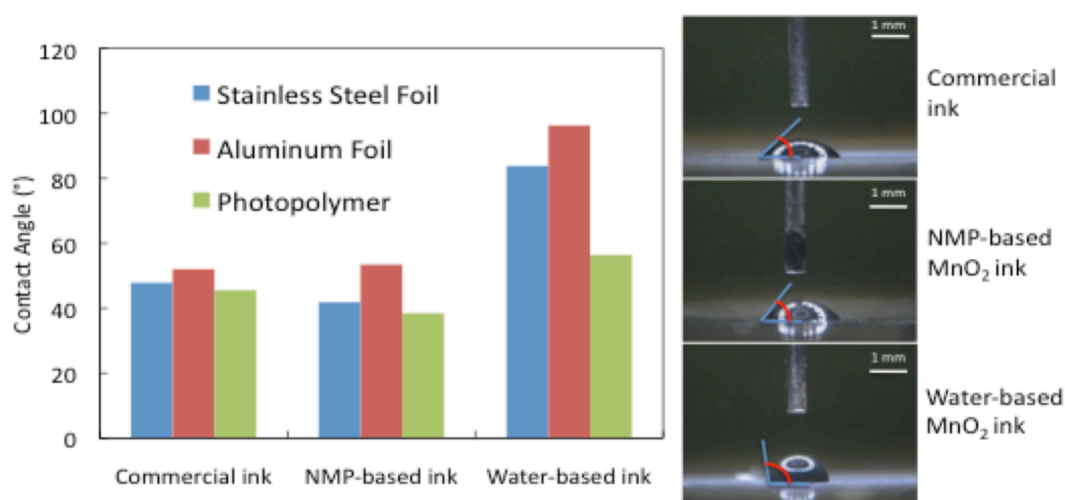


Figure 3.16. Contact angles of commercial water-based ink, NMP-based PVDF ink slurry, and water-based CMC/SBR ink slurry; the three figures on the right show the contact angle measurement using our custom dispenser print on an aluminum foil for four types of inks.

From Figure 3.17, however, by adding just 4 wt% of the dispersing agent to the water-based slurry significantly reduced the contact angles. Future work on optimization of the type and quantity of dispersants will be beneficial to obtaining the desired functional inks.

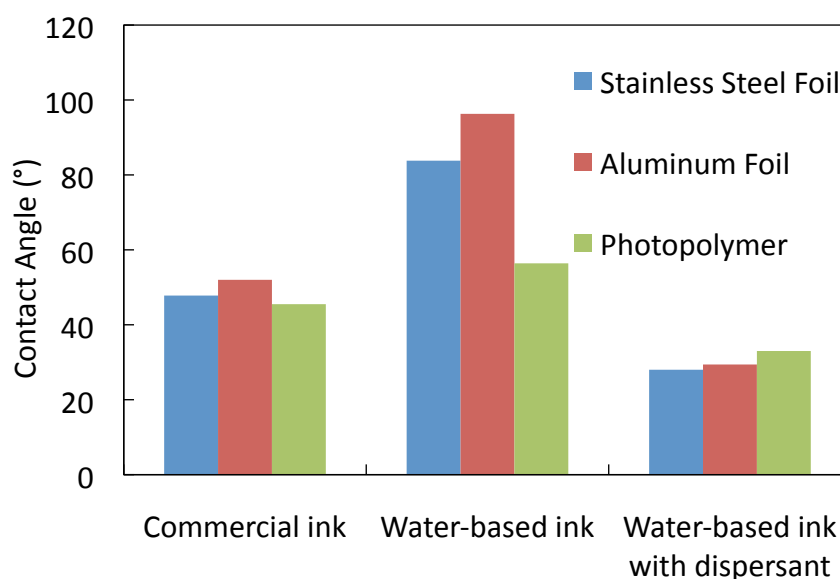


Figure 3.17. Contact angles comparison of commercial water-based ink, water-based CMC/SBR ink slurry and water-based CMC/SBR ink slurry with 4% dispersing agent.

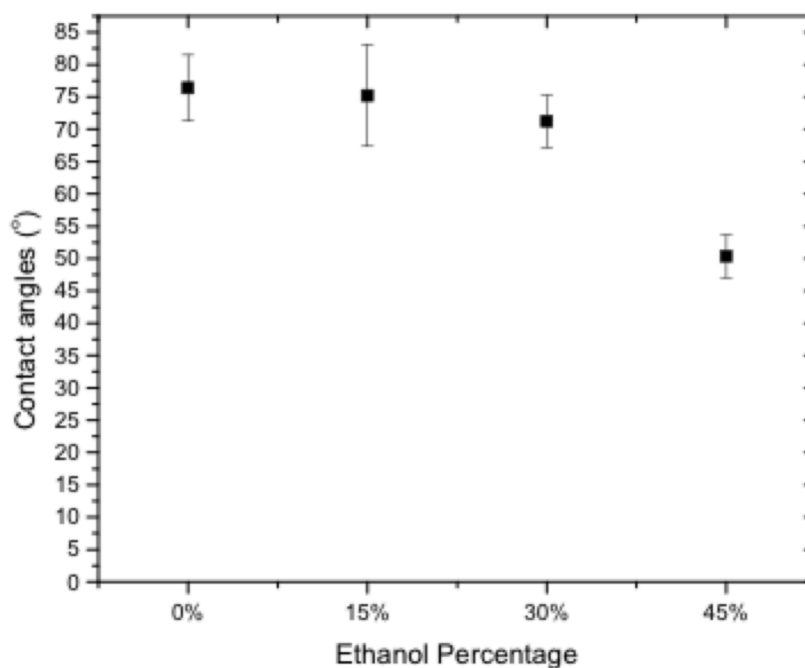


Figure 3.18. Contact angles of water-based CMC/SBR inks on stainless steel substrate were greatly reduced by adding ethanol as an additive solvent.

In Figure 3.18, another effective approach to reduce the surface tension and contact angles of the existing aqueous cathode inks was shown. By adding a certain amount of organic solvent, such as ethanol or acetone, the contact angles on stainless steel foil were reduced to what could be achieved by commercial flexographic inks. Of course, this is not a preferred method, as it is a

return to the volatile organic solvent-based slurry inks. For small scale printing in controllable environments, this approach might be considered.

The initial contact angles of the electrolyte on a printed MnO_2 cathode layer were measured and shown in Figure 3.19. The low contact angles suggest good wetting properties of the electrolyte with several electrolyte ink formulations by changing the organic solvent contents. The dynamic contact angle measurements were also conducted based on the video recording during ink drop spreading process on the cathode. Instead of coming to equilibrium state quickly, the contact angle further decreases over time due to the penetration of the electrolyte layer into the porous electrode. This effect has been consistently observed and measured as seen in Figure 3.19.

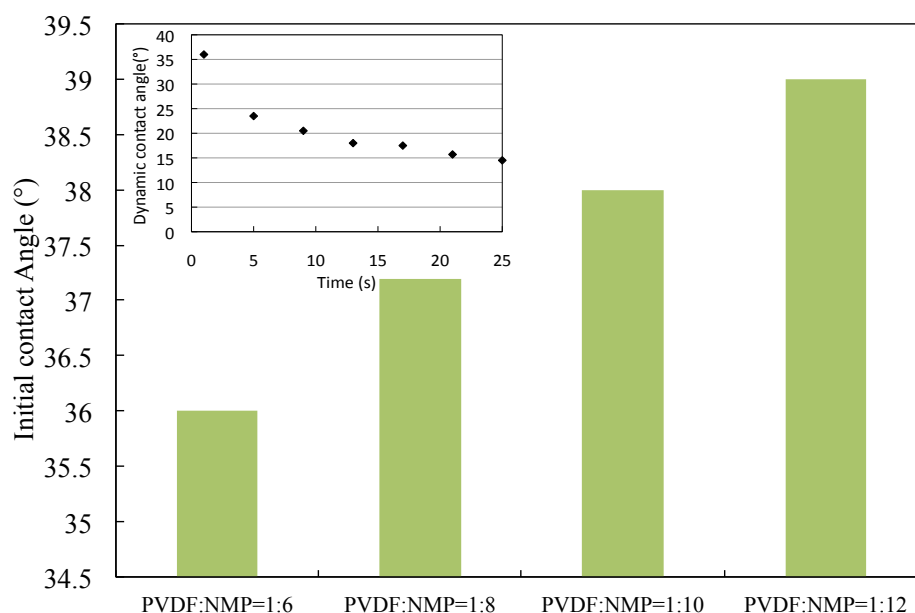


Figure 3.19. Initial contact angles of polymer electrolytes and the penetration and typical spreading behavior of the ink on porous MnO_2 electrode.

3.6. Ink Dispersing Qualities

Because flexography is typically a long-lasting, large volume ink printing process, high quality inks require good ink pigment dispersion, fine particle shape and size distribution as well as long-term stabilization of the dispersed particles in the ink[44], [45]. Figure 3.20 below shows the representative commercial ink making mechanism, which include pigment wetting stage, grinding stage for dispersion as well as the final stabilization of the pigment suspension [45]. The graphic ink dispersion process is a high-energy process when the pigment agglomerates or aggregates are mechanically broken up into smaller constituents, which then uniformly distributed in the ink vehicle. This is usually accomplished by mechanical impact and shear action provided by high impact mill equipment. Once dispersed, the primary particles then tend to re-agglomerate, forming so-called “flocs” typically due to the attractive van der Waals forces.

So in order to maintain the well-dispersed state, dispersing agent additives with stabilizing molecules are needed to achieve pigment stabilization.

According to the different types of additive dispersing agents and of repulsive force mechanisms, there are two classes of stabilization[45]: Electrostatic stabilization by adding ionic surfactants to form Coulomb-repulsion of the same charged particles and steric stabilization by adding non-ionic surfactant polymers covering the particles, which helps to create physical space separation based on they hydrophilicity or hydrophobicity of the polymer molecules. Depending on the contents of graphic ink pigments, resins and solvents, proper surfactant additives need to be selected to achieve excellent ink dispersing quality and stability.

Similarly, to develop good functional flexographic inks for battery or other energy applications, strict control of the ink dispersion and stabilization process is highly important. For example, high-speed planetary ball milling has been employed for cathode ink mixing and dispersion and shows improved ink uniformity and printability compared to inks prepared just using low power vortex mixer. In the present work a certain amount of dispersing agent (non-ionic surfactant) was also added to look at its effect on ink formulation performances.

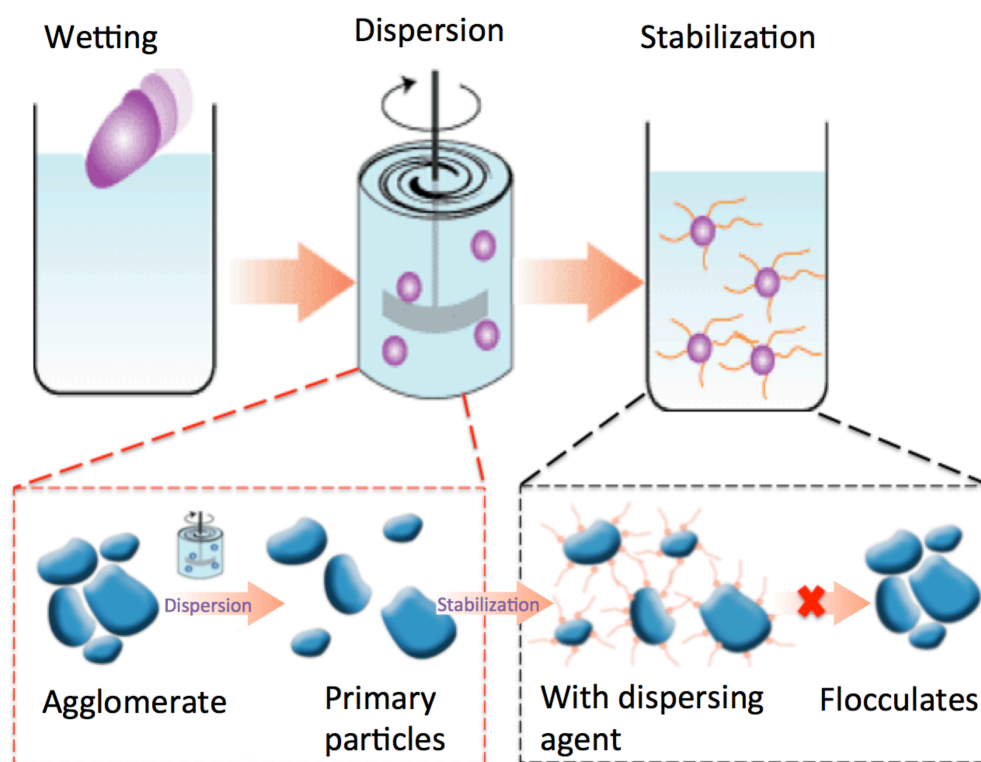


Figure 3.20. The mechanisms of typical pigments dispersion in liquid inks to produce stable suspension (adapted from [45])

Figure 3.21 shows the voltage versus discharge capacity curve from batteries assembled with cathode films flexographically printed with inks with and without 4 wt% dispersing agent as introduced before. The discharging curve from cathode ink with dispersing agent is much smoother than the one without dispersing agent, which implies that the ink homogeneity and film uniformity are likely be improved physically. More electrochemical characterization results will

be presented in the following chapter but from this figure, it can also be seen that the non-conductive dispersing agent has increased the internal resistance within the cell, which caused a lower discharge voltage. An optimization of the dispersing agent type and amount is highly recommended for achieving excellent ink printing quality, both physically and electrochemically.

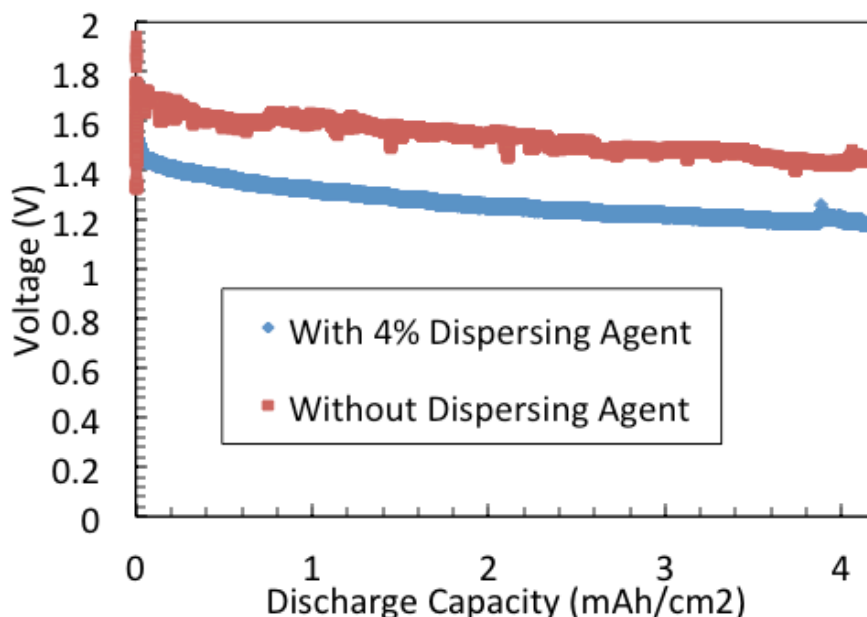


Figure 3.21. Comparison of the electrochemical performance of the cathode films printed from inks with and without 4% dispersing agent.

3.7. Physical Characterizations of the Printed Films

3.7.1. Introduction

With the different types of inks presented in the sections above, a series of printability experiments have been conducted mainly using a Perfect Proofer System (Integrity Engineering, Inc.) Figure 3.22 is shown below to just give a visual idea of what has been achieved. Figure 3.22(a) is a representative pattern printed using cathode ink formulations with CMC/SBR binders on stainless steel foils while Figure 3.22(b) is a representative pattern from using ink formulations with PSBR binders. Because of the low yield stress from the CMC/SBR based cathode inks (similar value with PVDF-HFP based cathode inks as shown in Figure 3.12), once the ink transferred to the substrate, the major part of the active powders including MnO_2 and acetylene black were easily squeezed to the edge of the pattern that was printed. Instead of forming a uniformly distributed film, this resulted in deposition of “inactive areas” in the battery electrode, which could then cause deteriorated electrochemical performance. With PSBR based inks satisfying the established yield stress and ink structural properties criteria, excellent printing quality with sharp edges and high uniformity were achieved, as shown in Figure 3.22(b).

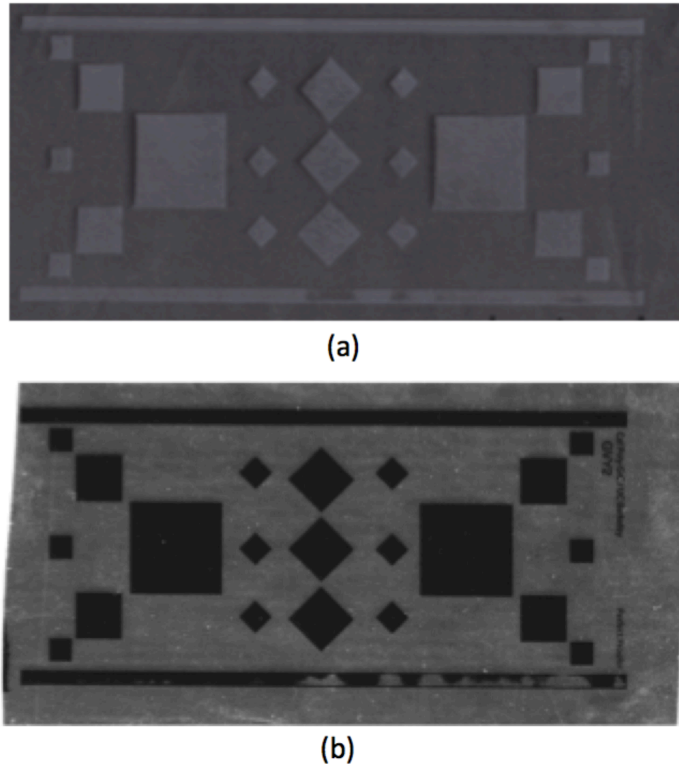


Figure 3.22. Significant improvement of printing quality on stainless steel foils by using cathode slurry inks with different polymeric binding solutions: (a) Printed films from cathode ink formulations with CMC/SBR binder; (b) Improved printed films from cathode ink formulations with PSBR binder.

3.7.2. Printed Cathode Film Surface Profile and Roughness

Films printed using the flexographic printability tester were observed under an optical microscope. Figure 3.23 below shows three representative films printed using the same PSBR-based cathode inks on stainless steel foils, but with anilox rollers with different cell volumes engraved on the ceramic surface. Larger cell volume means more ink will be transferred to the substrate, which then gives thicker deposited films. It is observed that all films printed with three available cell volumes show the well-known phenomenon of “viscous fingering” under the microscope. The fingering widths or configurations increase with the larger cell volumes. The fundamental theories of viscous fingering are still not well understood, but it is widely accepted that it is probably due to the instability during the ink transfer process, which causes ink splitting [46]-[50]. Further optimization of the ink formulations or using larger cell volumes should be able to minimize the fingering patterns. A printed film surface profile scan was done using a mechanical stylus based step profilometer (KLA-Tencor Alpha-Step IQ Surface Profiler). The anilox roller with 15 BCM cell volume helps achieve a film with an average thickness around $3.654\ \mu\text{m}$ and a standard deviation of $1.903\ \mu\text{m}$. Anilox roller with only 3.5 BCM cell volume prints a film with an average thickness around $1.271\ \mu\text{m}$ and a standard deviation of $0.681\ \mu\text{m}$.

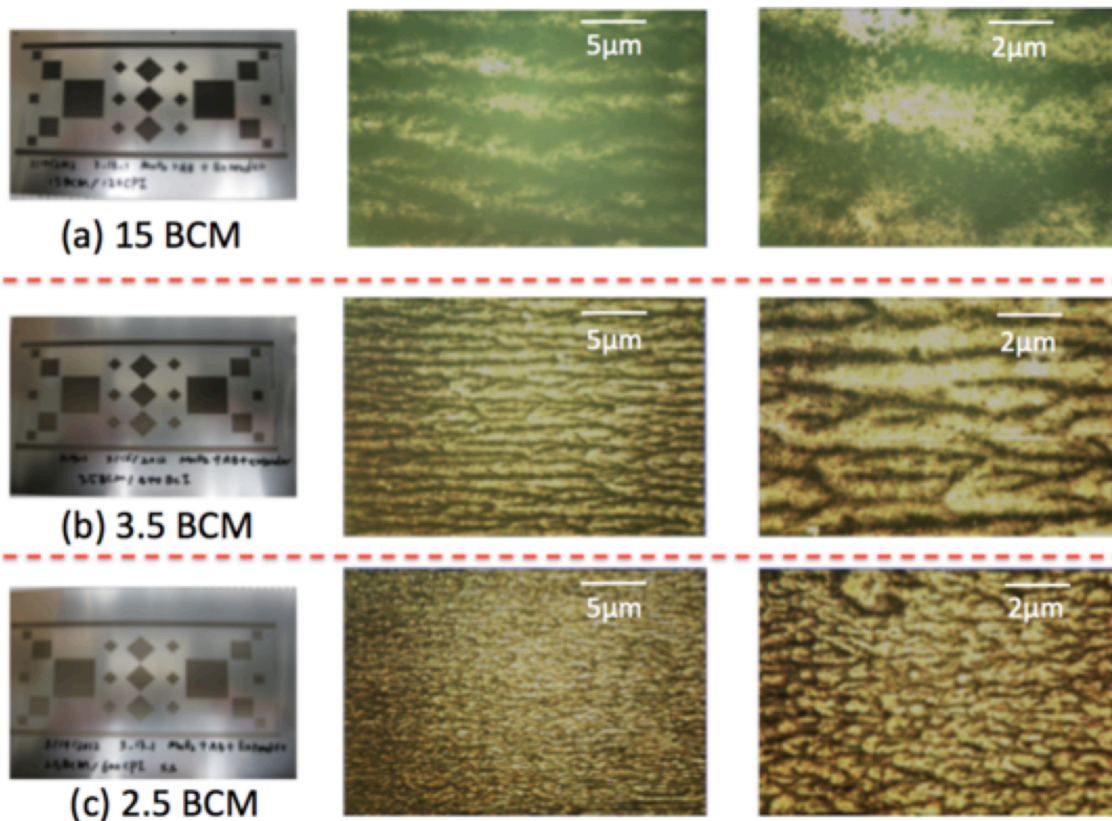
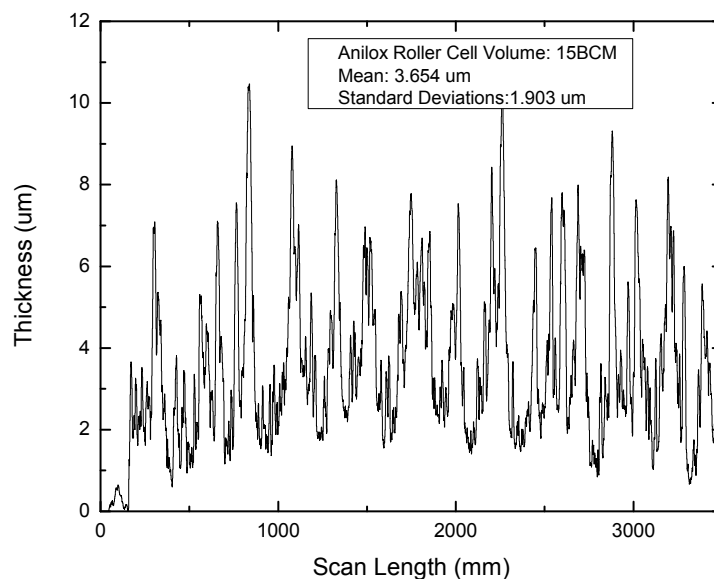


Figure 3.23. Flexographically printed PSBR-based cathode films under the optical microscope showing viscous fingering patterns: films respectively printed by using (a) 15BCM anilox roller, (b) 3.5 BCM anilox roller and (c) 2.5 BCM anilox roller.



(a)

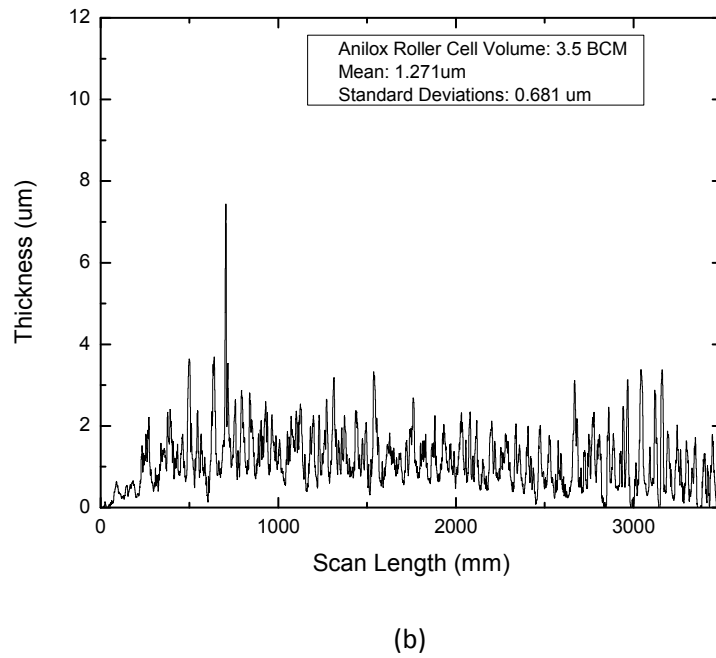


Figure 3.24. Surface profile scans of flexographically printed cathode films with: (a) 15BCM anilox roller, (b) 3.5BCM anilox roller.

For battery electrode printing applications, the thickness typically needs to be at least 20 μm to accomplish desired power and energy output per footprint area. This was realized by running multiple prints based on the same printing substrates. Figure 3.25 shows that the viscous fingering phenomenon disappeared after running five continuous prints by aligning the plates with the pattern already printed on the substrate. The cross-section of a film with five printed layers is shown in Figure 3.25, and a film thickness around 28 μm was successfully obtained.

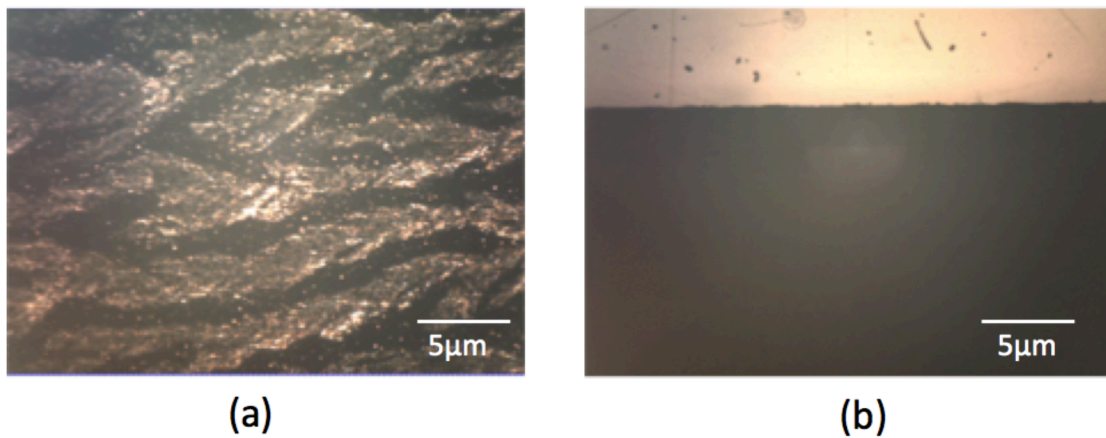


Figure 3.25. Comparison of the printed film surface profile under microscope: (a) viscous fingering patterns with just one print with PSBR-based cathode inks on stainless steel foils; (b)

No fingering patterns observed with five continuous prints with same PSBR-based cathode inks on stainless steel foils.

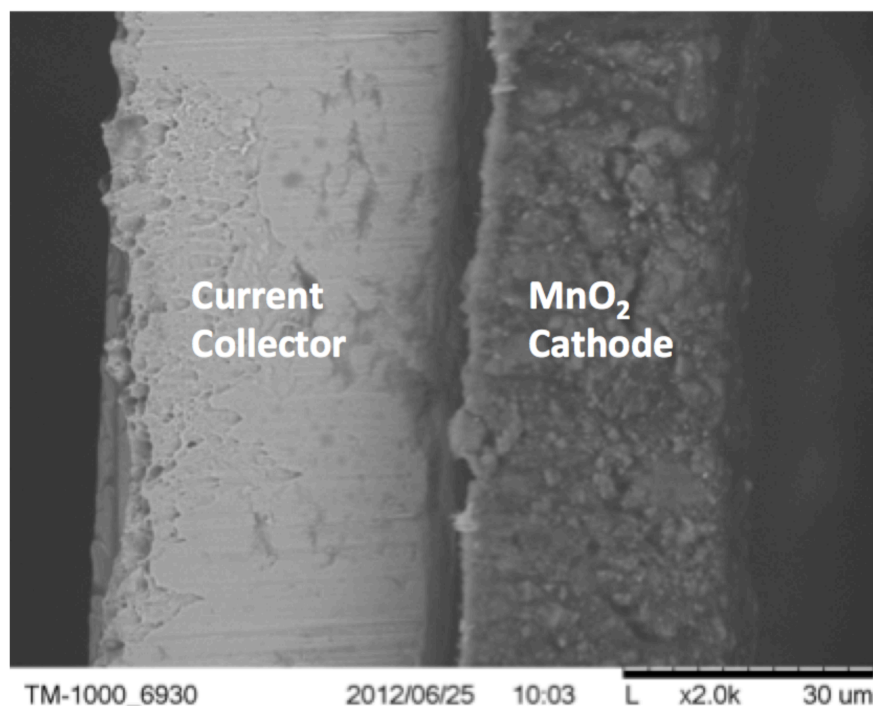


Figure 3.26. The SEM shows the cross-section of the printed PSBR-based cathode films on current collector foils.

3.8. Chapter Summary and Future Work

A roll-to-roll flexographic printing process for large-scale zinc-based battery manufacturing was proposed. Based on its fundamental operating mechanism, key criteria for developing functional flexographic printing inks were established, including composite ink rheology (steady-state viscosity and yield stress), ink wettability as well as ink dispersing qualities. The ink viscosity significantly influences the ink transfer efficiency while the yield stress critically determines its structural integrity once transferred on flexible substrate. The ink wettability indicates the ink spreading properties and film uniformity while the ink dispersing quality affects the ink homogeneity from before printing through the printing process. A variety of MnO_2 cathode inks were formulated and analyzed based on these criteria. A novel type of aqueous cathode ink based on PSBR polymeric binder showed excellent flexographic printability.

The results of this work are promising for the future development of all other composite slurry components of the zinc-based battery system for flexographic printing as will be shown in the following chapters, even including an inert particle-based ionic liquid slurry electrolyte. Future studies will address further optimization of the ink formulations to achieve better printing quality on a variety of nonconductive and conductive substrate. Specifically, the effects of polymeric binder contents as well as the type and amount of surfactant additives on the printability will be

interesting. Study on the substrate pre-treatment would be also essential to fully understanding and improvement of the whole flexographic printing process for energy storage fabrications.

Chapter References

- [1] P. K. Wright, D. A. Dornfeld, A. Chen, C. C. Ho, and J. W. Evans, "Dispenser printing for prototyping microscale devices," *Trans of NAMRI/SME*, 2010.
- [2] C. C. Ho, J. W. Evans, and P. K. Wright, "Direct write dispenser printing of zinc microbatteries," *Technical Digest of PowerMEMS*, 2009.
- [3] C. C. Ho, J. W. Evans, and P. K. Wright, "Direct write dispenser printing of a zinc microbattery with an ionic liquid gel electrolyte," *J. Micromech. Microeng.*, vol. 20, no. 10, p. 104009, Sep. 2010.
- [4] C. C. Ho, D. Steingart, J. Evans, and P. Wright, "Tailoring Electrochemical Capacitor Energy Storage Using Direct Write Dispenser Printing," presented at the 214th ECS Meeting, 2008, vol. 16, pp. 35–47.
- [5] C. C. Ho, D. A. Steingart, and J. P. Salminen, "Dispenser printed electrochemical capacitors for power management of millimeter scale lithium ion polymer microbatteries for wireless sensors," *Technical Digest of PowerMEMS*, 2006.
- [6] M. Koplow, A. Chen, D. Steingart, P. K. Wright, and J. W. Evans, "Thick film thermoelectric energy harvesting systems for biomedical applications," presented at the 2008 5th International Summer School and Symposium on Medical Devices and Biosensors, 2008, pp. 322–325.
- [7] A. Chen, D. Madan, B. T. Mahlstedt, P. K. Wright, and J. W. Evans, "Dispenser printed thick film thermoelectric materials," *Technical Digest of PowerMEMS*, 2010.
- [8] A. Chen, M. Koplow, D. Madan, P. K. Wright, and J. W. Evans, "Dispenser Printed Microscale Thermoelectric Generators for Powering Wireless Sensor Networks," 2009.
- [9] A. Chen, D. Madan, M. Koplow, and P. K. Wright, "Dispenser printed thermoelectric energy generators," *Technical Digest of PowerMEMS*, 2009.
- [10] D. Madan, A. Chen, P. K. Wright, and J. W. Evans, "Dispenser printed composite thermoelectric thick films for thermoelectric generator applications," *J. Appl. Phys.*, vol. 109, no. 3, pp. 034904–034904–6, 2011.
- [11] D. Madan, A. Chen, P. K. Wright, and J. W. J. O. A. P. Evans, "Dispenser printed composite thermoelectric thick films for thermoelectric generator applications," *J. Appl. Phys.*, vol. 109, no. 3.
- [12] D. Madan, A. Chen, P. K. Wright, and J. W. Evans, "Printed Se-Doped MA n-Type Bi₂Te₃ Thick-Film Thermoelectric Generators," *Journal of Elec Materi*, vol. 41, no. 6, pp. 1481–1486, Jan. 2012.
- [13] E. S. Leland, P. K. Wright, and R. M. White, "A MEMS AC current sensor for residential and commercial electricity end-use monitoring," *J. Micromech. Microeng.*, vol. 19, no. 9, p. 094018, Aug. 2009.
- [14] T. Mäkelä, T. Haatainen, P. Majander, and J. Ahopelto, "Continuous roll to roll nanoimprinting of inherently conducting polyaniline," *Microelectronic Engineering*, vol. 84, no. 5, pp. 877–879, May 2007.
- [15] J. Noh, D. Yeom, C. Lim, H. Cha, J. Han, J. Kim, Y. Park, V. Subramanian, and G. Cho, "Scalability of Roll-to-Roll Gravure-Printed Electrodes on Plastic Foils," *IEEE Trans. Electron. Packag. Manufact.*, vol. 33, no. 4, pp. 275–283, Oct. 2010.
- [16] M. Jung, J. Kim, J. Noh, N. Lim, C. Lim, G. Lee, J. Kim, H. Kang, K. Jung, A. D.

- Leonard, J. M. Tour, and G. Cho, "All-Printed and Roll-to-Roll-Printable 13.56-MHz-Operated 1-bit RF Tag on Plastic Foils," *Electron Devices, IEEE Transactions on*, vol. 57, no. 3, pp. 571–580, 2010.
- [17] F. C. Krebs, T. Tromholt, and M. Jørgensen, "Upscaling of polymer solar cell fabrication using full roll-to-roll processing," *Nanoscale*, vol. 2, no. 6, p. 873, 2010.
- [18] F. C. Krebs, J. Fyenbo, and M. Jørgensen, "Product integration of compact roll-to-roll processed polymer solar cell modules: methods and manufacture using flexographic printing, slot-die coating and rotary screen printing," *Journal of Materials Chemistry*, vol. 20, no. 41, pp. 8994–9001, 2010.
- [19] F. C. Krebs, "All solution roll-to-roll processed polymer solar cells free from indium-tin-oxide and vacuum coating steps," *Organic Electronics*, vol. 10, no. 5, pp. 761–768, Aug. 2009.
- [20] R. Søndergaard, M. Hösel, D. Angmo, T. T. Larsen-Olsen, and F. C. Krebs, "Roll-to-roll fabrication of polymer solar cells," *Materials Today*, vol. 15, no. 1, pp. 36–49, Jan. 2012.
- [21] L. Zhou, A. Wanga, S.-C. Wu, J. Sun, S. Park, and T. N. Jackson, "All-organic active matrix flexible display," *Appl. Phys. Lett.*, vol. 88, no. 8, p. 083502, 2006.
- [22] Lisong Zhou, Sungkyu Park, Bo Bai, Jie Sun, Sheng-Chu Wu, T. N. Jackson, S. Nelson, D. Freeman, and Yongtaek Hong, "Pentacene TFT driven AM OLED displays," *IEEE Electron Device Lett.*, vol. 26, no. 9, pp. 640–642, 2005.
- [23] G. Crawford, "Flexible Flat Panel Displays - Google Books," 2005.
- [24] K. Jain, M. Klosner, M. Zemel, and S. Raghunandan, "Flexible Electronics and Displays: High-Resolution, Roll-to-Roll, Projection Lithography and Photoablation Processing Technologies for High-Throughput Production," *Proc. IEEE*, vol. 93, no. 8, pp. 1500–1510, 2005.
- [25] A. N. Sokolov, M. E. Roberts, and Z. Bao, "Fabrication of low-cost electronic biosensors," *Materials Today*, vol. 12, no. 9, pp. 12–20, Sep. 2009.
- [26] A. C. Arias, J. Daniel, T. N. Ng, S. Garner, G. L. Whiting, L. Lavery, B. Russo, and B. Krusor, "Flexible printed sensor tape based on solution processed materials," presented at the 2010 23rd Annual Meeting of the IEEE Photonics Society (Formerly LEOS Annual Meeting), 2010, pp. 18–19.
- [27] U. Heider, R. Oesten, and M. Jungnitz, "Challenge in manufacturing electrolyte solutions for lithium and lithium ion batteries quality control and minimizing contamination level," *Journal of Power Sources*, vol. 81, pp. 119–122, Sep. 1999.
- [28] D. H. Doughty, P. C. Butler, and A. A. Akhil, "Batteries for large-scale stationary electrical energy storage," *The Electrochemical Society Interface*, Fall 2010.
- [29] D. A. Alsaied, E. Rebrosova, M. Joyce, M. Rebroso, M. Z. Atashbar, and B. Bazuin, "Gravure Printing of ITO Transparent Electrodes for Applications in Flexible Electronics," *Display Technology, Journal of*, vol. 8, no. 7, pp. 391–396, 2012.
- [30] J. J. Brezinski, "Paint and Coating Testing Manual - Google Books," *Paint and Coating*, 1995.
- [31] J.-H. Lee, U. Paik, V. A. Hackley, and Y.-M. Choi, "Effect of Carboxymethyl Cellulose on Aqueous Processing of Natural Graphite Negative Electrodes and their Electrochemical Performance for Lithium Batteries," *J. Electrochem. Soc.*, vol. 152, no. 9, p. A1763, 2005.
- [32] J. Li, R. B. Lewis, and J. R. Dahn, "Sodium Carboxymethyl Cellulose," *Electrochem.*

- Solid-State Lett.*, vol. 10, no. 2, p. A17, 2007.
- [33] H. Buqa, M. Holzapfel, F. Krumeich, C. Veit, and P. Novák, "Study of styrene butadiene rubber and sodium methyl cellulose as binder for negative electrodes in lithium-ion batteries," *Journal of Power Sources*, vol. 161, no. 1, pp. 617–622, Oct. 2006.
 - [34] J. R. Stokes and J. H. Telford, "Measuring the yield behaviour of structured fluids," *Journal of Non-Newtonian Fluid Mechanics*, vol. 124, no. 1, pp. 137–146, Dec. 2004.
 - [35] M. R. Somalu and N. P. Brandon, "Rheological Studies of Nickel/Scandia-Stabilized-Zirconia Screen Printing Inks for Solid Oxide Fuel Cell Anode Fabrication," *J. Am. Ceram. Soc.*, vol. 95, no. 4, pp. 1220–1228, Dec. 2011.
 - [36] S. Mallik, M. Schmidt, and R. Bauer, "Influence of solder paste components on rheological behaviour," *Electronics System-Integration Technology Conference, 2008. ESTC 2008. 2nd*, vol., no., pp. 1135, 1140, 1–4 Sept 2008.
 - [37] N. E. Pawlowski, L. E. Johnson, H. P. Lauw, J. P. Shields, and Z. Rehman, "Use of co-surfactants to adjust properties of ink-jet inks," 1997.
 - [38] P. J. Smith, D. Y. Shin, J. E. Stringer, B. Derby, and N. Reis, "Direct ink-jet printing and low temperature conversion of conductive silver patterns," *J Mater Sci*, vol. 41, no. 13, pp. 4153–4158, May 2006.
 - [39] P. de Gennes, "Wetting: statics and dynamics," *Rev. Mod. Phys.*, vol. 57, no. 3, pp. 827–863, Jul. 1985.
 - [40] W. D. Harkins and A. Feldman, *J. Am. Chem. Soc.*, vol. 44, no. 12, pp. 2665–2685, Dec. 1922.
 - [41] R. Defay, I. Prigogine, A. Bellemans, and D. H. Everett, "Defay, Prigogine and Bellemans Surface tension and adsorption," 1966.
 - [42] R. Weil, "Measurement of Surface Tension," *J. Appl. Phys.*, vol. 18, no. 4, p. 426, 1947.
 - [43] J. L. Ihrig and D. Y. F. Lai, "Contact angle measurement," *J. Chem. Educ.*, vol. 34, no. 4, p. 196, Apr. 1957.
 - [44] R. H. Leach, "The Printing Ink Manual - Google Books," 1993.
 - [45] I. gr, "Ink Dispersing and Pigment Stabilizations," *inkline.gr*, 03-Apr-2013. [Online]. Available: <http://www.inkline.gr/inkjet/newtech/tech/dispersion/>.
 - [46] S. M. Miller, S. M. Troian, and S. Wagner, "Direct printing of polymer microstructures on flat and spherical surfaces using a letterpress technique," *J. Vac. Sci. Technol. B*, vol. 20, no. 6, p. 2320, 2002.
 - [47] W. B. Zimmerman and G. M. Homsy, "Viscous fingering in miscible displacements: Unification of effects of viscosity contrast, anisotropic dispersion, and velocity dependence of dispersion on nonlinear finger propagation," *Phys. Fluids A*, vol. 4, no. 11, pp. 2348–2359, 1992.
 - [48] K. Reuter, H. Kempa, N. Brandt, M. Bartzsch, and A. C. Huebler, "Influence of process parameters on the electrical properties of offset printed conductive polymer layers," *Progress in Organic Coatings*, vol. 58, no. 4, pp. 312–315, Mar. 2007.
 - [49] G. Schmidt, H. Kempa, and U. Fuegmann, "Challenges and perspectives of printed electronics," *Proc. SPIE 6336, Organic Field-Effect Transistors V*, 633610, 2006.
 - [50] I. E. Dörsam, "Printing Technology for Electronics, Chapter 4 Ink transfer in the Printing Press," *idd.tu-darmstadt.de*.

Chapter 4

Electrochemical Characterizations

4.1. Introduction

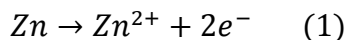
With good battery cathode films flexographically printed, electrochemical characterizations were then conducted for further optimization of the battery chemistry. A printed rechargeable zinc-based battery with an ionic liquid gel electrolyte was developed based on an assumption of a reversible intercalation mechanism of zinc ions into the manganese dioxide (MnO_2) cathode. It has been shown by Ho[1] that MnO_2 appeared to be a suitable insertion host for zinc ions, and served as a good cathode material in a zinc-metal oxide battery printed from a custom dispenser printer. However, it was pointed out at the same time that the charge transfer and transport mechanism of zinc ions in manganese dioxide cathode appears to be complicated, and further characterizations of these properties are important to the development and optimization of this specific battery chemistry[2]. Extensive characterizations of flexographically printed cathode films with newly developed aqueous-based inks are the primary focus of this chapter. Cell performance metrics include cell rechargeability and lifetime, impedance and energy density, as well as reliability, etc.

MnO_2 is a traditional, inexpensive transition metal oxide widely used in primary alkaline batteries as well as secondary Li-ion batteries, in which certain phases of the materials have been demonstrated to be able to withstand the reversible electrochemical insertion and extraction of lightweight protons and lithium ions. Synthetic MnO_2 can be categorized based on the preparation methods: chemical manganese dioxide (CMD) by chemical methods and electrolytic manganese dioxide (EMD) by electrochemical methods[3]. According to their degree of crystallization and content of foreign ions (therefore purity and stoichiometry), at least six distinct types of manganese dioxide have been characterized (α , β , γ , δ , ϵ and ramsdellite)[3]. Among them, the β - MnO_2 is the least reactive form of MnO_2 with the highest crystallinity, and it comes the closest to having a stoichiometric composition among the six [3]. By contrast, γ - MnO_2 is nearly amorphous and much more reactive electrochemically, which makes it widely used in alkaline batteries with its storage mechanism of protons (H^+). More generally, the electrochemical or battery activity of MnO_2 is determined by a combination of typical material properties such as crystal structure, surface area, porosity, and chemical purity [3].

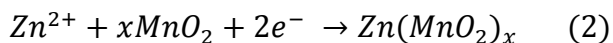
It is common that most battery chemistry performances are not readily predictable; the most reliable way of establishing their properties is through an actual performance test in a specific battery from what the author understands. In this thesis, α - MnO_2 has been mainly studied experimentally. α - MnO_2 was shown to be able to store and release much heavier zinc ions (Zn^{2+}) reversibly with large and stable tunnels in the structural framework without destruction of its fundamental structure[4]. It should be noticed that lithium ions have ionic radii of 0.68 Å and valence of one while zinc ions have ionic radii of 0.74 Å and valence of two [2][5].

The Zn/IGE/MnO₂ battery chemistry could be summarized as the following two reactions (during discharge):

Anodic reaction:



Cathodic reaction:



It can be seen that the anodic reaction is a zinc dissolution process, during discharge (and zinc deposition during charge), into the ionic liquid electrolyte. On the cathode side, it is probably a divalent zinc ion intercalation process happening. The amount of zinc ions that could be inserted and hosted in the lattice of MnO₂ will be studied in this chapter.

4.2. Experimental

The chemicals used for cathode and gel electrolyte synthesis, ink formulations and mixing methods, as well as physical characterization methods for the printed cathode films can be found in Chapter 3. Figure 4.1(a) shows the flexographically printed PSBR-based MnO₂ films with square patterns after five continuous prints on a roll of stainless steel foil, with an average thickness of 28 μm. From the SEM (Hitachi TM-1000) image in Figure 4.1(b), it was observed that the aqueous-based cathode film is denser from surface morphology than what was printed from organic solvent based cathode. It is probably because of the higher binding strength provided by the PSBR than the PVDF-HFP.

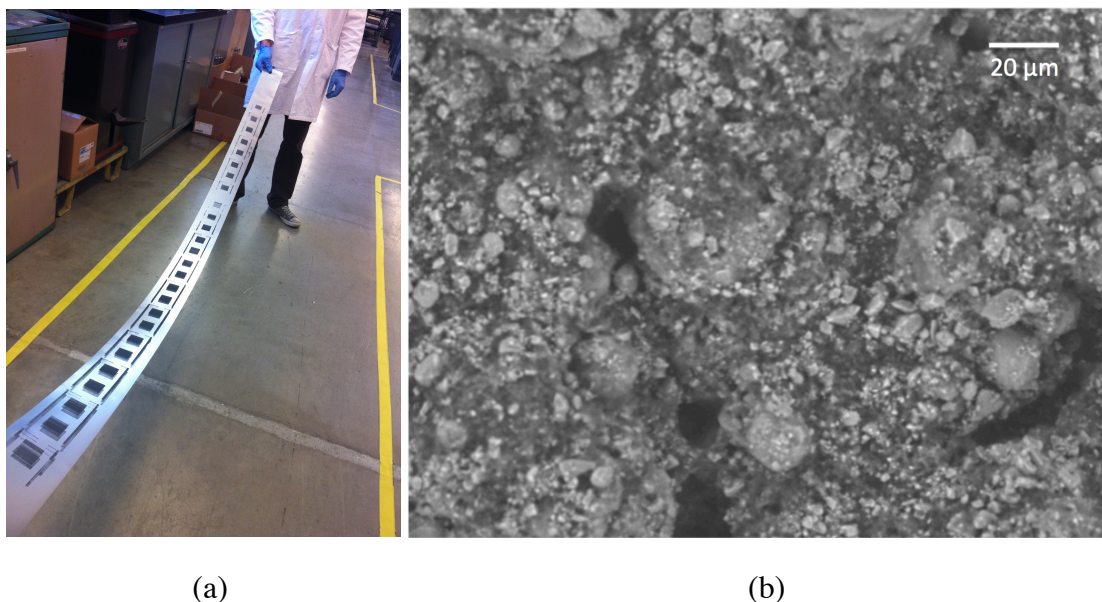


Figure 4.1. (a) Five continuous printed PSBR-based MnO₂ cathode films on a piece of stainless steel foil made with a flexographic ink printability tester at California Polytechnic State University, San Luis Obispo; (b) SEM image shows the surface profile of a PSBR-based MnO₂ cathode film.

For electrochemical characterizations, gel electrolyte solution was dispenser printed on top of the flexographically printed cathode films after being trimmed. The dispenser printed electrolyte had an active area of 1 cm² and an average thickness of 50 μm before being cured in the oven at 70 °C for two hours. Subsequently, a full cell was assembled by placing a piece of zinc foil on top (pre-cleaned with acetone) and clamping for at least 12 hours to equilibrate with the ambient environment before testing. The cell assembly process is illustrated in Figure 4.2.

All the assembled cells were tested in ambient environment at room temperature and the results were normalized according to the electrode footprint area the cell occupied. Both of cyclic voltammetry (CV) and electrochemical impedance spectroscopy (EIS) experiments were performed using a Gamry Reference 600 Potentiostat/Galvanostat/ZRA. Galvanostatic characterizations were conducted with both of the Gamry system and a custom built potentiostat/galvanostat[6].

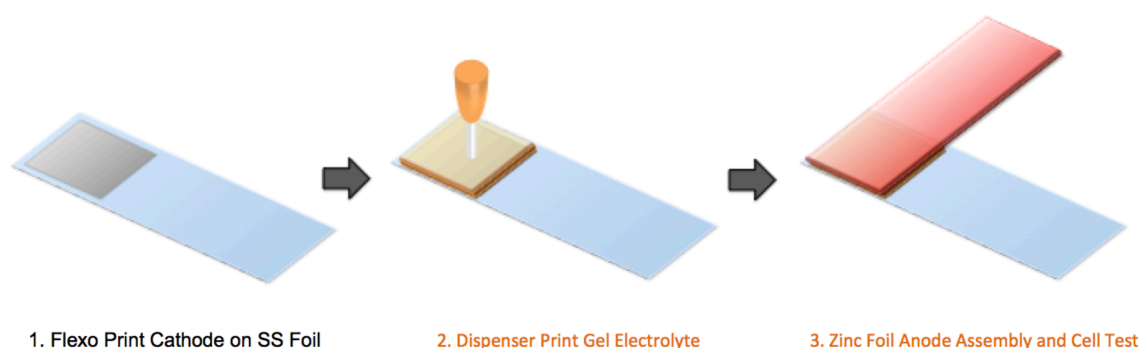


Figure 4.2. Full cell assembly process with flexographically printed cathode, dispenser printed gel electrolyte and zinc foil anode for electrochemical characterizations.

4.3. Reversible Zinc Ion Intercalation in the Flexographically Printed MnO₂ Cathode

To measure the electrochemical intercalation of zinc ions into the opened layer structure of α -MnO₂ cathode, a two-electrode cyclic voltammetry setup was used for studies of the cells assembled as described above. In these experiments, MnO₂ was the working electrode and zinc foil was used as both the reference and counter electrodes. Figure 4.3 shows a representative cyclic voltammetry plot of the insertion/extraction of Zn²⁺ ions into/from the α -MnO₂ cathode through the ionic liquid gel electrolyte at a voltage sweep rate of 10 mV/s for three continuous cycles. Relatively broad anodic and cathodic current density peaks were detected between 0.5V to 2.5V versus the Zn²⁺/Zn reference electrode, which demonstrated the fast transport of zinc ions and high interfacial reaction rate at this voltage sweep rate. The cyclic voltammetry curve indicated that the reversible electrochemical insertion and extraction of Zn²⁺ to and from the MnO₂ films occurred for at least three cycles without cell performance degradation.

Figure 4.4 shows the cyclic voltammetry curves of the flexographically printed cathode at different scan rates. Both reduction and oxidation current density peaks gradually increased with the increasing scan rate. Figure 4.5 shows a general linear relationship between the peak current density and the square root of scan rate. This linearity suggests a diffusion-limited reaction (semi-infinite diffusion)[7]. The peak current density i_p can be expressed by the classical Randles–Sevcik Equation at 25°C:

$$i_p = 2.69 \times 10^5 n^{3/2} C D^{1/2} v^{1/2} \quad (3)$$

where i_p (mA/cm^2) is the peak current density;

n is the number of electrons transferred in the reaction (2 for the zinc based chemistry);

C (mol/cm^3) is the zinc ion concentration ($2 \times 10^{-4} \text{ mol} / \text{cm}^3$);

D (cm^2/s) is the diffusion coefficient of the rate limiting species (zinc ions);

and v (V/s) is the scan rate.

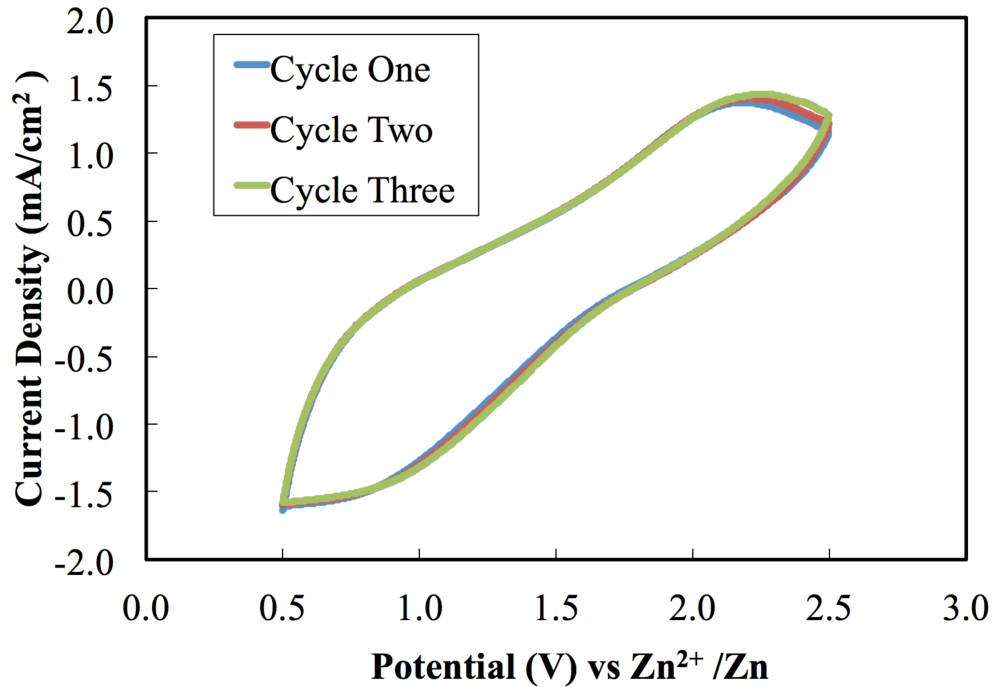


Figure 4.3. Voltammogram for a cell consisted of flexographically printed MnO_2 cathode, dispenser printed gel electrolyte, and zinc foil anode at a scan rate of 10 mV/s for three cycles. Zinc ions insertion into the MnO_2 lattice structure happened when sweeping voltage decreases while zinc ions extraction happened from the cathode structure when sweeping voltage increases. The sweeping direction started towards more positive potentials.

By fitting the slope of i_p versus $v^{1/2}$ in Figure 4.5 into Equation (3), the diffusion coefficient of zinc ions in the PSBR-based $\alpha\text{-MnO}_2$ cathode is calculated to be about $9.6 \times 10^{-9} \text{ cm}^2/\text{s}$. For comparison, the diffusion coefficient of zinc ions in BMIM+ Tf-

ionic liquid electrolytes varies as a function of zinc solute concentrations but is typically of the order of $10^{-8} \text{ cm}^2/\text{s}$ [2]. The diffusion coefficient of protons in electrolytic MnO_2 is

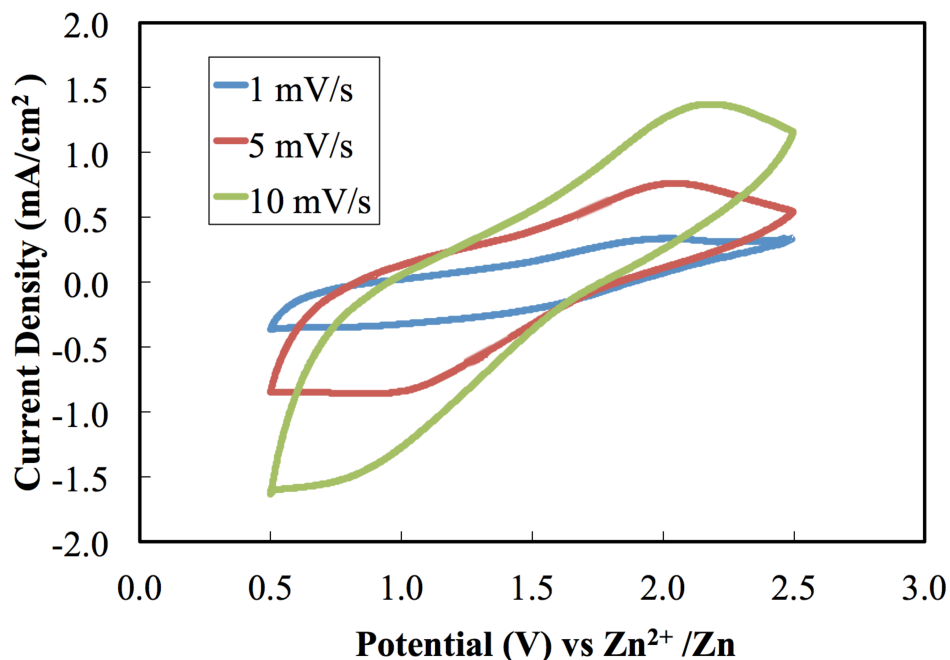


Figure 4.4. Voltammogram for an assembled cell consisting of flexographically printed MnO_2 cathode, dispenser printed gel electrolyte, and zinc foil anode at three scan rates respectively: 1 mV/s, 5 mV/s, and 10 mV/s.

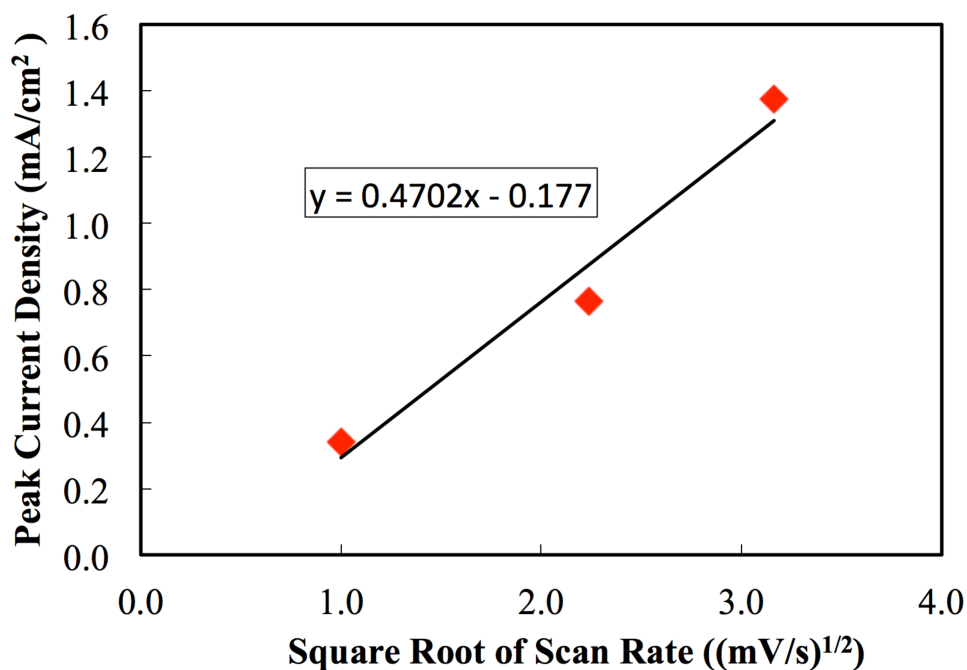


Figure 4.5. Linear relationship of the peak current density of the cell with flexographically printed cathode and the square root of scan rate during the cyclic voltammetry measurement.

10^{-15} to 10^{-16} cm^2/s [8][2] and the diffusion coefficient of lithium ions in MnO_2 is typically between 10^{-9} to 10^{-12} cm^2/s [9][2], which is similar to that of zinc ions calculated here. This indicates that although zinc ions are heavier than lithium ions, the transport properties of the two in the MnO_2 cathode are comparable and zinc ion batteries based on intercalation mechanism is a good possibility.

4.4. Galvanostatic Characterization of the Flexographically Printed MnO_2 Cathode

4.4.1. Discharge Capacity

Further electrochemical behavior of the flexographically printed cathode was measured using the galvanostatic method. The typical potential evolution of the assembled battery cell as a function of depth of discharge at a constant current density of $0.05 \text{ mA}/\text{cm}^2$ is shown in Figure 4.6. The converted galvanostatic discharge rate was about $C/3.2$ based on the maximum cell capacity obtained. The cell was discharged between 1.8 and 0.5 V. It was noticed that the discharge potential decreased with increasing depth of discharge. The sloping nature of this decline suggested that the mechanism of charge storage was predominantly pseudocapacitive[2]. It also revealed a homogeneous phase reaction nature. This specific assembled cell achieved $0.16 \text{ mAh}/\text{cm}^2$ in first cycle capacity density.

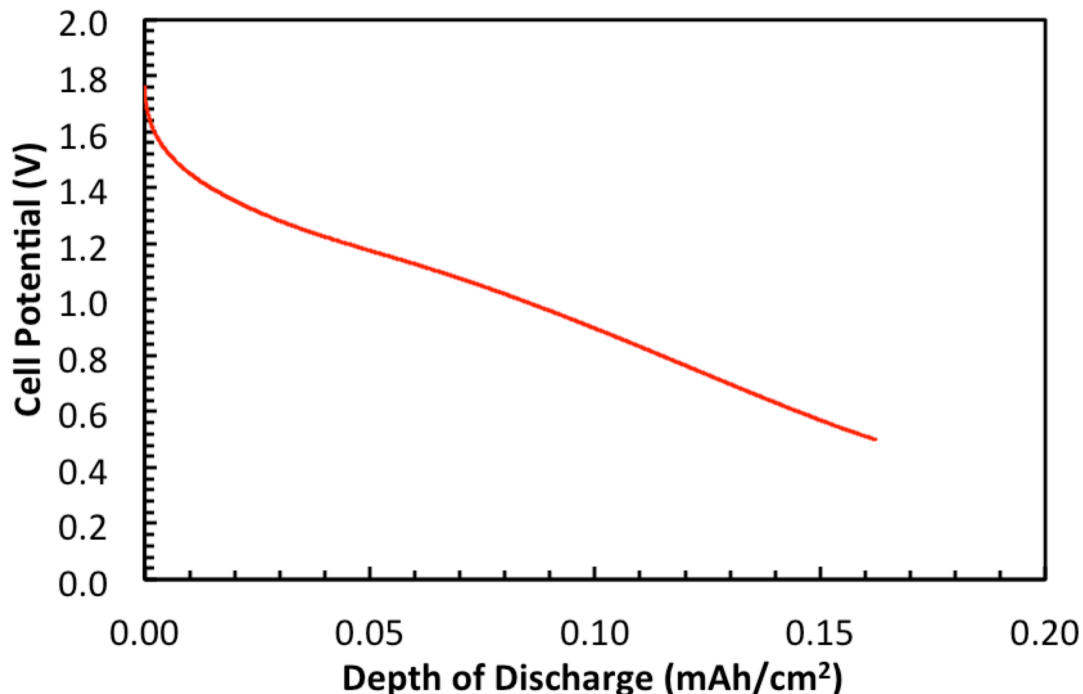


Figure 4.6. Discharge potential of a battery consisting of flexographically printed MnO_2 cathode, dispenser printed gel electrolyte, and zinc foil anode on a stainless steel

substrate, as a function of depth of discharge. The cell was discharged at a 0.05 mA/cm² current density and a C/3.2 rate.

The amount of zinc ions inserted in the MnO₂ composite cathode can be quantified using the following expression, based on the cathodic reaction written as in Equation 2:

$$x = \frac{m_{host} z_{ion} F}{M_{host} It} \quad (4)$$

where m_{host} is the total mass of the host material MnO₂;

z_{ion} is the valence of the zinc ion;

F is Faraday constant;

M_{host} is the molar mass of the host material MnO₂;

I is the current;

t is a defined amount of time the current was applied.

From the capacity measured in Figure 4.6 by discharging to a lower cutoff voltage of 0.5V, the value of x is calculated to be 20.5, which represents the amount of zinc ions inserted into MnO₂ to form Zn(MnO₂)_{20.5}, stoichiometrically. Even though this is a relatively small amount of insertion comparing to lithium metal insertion into MnO₂, it should be noticed that the value of x is inversely proportional to the cell capacity achieved. For cells with higher capacity, this level of insertion is much higher.

4.4.2. Galvanostatic Cyclability

A typical curve of assembled cell discharge capacity evolution with cycle number at a discharge current density of 0.1mA/cm² is shown in Figure 4.7. The cell was first charged at a constant current density of 0.1 mA/cm² until it reached a cutoff voltage of 1.8 V before being discharged between 1.8 and 0.5 V. As can be seen in the figure, the capacity decreased significantly at the first few cycles and then stabilized around cycle twenty. For the first twenty cycles measured, the reversible capacity was approximately 0.05 mAh/cm² while the irreversible capacity was about 0.13 mAh /cm², about 72% of the first cycle capacity. The irreversible capacity suggested that there was significant loss of active materials with first few cycles of reaction. After twenty cycles, an irreversible capacity still existed throughout each of the following consecutive cycles, but the irreversibility became negligible.

Figure 4.8 plots out the detailed cell voltage profile as a function of both the depth of charge and discharge for five different cycles. The Coulombic efficiency of the cell was calculated based on the first twenty cycles, which was about 95% at this discharge rate. This indicated that most of the charged capacity in the cells could be discharged at high efficiency.

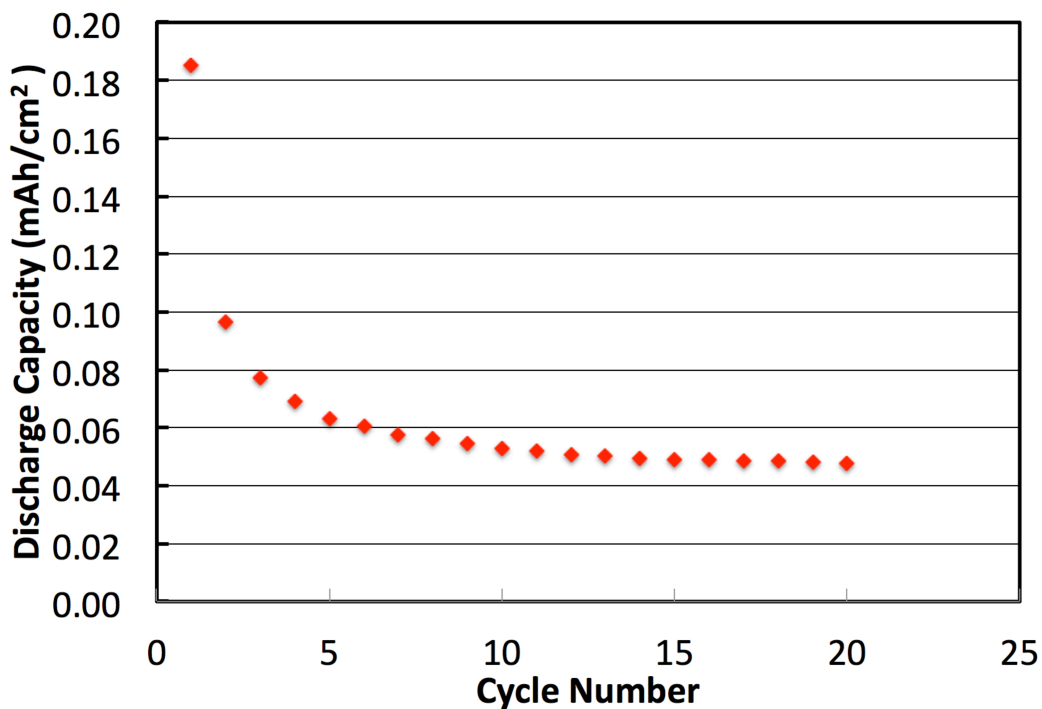


Figure 4.7. The galvanostatic cycling of a cell containing flexographically printed MnO_2 cathode, gel electrolyte, and zinc foil anode at a discharge current density of 0.1 mA/cm^2 .

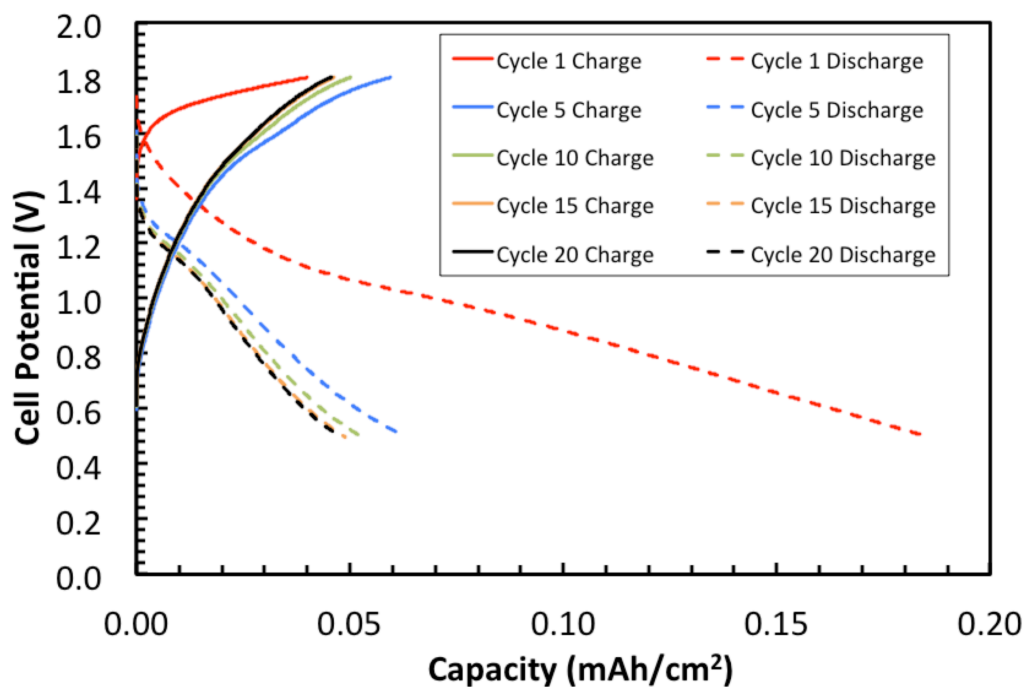


Figure 4.8. Cell potential as a function of both depth of charge and discharge for five different selected cycles. The capacity (maximum depth of discharge) drops quickly at the first few cycles but then stabilizes around cycle twenty.

4.4.3. Rate Performance

Studies on the rate performance of the assembled battery cell were also conducted and the results are shown in Figure 4.9 and Figure 4.10. Galvanostatic discharge capacities were measured between 1.8V and 0.5V for varying discharge current densities. The cells were charged and discharged using the same protocol as above but at four different current densities respectively: 0.05mA/cm², 0.1mA/cm², 0.5mA/cm² and 1.0 mA/cm². Figure 4.9 shows the cell potentials as a function of the depth of charge and discharge and Figure 4.10 summarizes the cell capacity attained at different discharge current density. As expected, the maximum discharge capacity was achieved at the lowest current density 0.05 mA/cm², which corresponded to a rate of approximately C/3.2. It is because at lower discharge current density, more active materials in the porous electrode have sufficient time to get in contact with the electrolyte penetrating into the structure, and react to generate more current over a discharge cycle. With current density increasing, the discharge capacity decreased because of the high cell impedance through the porous structure of printed cathode, which results less reactions[2].

These results indicate that the printed zinc-based battery based on this specific chemistry works better for energy-related applications in grid storage than power regulating applications. An integrated system with both of the battery and load leveling supercapacitor is widely considered to be able to address the demands for both high energy density and power density systems.

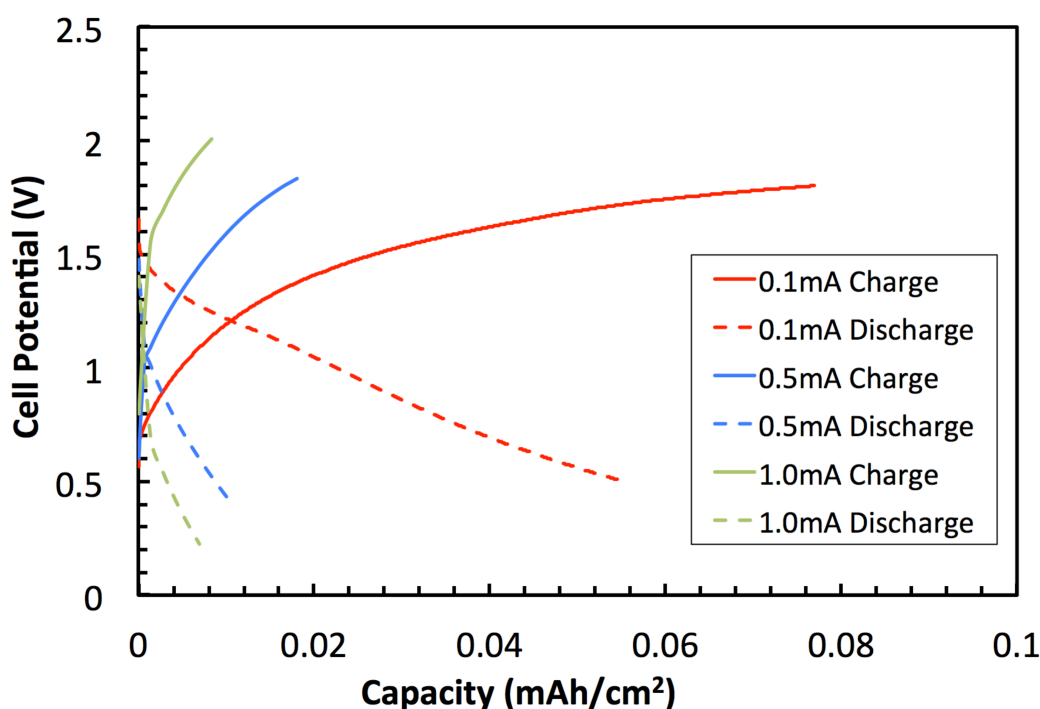


Figure 4.9. Cell potential as a function of both depth of charge and discharge at three different current densities respectively: 0.1mA/cm², 0.5mA/cm² and 1.0 mA/cm².

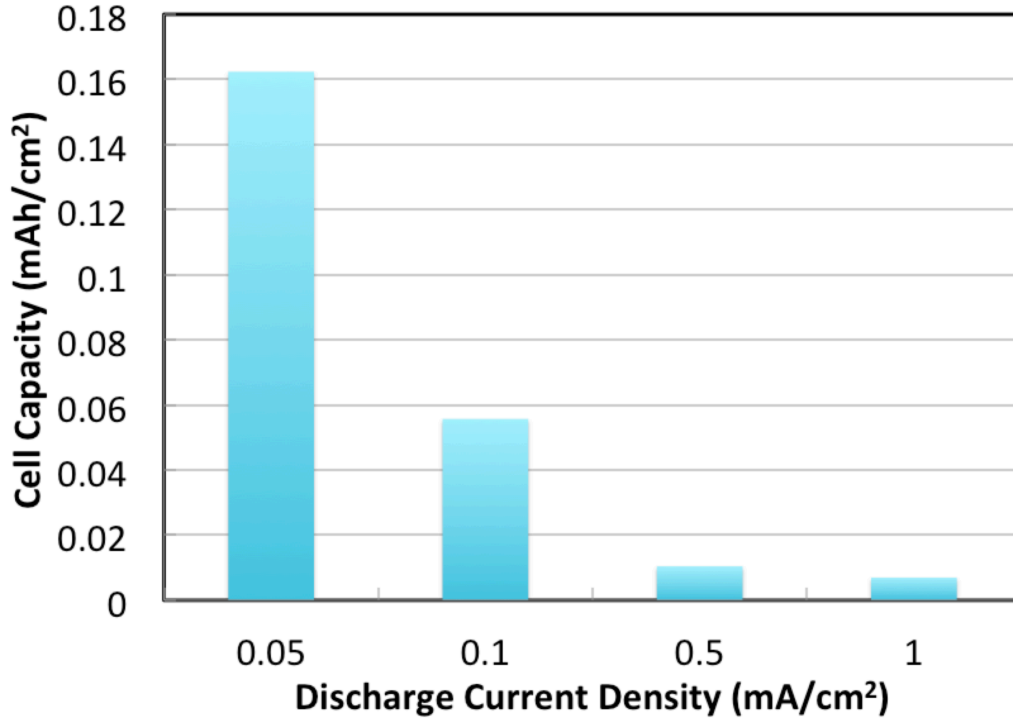


Figure 4.10. Discharge capacity extracted from the assembled cell as a function of discharge current density.

4.5. Electrochemical Impedance Spectroscopy

4.5.1. Introduction to Principles of AC Impedance Measurement

Electrochemical impedance spectroscopy (EIS) is a widely used AC impedance method to distinguish impedance components within an electrochemical cell. The impedance is measured by applying a small AC potential to the cell and recording the induced AC current response at a certain range of frequencies. The relationship between the applied potential and the response current is known as the impedance, which is similar to the potential-current-resistance relationship in a dc electrical circuit. A small sinusoidal excitation potential (amplitude of potential V_0 typically less than 10 mV) is used to maintain a linear or pseudo-linear response so that the output current remains sinusoidal in wave shape but shifted in phase[2].

The input potential, $V(t)$, is represented by the following expression:

$$V(t) = V_0 * \cos(\omega t) = V_0 * \cos(2\pi f t) \quad (5)$$

where

t is the time;

V_0 is the amplitude of the potential;

ω is the radial frequency;

and f is the frequency.

The output current response also has a sinusoidal shape, which is expressed as:

$$I(t) = I_0 * \cos(\omega t - \phi) = I_0 * \cos(2\pi f t - \phi) \quad (6)$$

where

I_0 is the amplitude of the current;

ϕ is the phase shift.

Based on Euler's Formula:

$$e^{j\theta} = \cos\theta + j\sin\theta \quad (7)$$

$V(t)$ and $I(t)$ can therefore be expressed using complex notations:

$$V(t) = V_0 * e^{j\omega t} \quad (8)$$

$$I(t) = I_0 * e^{j\omega t - j\phi} \quad (9)$$

The impedance is the ratio between the input potential and the output current, expressed below as a function of phase angle instead of time:

$$Z = \frac{V(t)}{I(t)} = |Z| * e^{j\phi} = |Z| * (\cos\phi + j\sin\phi) \quad (10)$$

where

$|Z|$ is the modulus of impedance.

Based on the above Equation 10, there are therefore two types of plot to represent the measured "electrochemical impedance spectrum". The first type is a widely used "Nyquist plot", representing impedance Z in a complex plane because the impedance can be divided into real and imaginary components and visually represented in a Nyquist plot. The second type is a "Bode plot", in which the impedance modulus $|Z|$ and phase angle ϕ are plotted as a function of measuring frequency f on horizontal axis.

Most electrochemical impedance spectra can be fitted to equivalent circuit models incorporating various circuit components that represent physical entities in the electrochemical system. Overviews of the common equivalent circuit elements and their physical meanings in electrochemical systems can be found in several publications ([2], [10], and [11]). A summary of the common circuit elements and their mathematical expressions in impedance used to model electrochemical systems is given in Table 4.1.

4.5.2. Interfacial Properties between Zinc and Gel Electrolyte

An example of both of the Nyquist plot and Bode plot displaying the impedance spectra for a symmetric electrochemical cell with two zinc foil electrodes and an ionic liquid gel electrolyte is shown in Figure 4.11 and 4.12. This cell was built to study the ionic liquid

gel electrolyte resistance as well as interfacial properties between the zinc electrode and the gel electrolyte.

A planar cell structure was first built by clamping two zinc foil electrodes on both sides of the same gel electrolyte as described in the experimental section. The active interfacial area between the electrodes and the electrolyte was 1 cm^2 . The cell was again allowed to stabilize over 12 hours after assembly before an EIS test was performed on the cell at room temperature in ambient environment. The cell was swept with a V_0 of 5 mV from 1 MHz to 0.01 Hz with 0V DC bias.

Table 4.1. Common equivalent circuit elements in electrochemical systems and their mathematical expressions in impedance (adapted from [2]).

Equivalent Circuit Element	Impedance Expression
Resistor, R	$Z=R$
Capacitor, C	$Z=1/j\omega C$
Constant Phase Element, CPE	$Z=A(j\omega)^{-\alpha}$
Infinite Warburg, W_{infinite}	$Z=W(\omega)^{-1/2}(1-j)$
Bounded Warburg, W_{finite}	$Z=W(\omega)^{-1/2}(1-j)\tanh[\delta(j\omega/D)^{1/2}]$

An equivalent circuit model was built to model this system by Ho and is illustrated in Figure 4.12[2]. The system can be expressed as an equivalent circuit containing a gel electrolyte resistor in series with a constant phase element that is in parallel with an interfacial charge transfer resistor and a Warburg diffusion element. The constant phase element corresponded to a complex double layer capacitance in a cell system, representing non-uniform interfacial properties between porous electrodes and electrolyte [2]. For this specific gel electrolyte based test cell, this element was used because of the interfacial inhomogeneity from the non-standard cell assembly process. The Warburg diffusion element is commonly used to model semi-infinite linear diffusion and was included in the circuit to represent the diffusion of zinc ions in the gel electrolyte. The equivalent circuit model works well for assembled cells with dispenser printed electrolyte and zinc foil electrode. The fits determined by the equivalent circuit model are also included in both of Figure 4.11(a) and 4.11(b). From the equivalent circuit model, the gel resistance of this system is $90.17 \text{ } \Omega/\text{cm}^2$, and the interfacial resistance is $57.49 \text{ k}\Omega/\text{cm}^2$.

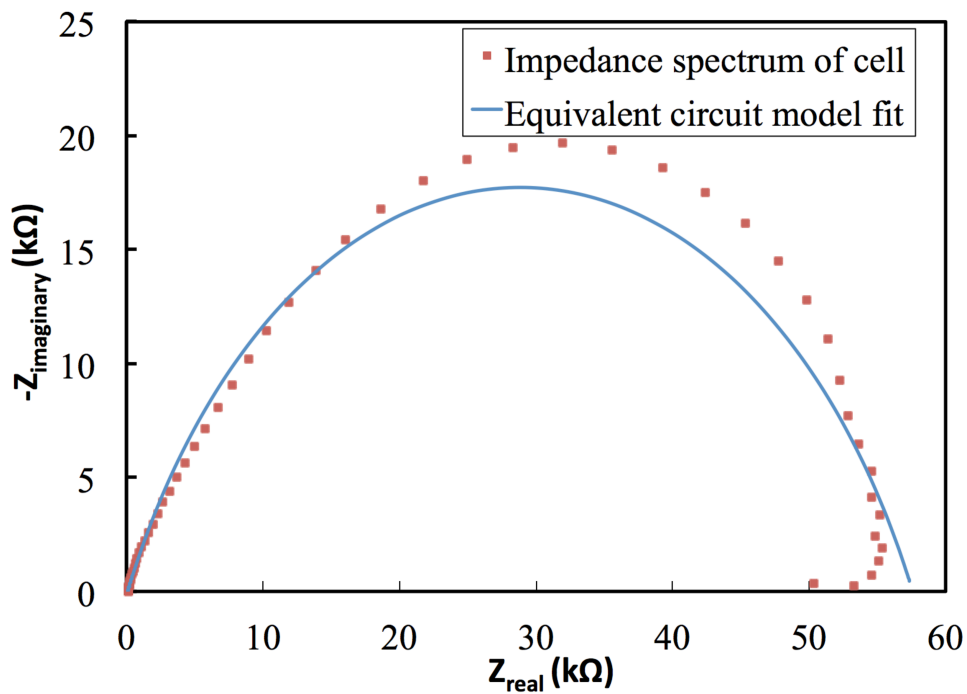


Figure 4.11(a). AC electrochemical impedance spectra in Nyquist form and equivalent circuit fitting of one zinc/gel/zinc cell containing two zinc foil electrodes and one ionic liquid gel electrolyte.

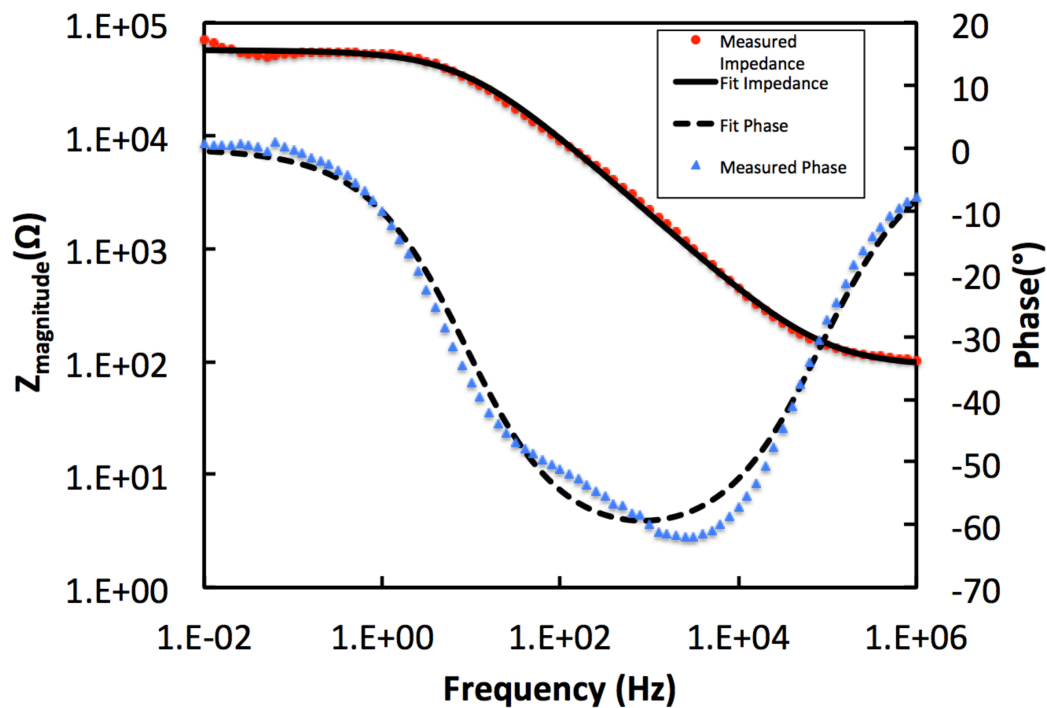


Figure 4.11(b). The electrochemical impedance spectra in Bode form and equivalent circuit fitting of one cell containing two zinc foil electrodes and one ionic liquid gel electrolyte.

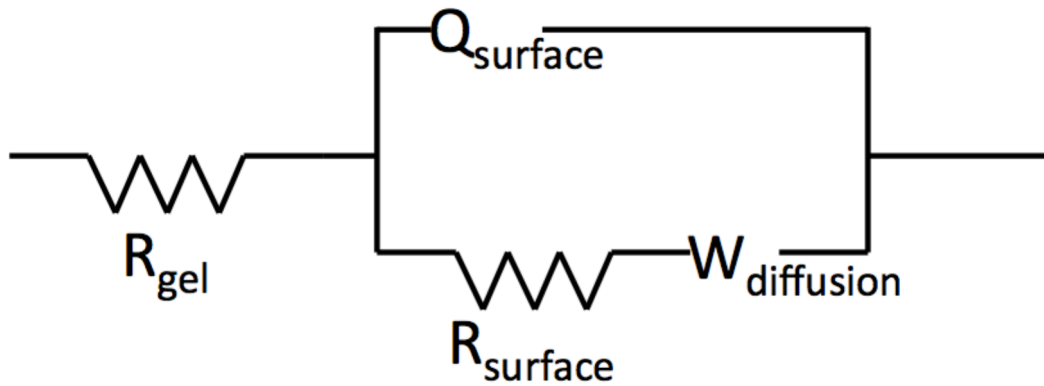


Figure 4.12. Equivalent circuit model built for a test cell containing two zinc foil electrodes and one ionic liquid gel electrolyte. R_{gel} represents the resistor, $Q_{diffusion}$ represents the constant phase element and $W_{diffusion}$ represents the Warburg diffusion element (adapted from [2]).

Using the same ionic liquid electrolyte, symmetric cell structure and testing method, studies on the cell impedance variation as a function of working temperature and dispenser printed gel electrolyte thickness were conducted. The temperature dependence results of the cell impedance are shown in Figure 4.13 together with the extracted gel resistances and the interfacial resistances from the equivalent circuit models built above. It was observed that both the gel and the interfacial resistances decreased as the cell working temperature increased. These were attributed to the increasing ionic conductivities through the gel electrolyte and the decreasing interfacial charge transfer resistances with the temperature.

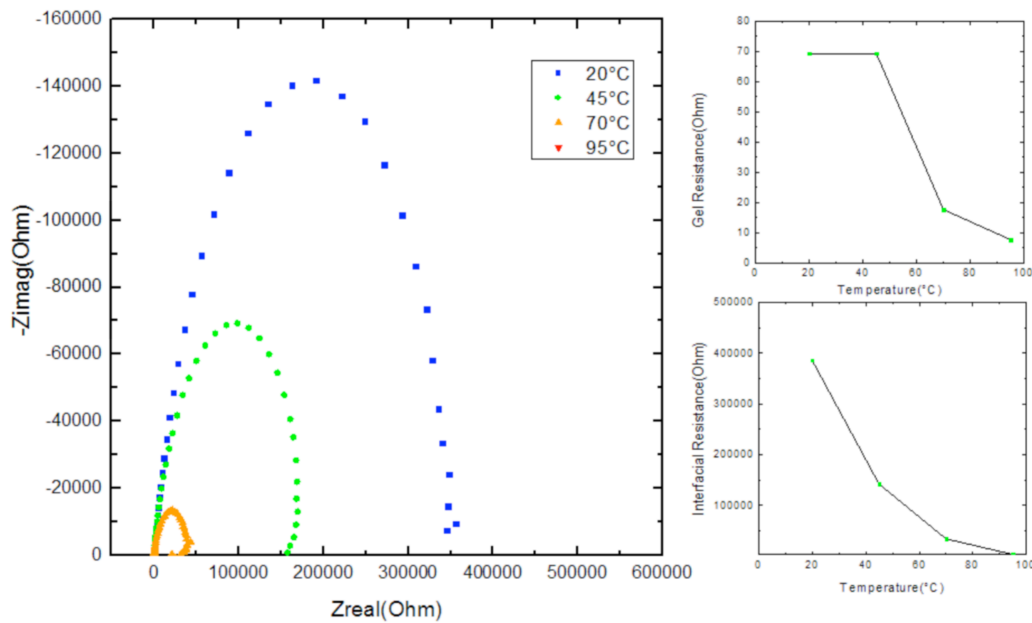


Figure 4.13. Electrochemical impedance spectra in Nyquist form of a zinc/gel/zinc cell measured at four different temperatures respectively: 20°C, 45°C, 70°C, and 95°C. The cell contained a gel electrolyte sandwiched between two zinc foil electrodes. The decreases in the size of the loops can be attributed to decreasing interfacial impedances with temperature increases. Both of the gel resistance and interfacial resistance decrease with the increasing temperature.

The ionic conductivity σ of the electrolyte was calculated based on the following equation:

$$\sigma = l/AR_{gel} \quad (11)$$

where

l is the gel electrolyte membrane thickness;

A is the active area of the gel electrolyte;

and R_{gel} is the gel resistance measured from impedance spectra.

The ionic conductivities calculated in the wide temperature range from 20 °C to 95 °C were all in the order of magnitude of 10^{-3} S/cm, which are comparable to those of typical lithium ion conducting polymer gel electrolytes. This impedance result of ionic liquid gel electrolyte shows the promise for potential battery applications in wide operating temperature ranges.

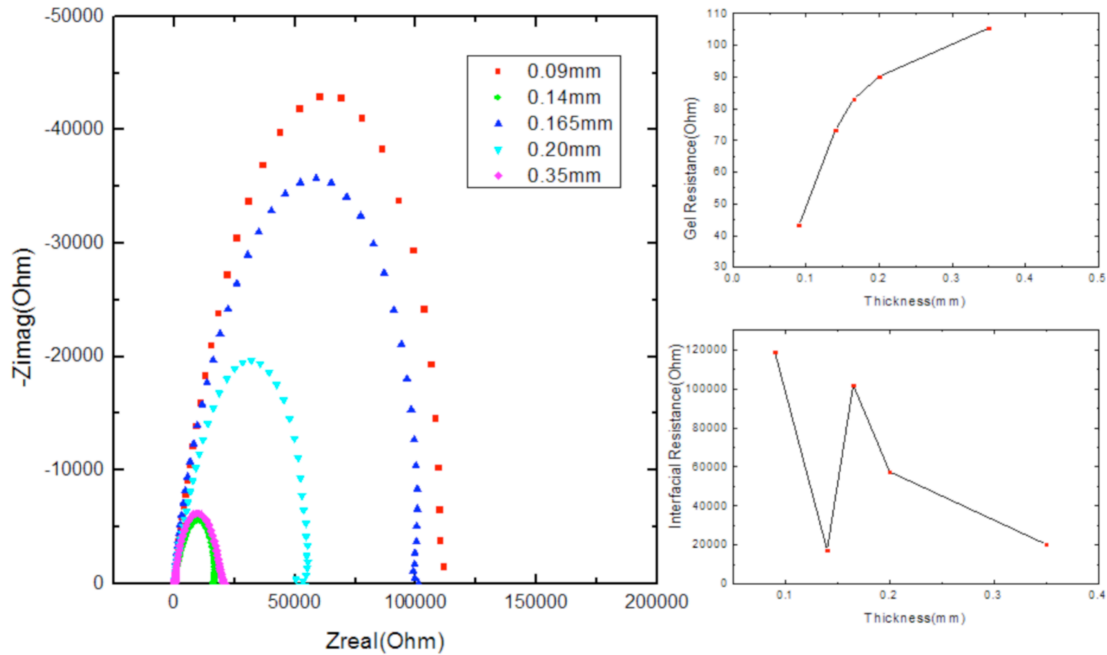


Figure 4.14. Electrochemical impedance spectra in Nyquist form of five zinc/gel/zinc cells consisting of gel electrolyte films at different thickness. The cell contained a gel electrolyte sandwiched between two zinc foil electrodes. The gel resistances increase

with the increasing thickness while the interfacial resistances show no apparent dependence on the gel thickness.

The electrolyte impedance dependence on the gel membrane thickness is shown in Figure 4.14. As expected according to Equation 11, the gel resistance increased with the membrane thickness. The interfacial resistance did not show direct relationship with the thickness. The fluctuation of the interfacial resistance curve was probably due to the varying forces applied to cells during the assembly process with different clamps. The process variables contributing to the low cell yield and performance variation will be discussed in session 4.6.

The dependence of ionic conductivities on the zinc solute concentrations in the BMIM+Tf⁻ ionic liquid electrolyte as well as on the ionic liquid concentrations in the PVDF-HFP binding solution were studied by Ho[2]. It was concluded that the ionic conductivities increase with lower zinc solute concentration in the BMIM+Tf⁻ ionic liquid but with higher ionic liquid electrolyte concentration in the PVDF-HFP gel. However, as the ionic liquid electrolyte concentration increases in the gel, “sweating” happens as shown in Figure 4.15, which causes the mechanical strength of the gel structure to degrade. There should be a tradeoff between gel electrochemical performance and structural integrity.

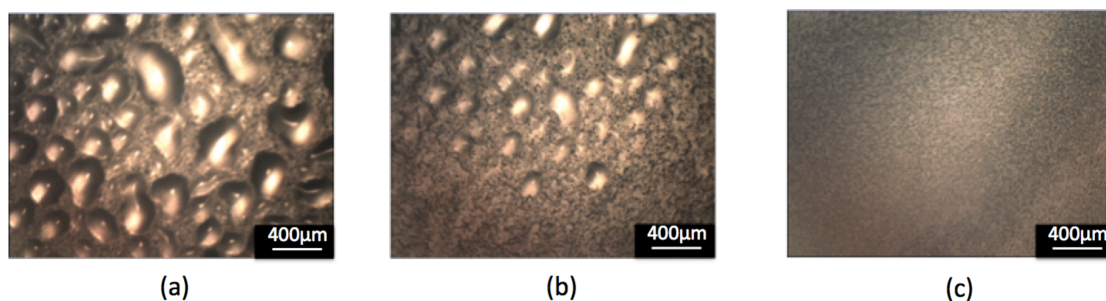


Figure 4.15. Gel electrolytes under optical microscope after being taken out of the oven for two hours, respectively for three gel electrolytes with different weight ratios of ionic liquid electrolyte to PVDF-HFP: (a) 1:1; (b) 0.75:1; (c) 0.5:1. Electrolyte “sweating” happened to the gel electrolyte with more than 50 wt% 0.25M ionic liquid electrolytes in PVDF-HFP.

4.5.3. Impedance Analysis of The Assembled Full Cell

The influence of the cell potential on the electrochemical behavior of zinc ions in the flexographically printed α -MnO₂ composite electrode was also investigated using electrochemical impedance spectroscopy. For a small AC input signal with an amplitude V_0 of 5 mV and a frequency sweep between 0.1 Hz to 10⁶ Hz, the impedance spectra of an assembled cell containing a flexographically printed MnO₂ cathode, a dispenser printed gel electrolyte, and a zinc foil anode were recorded along one discharge and charge cycle at several potentials with 0V DC bias. From the CV curves shown before,

when the potential decreased, the cathode started transferring from zinc ion extraction to the zinc ion insertion.

The cell's impedance spectra from the discharge routine were recorded from 1.49 to 1.11 V versus Zn^{2+}/Zn reference electrode, which are all displayed in Figure 4.16. An equivalent circuit model was not successfully built for these measurements probably because the cell systems are highly complex and constantly changing. But it was suggested by Ho that there are four main phenomena contributing to the cell's overall polarization[2]: the gel electrolyte resistance at very high frequencies, the electrode surface film resistance, the charge transfer resistance at the electrode and electrolyte interface, and diffusion effects at very low frequencies(not apparent in the plots here at frequencies above 0.1Hz).

The frequencies in the plots decrease from left towards the right direction. It was observed that the spectra taken for the cell at 1.11 V and 1.32V replicate the high frequency behavior of the 1.49 V scan; but in the lower frequency charge transfer region, curve divergences occur. The smaller semi-circles at low potentials show increased charge transfer resistance at the interface with potential increasing. This is backed by the impedance spectra at two charging process potentials as shown in Figure 4.17. With increasing cell potential from 1.21 to 1.36 V, the charge transfer semicircle stretches and expands as a function of working potential with the same trend as the discharge process. Similar results were observed with dispenser printed cells an equivalent circuit model was successfully built by Ho [2].

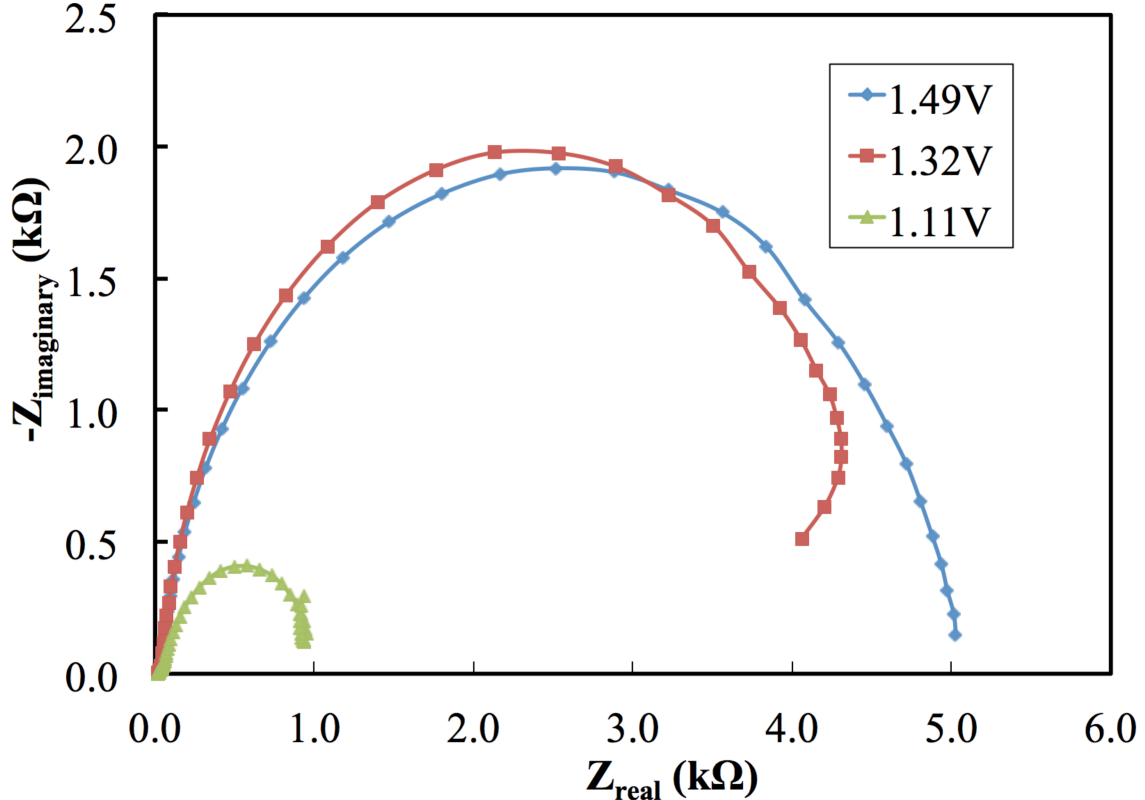


Figure 4.16. Electrochemical impedance spectra at several discharging cell potentials, respectively at 1.49 V, 1.32V and 1.11V. The assembled cell that was measured contained a flexographically printed MnO₂ cathode, a dispenser printed gel electrolyte, and a zinc foil anode.

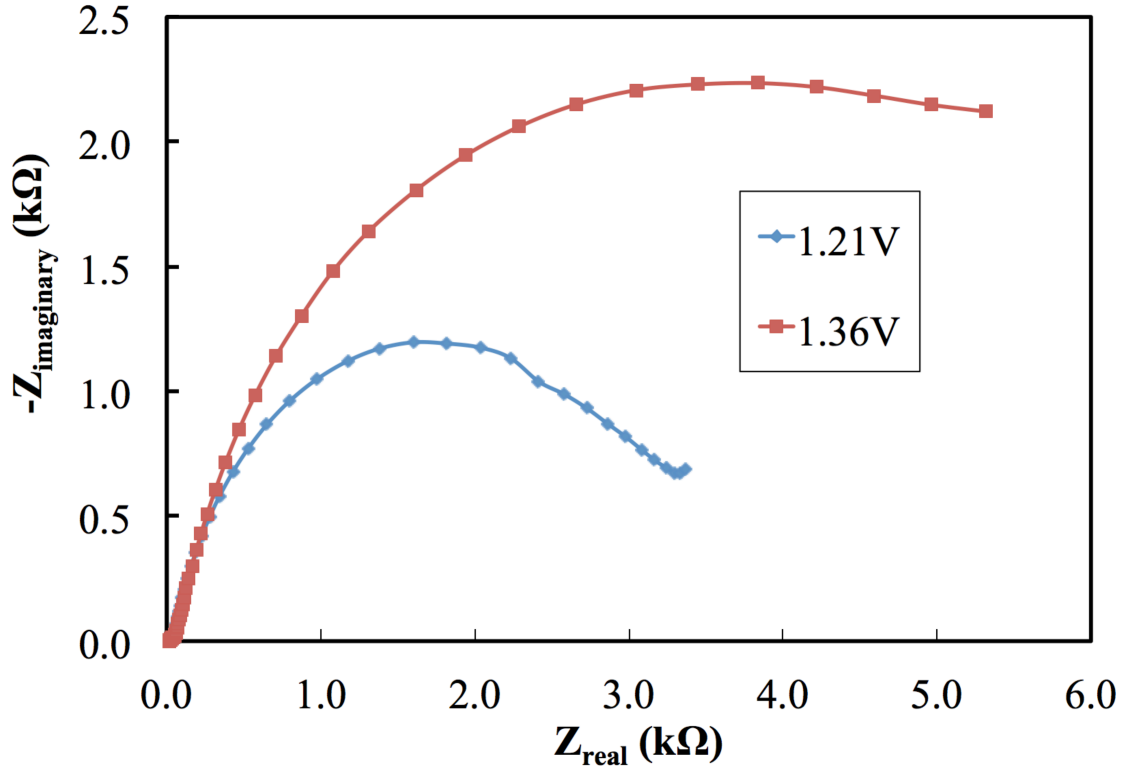


Figure 4.17. Electrochemical impedance spectra at several charging cell potentials, respectively 1.21 V, and 1.36V. The assembled cell that was measured contained a flexographically printed MnO₂ cathode, a dispenser printed gel electrolyte, and a zinc foil anode.

4.6. Zinc-based Battery Characterization in Controlled Environment

4.6.1. Introduction to Low Cell Yield and Performance Variations

Even though both of dispenser and flexographically printed zinc-based batteries showed promising results in aspects of achievable energy density and cycle life, the current printed battery cells suffered from low cell yield and performance variations. Batteries printed in the same batch frequently exhibited distinct electrochemical behavior. While a few cells achieved tens of cycles without capacity degradation, most of the cells displayed severe capacity fade or even failed within just a few cycles[2]. Figure 4.18

shows a cyclic voltammetry curve for a clamped cell consisted of a printed MnO₂ cathode, a gel electrolyte and a zinc foil electrode. The rough and changed scanning curves for three continuous cycles show that the uneven interfacial properties between the electrode and electrolyte for the assembled cell could be one of the process variables resulting in the performance variations for different printed cells.

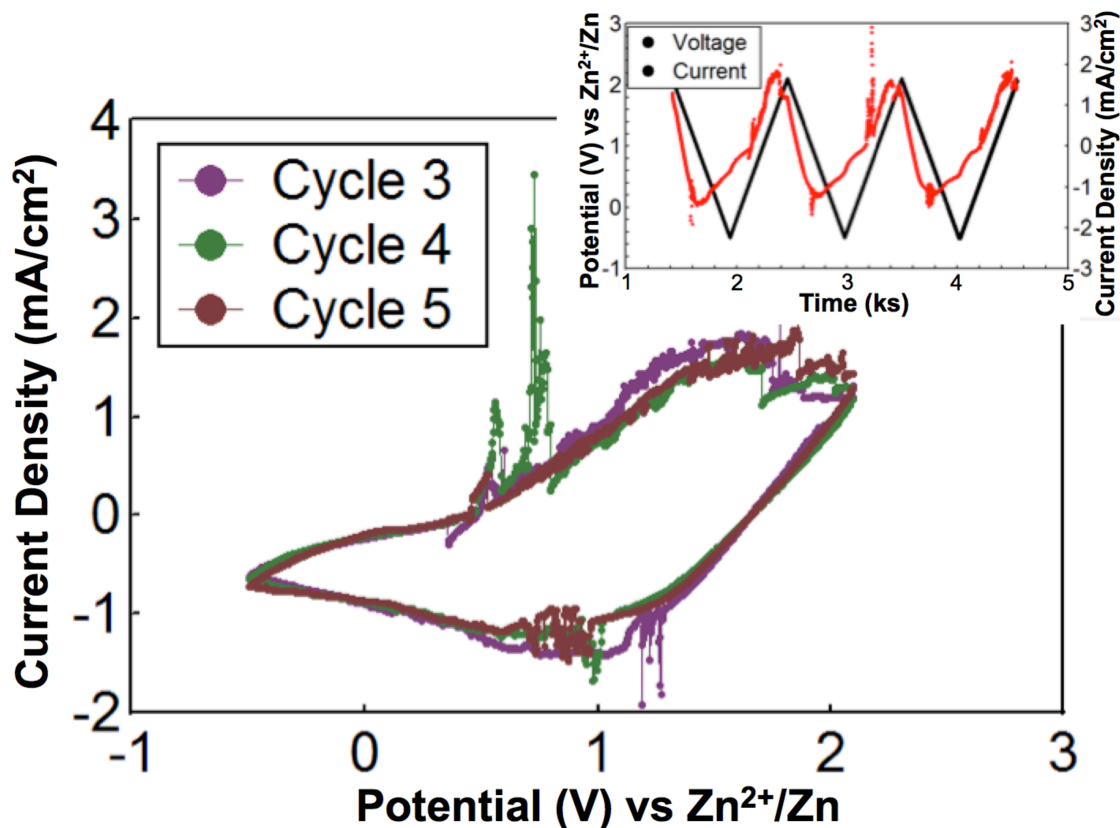


Figure 4.18. Cyclic Voltammogram for a cell consisted of printed MnO₂ cathode, gel electrolyte, and zinc foil anode at a scan rate of 10 mV/s for three cycles. The applied cyclic sweeping voltage and measured current as a function of time is shown in the upper right corner of the graph.

Table 4.2. Summary of variables potentially contributing to the low yield and performance variation for the assembled cells with flexographically printed MnO₂ cathode, respectively, from functional ink development process, printing process and cell assembly and characterization process.

Functional Ink Development	Flexo Printing	Post-printing
Powder Size and Distribution	Inter-roller Pressure	Cell Assembly
Powder Oxidation	Substrate Uniformity and Tension	Testing Method
Ink Mixing Method	Anilox Roller	Testing Environments
Dispersion and Stabilization	Plate Accuracy	
Rheology	Printing Speed	
Wettability	Drying Temperature and Time	

A summary of potential variables contributing to the cell performance variation is shown in Table 4.2. The variables are divided into three primary categories: pre-printing process (functional ink preparation), printing process, and post-printing process (assembly and characterizations). Because all the experiments through the three processes were performed in ambient environmental conditions, there was a poor control with experimental process parameters such as humidity and oxygen level. Therefore it was difficult to determine which variable is having most effect on the cell performance. Preliminary experiments making standard coin cells using the same zinc-based chemistry for printable batteries in controlled inert environments have consequently been conducted.

4.6.2. Experimental for Making Coin Cells

The chemicals used for MnO_2 cathode, ink formulations and mixing methods were the same as used for flexographic printing. After the PSBR-based slurry ink was prepared in the ambient environment, an automatic coating machine with doctor blade was employed to cast the electrode on a stainless steel or aluminum foil. Punching tools were used for making circular disk cathodes with a 1.27 cm diameter, after the electrode was air dried for 24 hours. Then the circular disk electrodes prepared were put in the vacuum oven for 12 hours at 130°C before being transported directly into an argon-filled glove box without exposure to the air.

The zinc salt and ionic liquid solution were dried in the vacuum oven for 6 hours at 90°C before being transported into the glove box. Ionic liquid electrolyte solution with the same formulation as described before (1:10 zinc salt to ionic liquid mass ratio) was then prepared in the glove box and ready for coin cell assembly.

Punching tools were used for making circular disk anodes with a 1.43 cm diameter from the zinc foil. All the circular disk anodes prepared were dried in the vacuum oven for 12 hours at 130°C before being transported directly into an argon-filled glove box.

All other components used for the coin cell assembly were dried in vacuum oven for 12 hours at 130°C before being transported directly into an argon-filled glove box, including the top and bottom cases, Celgard@separator and spacer, as well as springs. A coin cell press was then used for making coin cells in the argon-filled glove box.

The coin cells were then transported out to the lab environment for testing, using a fully automated Maccor battery controller unit.

4.6.3. Discharge Capacity and Rate Performance

Figure 4.19 shows the first cycle deep discharge voltage profiles, between 1.7V and 0.1V, for coin cells made in the argon environment. With discharge current density increasing, the specific discharge capacity in mAh per gram of active material MnO_2 decreased. The capacity achieved at 11.2mA/g specific discharge current was comparable to what was attained from the assembled cell in ambient environment with flexographically printed cathode. In Figure 4.20, the capacity versus cycle curves were plotted at three

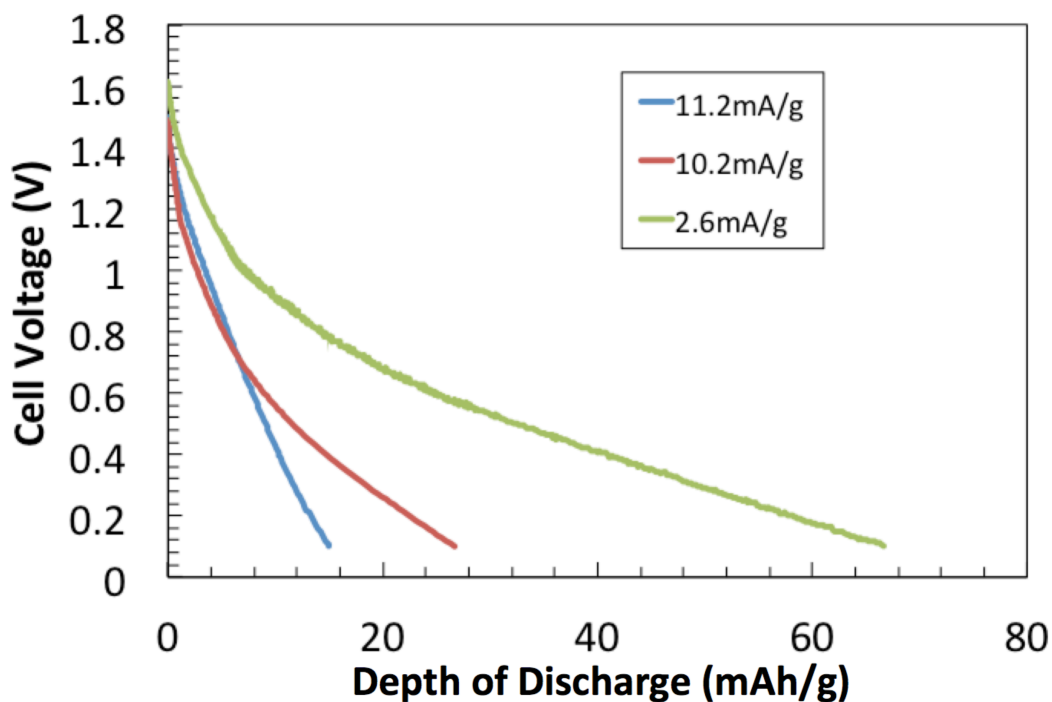


Figure 4.19. First cycle cell voltage versus discharge capacity for coin cells made in Argon-filled glove box at three different discharge current densities.

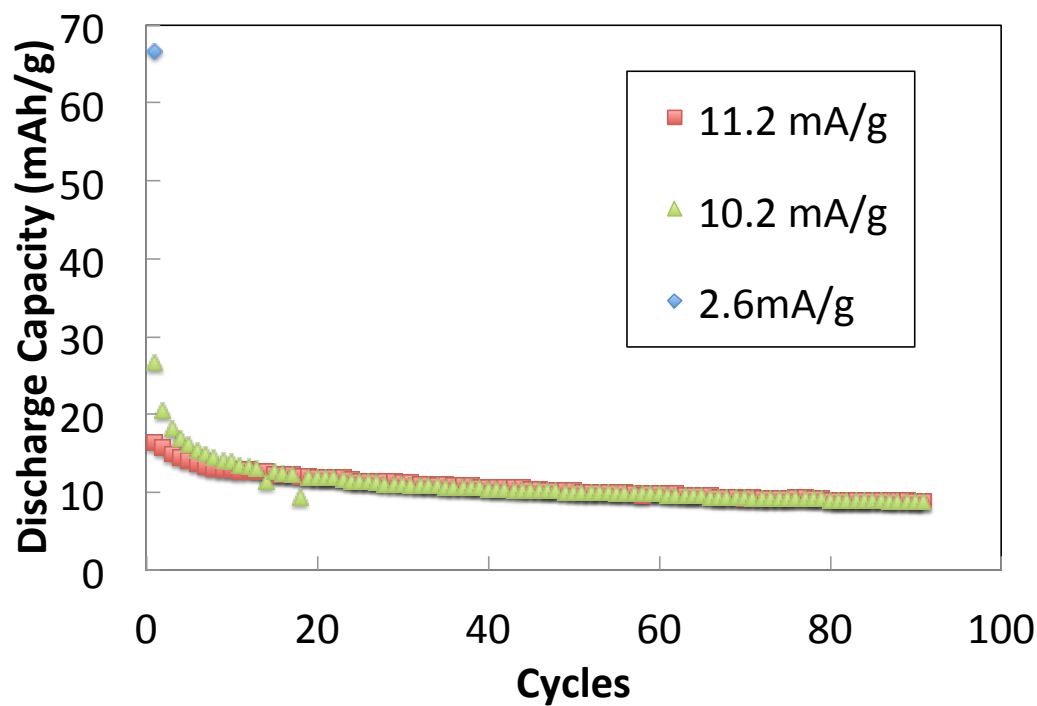


Figure 4.20. The galvanostatic cycling of a coin cell containing PSBR-based MnO_2 cathode, ionic liquid electrolyte, and zinc foil anode at three different discharge current densities.

discharge current densities. There were fast capacity decreases up to 64% over the first twenty cycles and then the capacities slowly stabilized. The behaviors are similar to what was obtained in most cells assembled in ambient environment, but the results were more consistent and repeatable.

4.6.4. Water Influence on the Coin Cell Performance

The influence of water content in the cell on the performance was studied by making coin cells in the glove box with the same MnO_2 cathode coated with doctor blade but without going through the vacuum oven drying process. The circular disk cathodes were transported directly in the glove box after they were air dried at room temperature in ambient environment overnight. A considerable amount of water was expected to remain in the cathode. The galvanostatic cycling curves of this experiment are shown in Figure 4.21. It was noticed that the coin cells made with "wet" cathodes did not show much difference with regard to specific capacity over cycles, although starting out at a lower capacity. Further experiment with more accurate measurement and control of water content in the cathode as well as the ionic liquid electrolyte will be helpful to understand the influence of water content on the zinc-based battery chemistry performance.

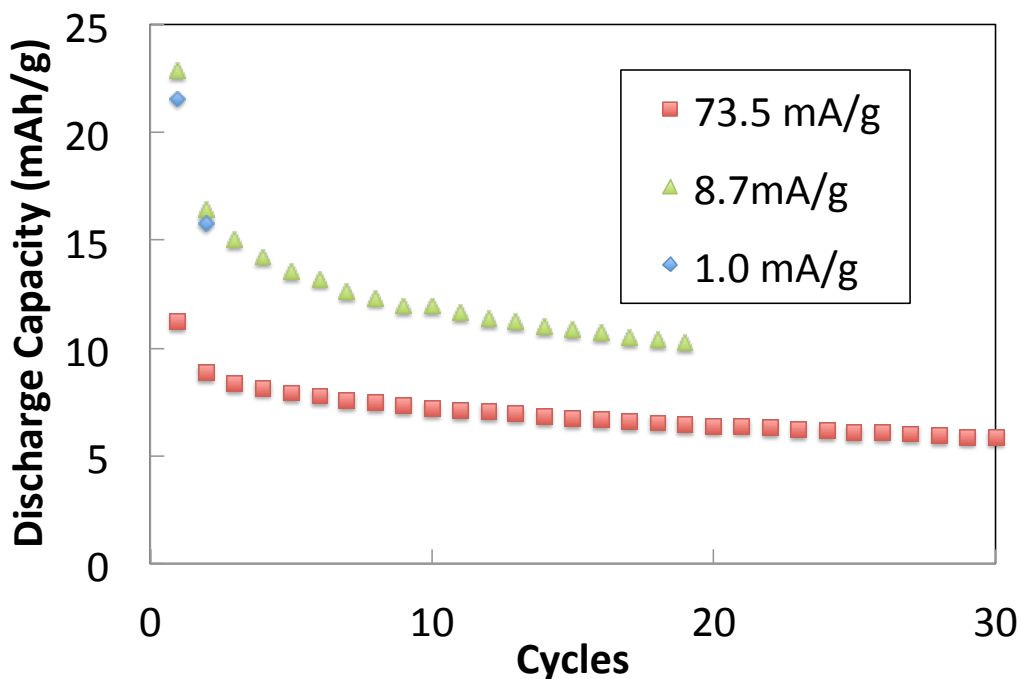


Figure 4.21. The galvanostatic cycling of a coin cell containing PSBR-based MnO_2 cathode (dried only at room temperature overnight in ambient environment), ionic liquid electrolyte, and zinc foil anode at three different discharge current densities.

4.6.5. Current Collector Effect

Aluminum foils, which is easy to process, corrosion resistant to an oxidizing potential and inexpensive, are widely used as the current collector for the cathode in lithium ion battery systems[12]. A comparison of the zinc-based coin cell capacity performances at similar discharge current density made using aluminum foil and traditional stainless steel foil is shown in Figure 4.21. Both cells achieved similar electrochemical performance. It was concluded that aluminum foils are compatible with the printable PSBR-based MnO_2 cathode and therefore could potentially be used to replace stainless steel foils in suitable applications for the zinc-based chemistry.

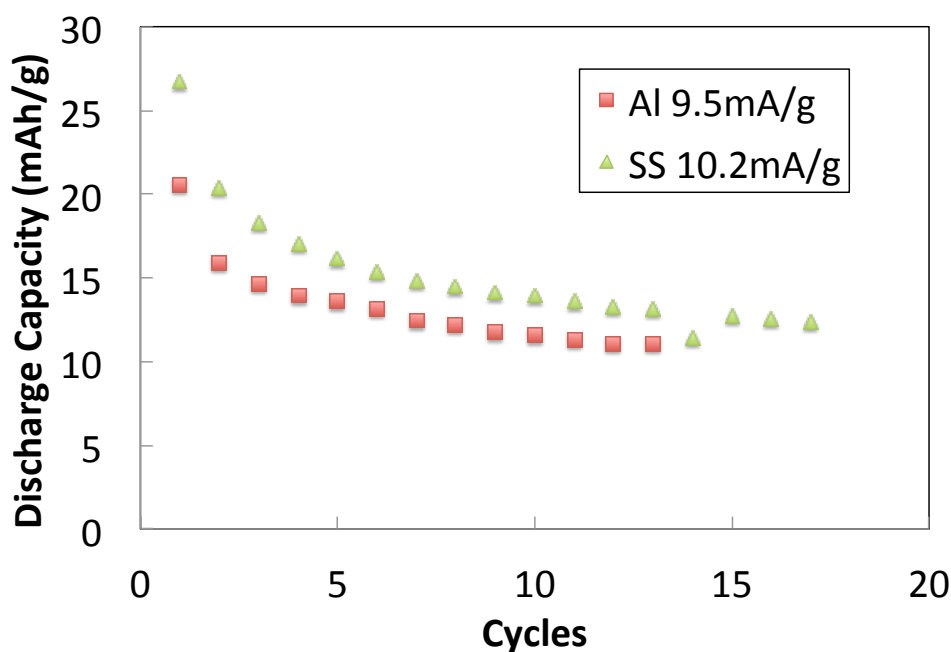


Figure 4.21. Comparison of the coin cell cycling performances with different current collectors at similar discharge current density: aluminum and stainless steel foils.

4.7. Printable Current Collectors

4.7.1. Entirely Printed Zinc-based Battery

Previous research on the printable zinc-based battery was mainly focused on the optimization of the two electrodes as well as the ionic liquid electrolyte and the fabrication on foil current collectors[13]-[15]. Development of printable current collectors will open more opportunities for direct energy storage device integration on any non-conductive substrates used in various industrial and residential applications. Combining with the roll-to-roll printing technique, large-scale electrochemical energy storage could be fabricated on various flexible substrates, such as plastics and papers used in packaging industry.

This session shows the preliminary efforts towards development of an entirely printable battery. Figure 4.22(b) shows the cross-section of a five-layer battery, entirely printed using the custom dispenser printer on a polyimide substrate, under the SEM. The five layers include: the zinc anode, the MnO_2 cathode, the ionic liquid gel electrolyte and two nickel composite current collectors. For comparison, a printed cell with only two electrodes and one gel electrolyte is shown in Figure 4.22(a)[1].

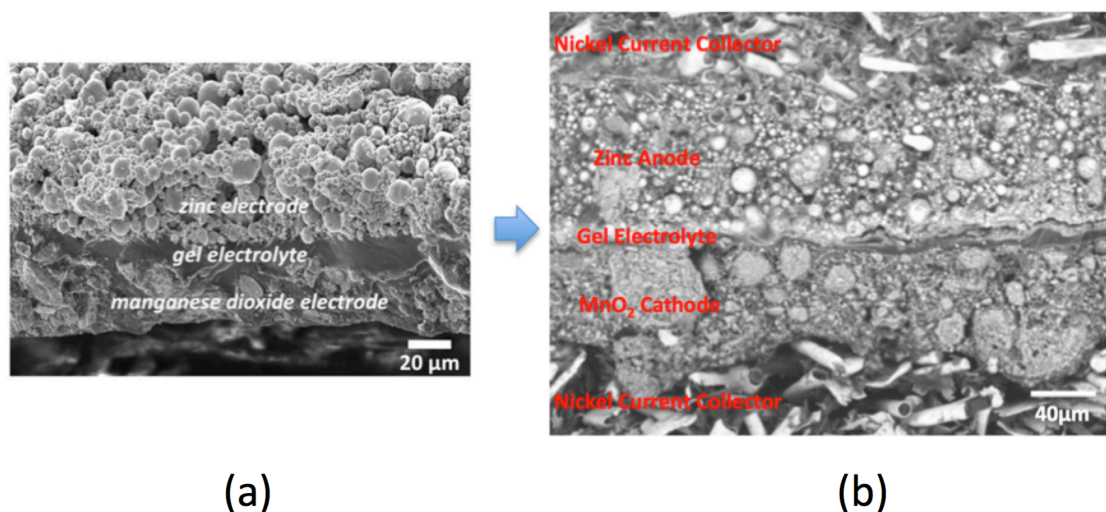


Figure 4.22. (a) Cross-section of a dispenser printed zinc-based battery under SEM showing the sandwich structure with three layers: zinc anode, gel electrolyte and MnO_2 cathode[1]; (b) Cross-section of a dispenser printed battery under SEM with additional two current collector layers, on the top and at the bottom. The current collectors were composed of carbon black fibers coated with nickel and PSBR binder.

Figure 4.23 shows two entirely dispenser printed zinc-based solid-state batteries on two non-conductive substrates, one on a polyimide and the other on a transparent plastic material. Both of the current collectors were designed with electrical connection patterns, so they were conveniently connected to external loads for testing and characterizations. The printed cells showed open circuit voltages around 1.2V but during the galvanostatic cycling, the battery showed no useful discharge capacity. The close circuit voltages dropped abruptly to the controlled cutoff voltage when discharges started, which were probably due to the high internal resistances caused by the printed current collectors. In the following session, an initial optimization of the printable nickel current collector for higher conductivity will be discussed.

4.7.2. Optimization of the Printable Nickel Composite Ink

Composite current collector inks have been developed using PSBR as the binder material. All inks were mixed using a planetary mixer (Torrey Hills ND 0.4L) for three hours

before being printed to form square films on glass slides with an area of 1 cm^2 . Electrical conductivity measurements of the printed nickel films were carried out using the Van der Pauw method to determine the sheet resistance of the materials. In Figure 4.24, it is shown that printed nickel films with inks containing 80 wt% original pure nickel powder ordered from Sigma-Aldrich and 20 wt% PSBR achieved the highest conductivity. Composite nickel inks with nickel-coated carbon black powder did not give good film conductivities.

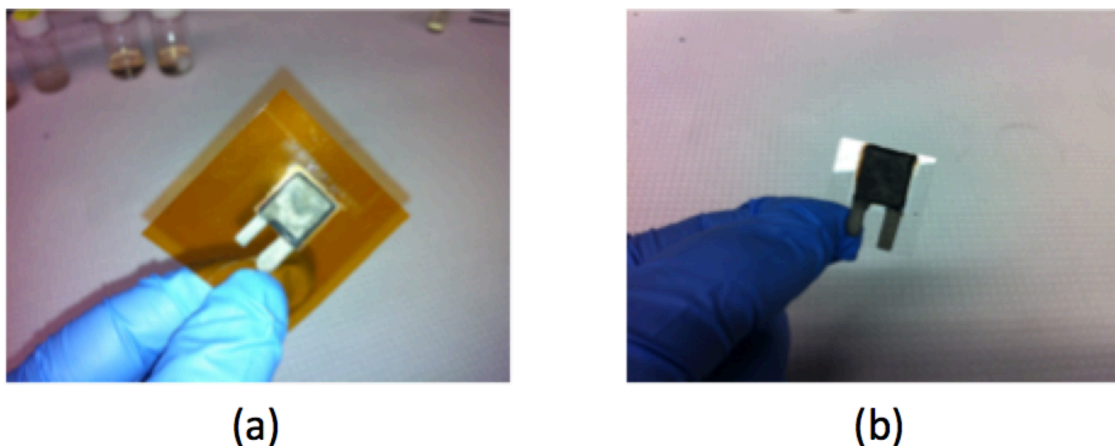


Figure 4.23. (a) Dispenser printed zinc-based battery on a flexible polyimide substrate; the two current collectors were designed with electrical connection patterns; (b) Dispenser printed zinc-based battery on a transparent plastic substrate.

Ball-milling the original pure nickel powder was then used to further control the powder size and distribution. All powders were individually placed into 100ml stainless steel jars with stainless steel balls with different diameters at a ball-to-powder mass ratio of 10:1. The jars were then placed in a planetary ball mill (Torrey Hills ND 0.4L) and operated at rotational a speed of 300 rpm for a certain amount of time. Isopropanol (ordered from Sigma Aldrich, Inc.) was typically used as a process control agent at a 1:1 weight ratio of powder to fluid[16], [17]. As shown in Figure 4.25, the powders showed distinct shapes and sizes after being ball-milled using different size stainless steel balls as well as for different time durations. Most powders transformed into flake shape after being ball-milled for six hours with stainless steel balls with both sizes.

Composite current collector inks consisted of both the original nickel powder and the PSBR binder were ball milled using the same method as above. SEM images of the printed film surface morphologies are shown in Figure 4.26. Films printed with the nickel ink, which was ball-milled for six hours with 3mm stainless steel balls, showed almost no binder materials dispersing through the film. The conductivity measurements in Figure 4 confirmed that ball-milling process seems to have an adverse affect on the nickel conductivity. The electrical conductivity of composite nickel films printed from ink with six hours of ball milling is lower than from ink with two hours of ball milling.

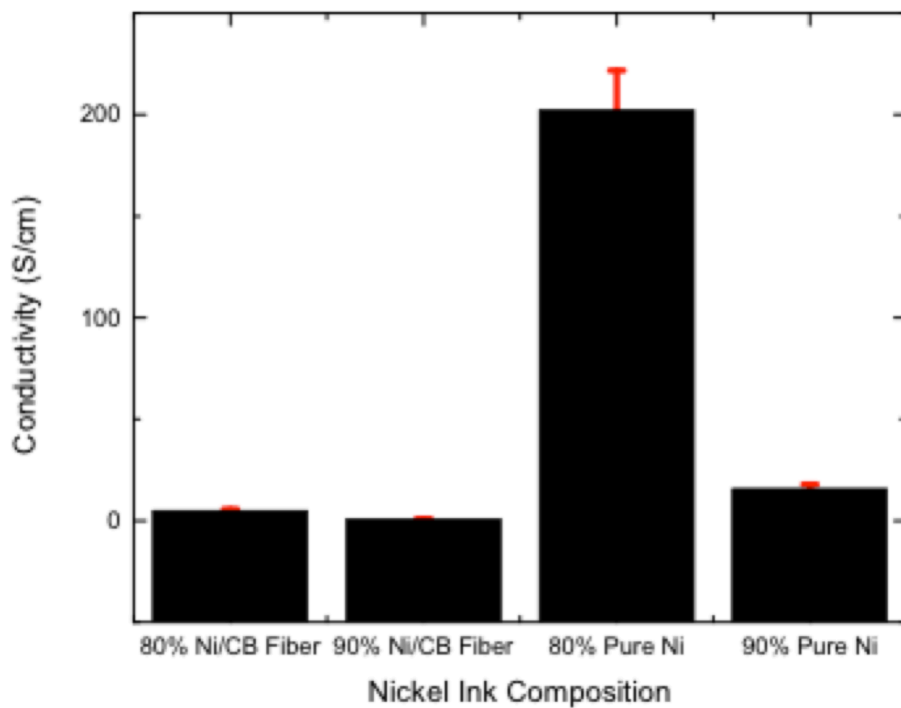


Figure 4.24. Conductivity measurements for films dispenser printed from four PSBR-based nickel current collector inks. PSBR was used as the binder for all four inks. Ni/CB Fiber represents nickel coated carbon black fibers. Pure nickel powders were obtained from Sigma-Aldrich (coauthored with Bernard Kim).

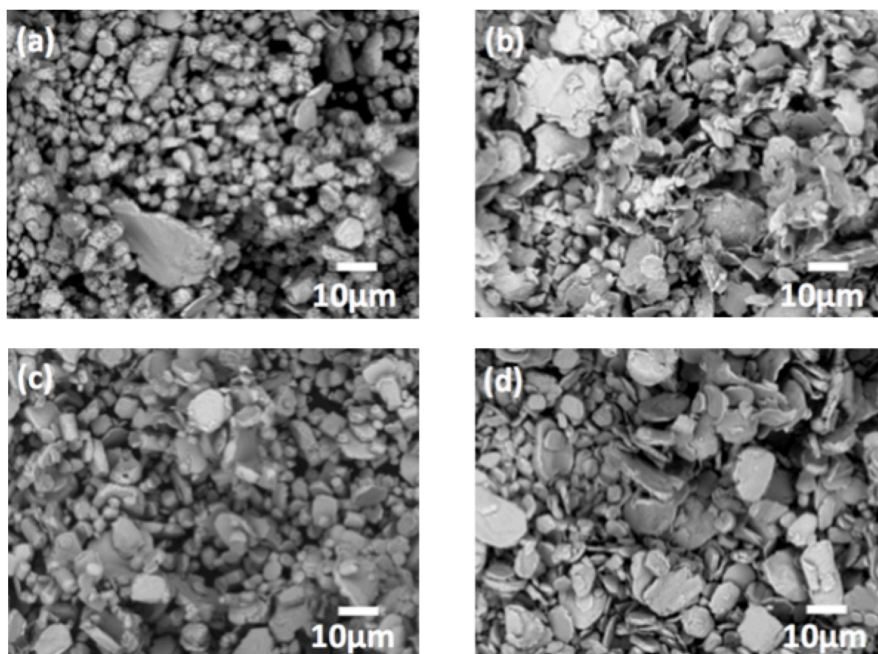


Figure 4.25. Scanning electron microscope images of nickel powder: (a) ball milled with 10mm stainless steel balls for 2 hours; (b) ball milled with 10mm stainless steel balls for 10 hours; (c) ball milled with 10mm stainless steel balls for 2 hours; (d) ball milled with 10mm stainless steel balls for 10 hours.

6 hours; (c) ball milled with 3 mm stainless steel balls for 2 hours; (d) ball milled with 3 mm stainless steel balls for 6 hours (coauthored with Bernard Kim).

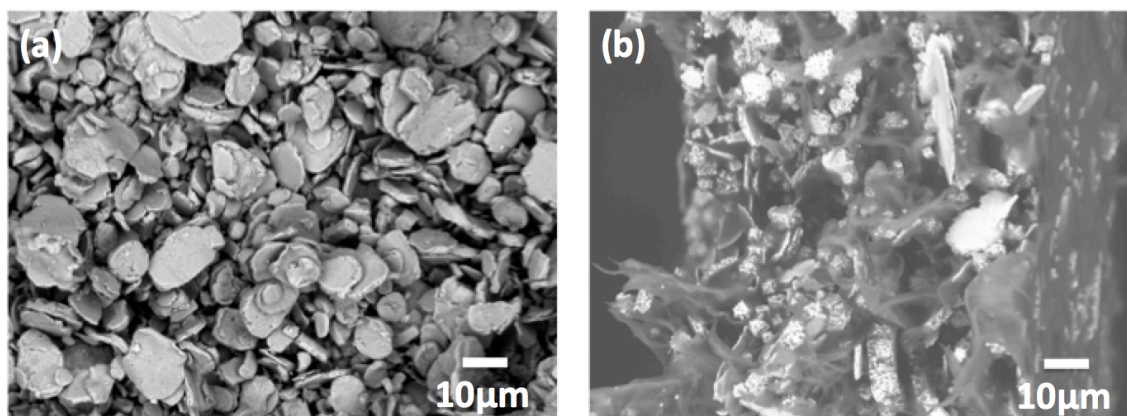


Figure 4.26. Scanning electron microscope images of printed films from PSBR-based nickel composite inks: (a) ball milled with 3 mm stainless steel balls for 6 hours; (b) ball milled with 10mm stainless steel balls for 2 hours (coauthored with Bernard Kim).

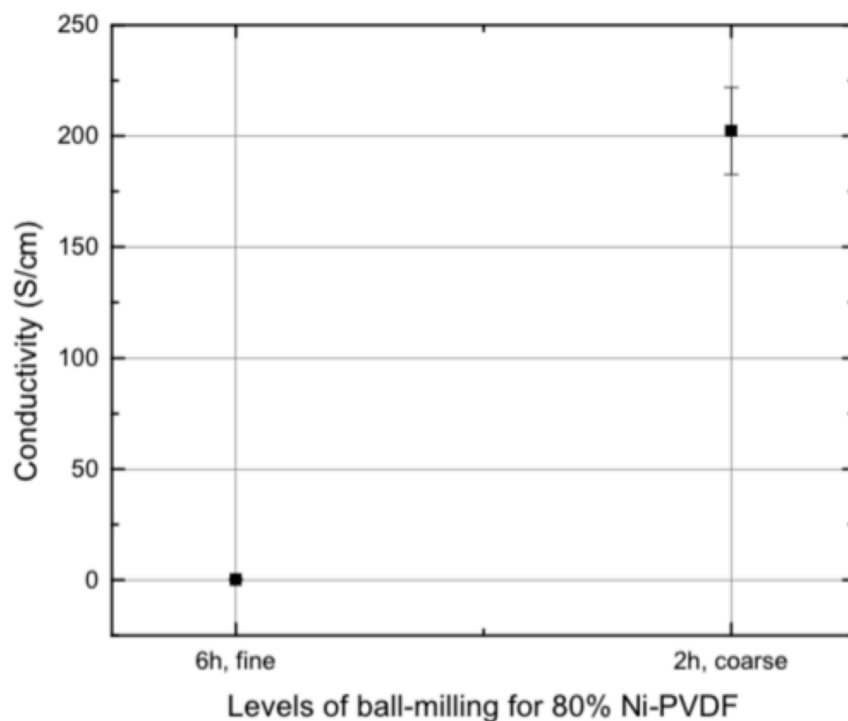


Figure 4.27. Conductivity measurements for films dispenser printed with PSBR-based nickel current collector inks, prepared by ball milling with 3 mm stainless steel balls for 6 hours and ball milling with 10mm stainless steel balls for 2 hours (coauthored with Bernard Kim).

4.8. Chapter Summary and Future Work

Extensive electrochemical characterizations with the flexographically printed PSBR-based composite α -MnO₂ cathode were conducted. Full cells consisting of dispenser-printed electrolytes and zinc foil anodes were assembled. The cyclic voltammetry method was used to study the reversible zinc intercalation through ionic liquid electrolyte into the aqueous-based cathode. Galvanostatic cycling showed that the cell capacity stabilized after about twenty cycles and the capacity varied significantly with discharge current density. Electrochemical impedance spectroscopy measurements revealed the interfacial resistance between the gel electrolyte and zinc foil, as well as the evolution of impedance components through cycling, for a full zinc-based cell system. Coin cells based on zinc/ionic liquid electrolyte/MnO₂ chemistry were made in an argon and then characterized to study zinc-based chemistry performance in this controllable environment. The coin cells showed comparable behavior to batteries printed in the ambient environment. Printable PSBR-based nickel current collector inks have also been developed for an entirely printable zinc-based battery, to conveniently integrate with other electronics on non-conductive, flexible substrates.

Chapter References

- [1] C. C. Ho, J. W. Evans, and P. K. Wright, "Direct write dispenser printing of a zinc microbattery with an ionic liquid gel electrolyte," *J. Micromech. Microeng.*, vol. 20, no. 10, p. 104009, Sep. 2010.
- [2] C. C. Ho, "Dispenser Printed Zinc Microbattery with an Ionic Liquid Gel Electrolyte," *Ph.D. Dissertation*, May 2010.
- [3] A. H. Reidies, *Manganese Compounds*. Weinheim, Germany: Wiley-VCH Verlag GmbH & Co. KGaA, 2000.
- [4] C. Xu, B. Li, H. Du, and F. Kang, "Energetic Zinc Ion Chemistry: The Rechargeable Zinc Ion Battery," *Angew. Chem. Int. Ed.*, vol. 51, no. 4, pp. 933–935, Dec. 2011.
- [5] J. A. Dean, "Lange's handbook of chemistry," Jan. 1985.
- [6] D. A. Steingart, A. Redfern, C. Ho, P. Wright, and J. Evans, "Jonny Galvo: A Small, Low Cost Wireless Galvanostat," *presented at the 208th ECS Meeting*, 2006, vol. 1, pp. 17–22.
- [7] M. S. Wu and P. Chiang, "Electrochemically deposited nanowires of manganese oxide as an anode material for lithium-ion batteries," *Electrochemistry Communications*, vol. 8, issue. 3, pp. 383–388, March 2006.
- [8] D. Qu, "The study of the proton diffusion process in the porous MnO₂ electrode," *Electrochimica Acta*, vol. 49, no. 4, pp. 657–665, Feb. 2004.
- [9] L. Chen, X. Huang, E. Kelder, and J. Schoonman, "ScienceDirect.com - Solid State Ionics - Diffusion enhancement in Li_xMn₂O₄," *Solid State Ionics*, 1995.
- [10] J. R. Scully and D. C. Silverman, "Electrochemical impedance: analysis and interpretation - Google Books," 1993.
- [11] M. E. Orazem and B. Tribollet, "Electrochemical Impedance Spectroscopy - Mark E. Orazem, Bernard Tribollet - Google Books," 2011.

- [12] M. Wakihara, "ScienceDirect.com - Materials Science and Engineering: R: Reports - Recent developments in lithium ion batteries," *Materials Science and Engineering: R: Reports*, 2001.
- [13] C. C. Ho, J. W. Evans, and P. K. Wright, "Direct write dispenser printing of zinc microbatteries," *Technical Digest of PowerMEMS*, 2009.
- [14] C. C. Ho, D. A. Steingart, J. P. Salminen, W. H. Sin, T. M. K. Rantala, J. W. Evans, and P. K. Wright, "Dispenser printed electrochemical capacitors for power management of millimeter scale lithium ion polymer microbatteries for wireless sensors," *Technical Digest of PowerMEMS*, 2006.
- [15] Z. Wang, A. Chen, R. Winslow, D. Madan, R. C. Juang, M. Nill, J. W. Evans, and P. K. Wright, "Integration of dispenser-printed ultra-low-voltage thermoelectric and energy storage devices," *J. Micromech. Microeng.*, 2012, 22, 094001.
- [16] D. Madan, A. Chen, P. K. Wright, and J. W. Evans, "Dispenser printed composite thermoelectric thick films for thermoelectric generator applications," *J. Appl. Phys.*, vol. 109, no. 3, pp. 034904–034904–6, 2011.
- [17] D. Madan, A. Chen, P. K. Wright, and J. W. Evans, "Printed Se-Doped MA n-Type Bi₂Te₃ Thick-Film Thermoelectric Generators," *Journal of Elec Materi*, vol. 41, no. 6, pp. 1481–1486, Jan. 2012.

Chapter 5

Integration of Printable Ultra-low-voltage Thermoelectric and Energy Storage Devices

5.1. Introduction

As discussed in the introduction chapter, the printed battery project was initiated to develop an energy storage solution for wireless sensor network applications. Research related to self-powered wireless sensor systems has emerged in recent years due to a wide range of potential applications [1], including structural health monitoring [2], intelligent transportation systems [3], residential energy management [4], and in-home healthcare systems [5]. Prolific amounts of research have thus been conducted on micro-power energy harvesting techniques including photovoltaic [6], piezoelectric [7] and thermoelectric [8] technologies to replace traditional primary batteries as the power source. However, these energy-harvesting methods, often due to their intermittent nature, can be detrimental to the continuous operation of the wireless sensor systems [9]. To provide a perpetual power source, a cost-effective, integrated energy harvesting system with energy storage capabilities is highly desired [10]. Rechargeable micro-batteries and electrochemical supercapacitors are typical choices for energy storage. The practical integration of such a system is highly dependent on the chosen energy harvesting and energy storage technologies and requires suitable power management solutions [11-13].

In this chapter it is aimed to demonstrate the integration of both dispenser-printed, ultra-low-voltage thermoelectric generators (TEG) [14-15] and rechargeable, zinc-based micro-batteries [16-18], which have both been independently demonstrated in previous works, with a commercial voltage step-up converter circuit. With this proof of concept prototype fabricated at dispenser scale, scaled-up manufacturing utilizing flexographic printing techniques will soon be realized by designing larger scale devices and developing various functional flexographic inks based on printability criteria established in chapter 3.

In the previous work, a 50-couple TEG printed on a flexible polyimide substrate was capable of producing $10.5\mu\text{W}$ at 171.6mV for a 20K temperature difference at matched load resistance [15]. Printed zinc-manganese dioxide microbatteries with gel polymer electrolytes achieved average discharge rates of 1mAh/cm^2 and 1.2mWh/cm^2 between $C/2 - C/7$ [16]. Although the performance of printed thermal energy harvesting and energy storage devices was individually demonstrated, practical applications require integrated DC-to-DC voltage step-up conversion. While low current output ($\mu\text{A}\sim\text{mA}$) from TEGs are sufficient for slowly charging microbatteries, it is always necessary to achieve a voltage output higher than the open circuit voltage of the battery ($1.5\sim 5\text{V}$ depending on the battery type and printed cell numbers). This presents difficulties for dispenser printable small-scale thermoelectric generators at low temperature differences

because device output voltages typically fall within the mV range. Thus, the use of a commercially available voltage step-up DC-to-DC converter (Linear Tech LTC3108) was explored, to charge a printed microbattery using ultra-low power and energy harvested from a printed thermoelectric device. Figure 1 shows a schematic of the components in an integrated system.

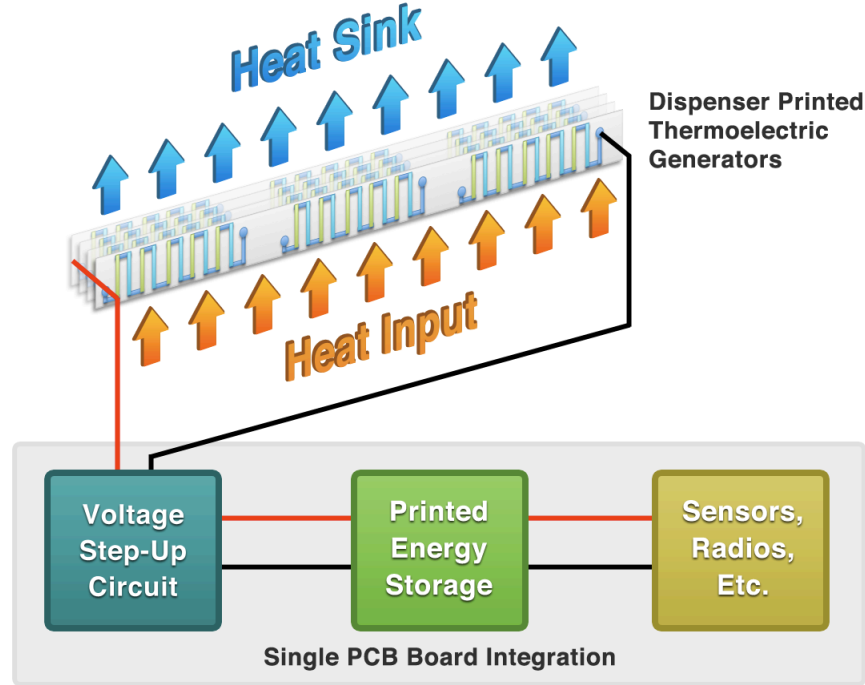


Figure 1. A schematic of printable, low-voltage, thermoelectric energy harvesting and energy storage devices integration (courtesy of Rich Winslow).

5.2. Printed Thermoelectric Devices

5.2.1. Thermoelectric Device Design

Thermoelectric devices are designed based on the widely known Seebeck effect [14-15]. When there is a temperature gradient applied to thermoelectric materials, an open circuit voltage will be generated. Depending on the voltage direction, there are two types of thermoelectric materials: p-type materials with holes as charge carriers and n-type materials with electrons as charge carriers. If the two types of thermoelectric elements are put electrically in-series but thermally in parallel, a high voltage and power generating device is then created. In the past few years, great research efforts in both academia and industry have been made to develop high efficient thermoelectric devices for useful thermal energy conversion.

On the materials side, a dimensionless figure of merit (ZT) is used to evaluate the thermoelectric materials performance as shown in the following equation:

$$ZT = \frac{\alpha^2 \sigma}{\lambda} T \quad (1)$$

where

α represents the Seebeck coefficient;

σ represents the electrical conductivity;

λ denotes the thermal conductivity of the materials;

and T means the average temperature across the materials.

A higher ZT value is achieved; better thermoelectric materials get developed.

On the device sides, traditional thermoelectric devices are typically in 3D array structures, which cause not only its fabrication process highly labor intensive, but also high limitations regarding to the low device array densities as well as low aspect ratios. [14-15] Printed thermoelectric devices with novel planar design solved most of these problems with a scalable manufacturing process. It also opens door to novel devices design and fabrication, for example circular thermoelectric devices, as well as parallel-connected thermoelectric devices for optimized internal resistant and power output. As will be shown, the power output of the device is a function of not only the materials ZT value but also the number of couples/elements and their connections.

All previous thermoelectric devices before were designed with a single type of connection: all thermoelectric couples connected in series [14-15]. Because of the high resistivity with the printable composite materials used in our research, the device thus has very internal resistance (typically 1-5k Ω for a 50 couple device). For battery integration, since the commercially bought DC-to-DC converter is designed as a 2-10 Ω load resistance, the printed thermoelectric generator was redesigned to reduce device resistance to match this load resistance. The reduction in device resistance was achieved by decreasing the number of thermoelectric couples in series and instead placing them in parallel. However, this results in a trade-off between voltage output and device resistance. Figure 2 shows the calculations for this phenomenon for a device consisting of 250 couples given a resistance of 12.5 Ω for a single couple [15]. Varying the number of couples in series, while forming sets of series couples in parallel to achieve 250 total couples, significantly reduces the total internal resistance to match an external load.

Figure 3 demonstrates the optimization of the closed-circuit voltage output (based on a circuit resistance of 4 Ω [19]), number of couples in series, and temperature difference for a printed TEG consisting of 250 total couples. At $\Delta T=20K$, the minimum closed circuit voltage of 20mV for the converter can be achieved for a device consisting of 4 – 20 couples in series. The maximum closed circuit voltage can be achieved for a TEG with 25 parallel sets of 10 couples in series. This design was thus chosen for fabrication and testing. Based on the closed circuit voltage of 28.4mV at $\Delta T=20K$, the power delivered to the converter circuit will be approximately 202.3 μW . Given the circuit conversion efficiency of approximately 35%, the output power after stepping up the voltage will be approximately 70.8 μW . This is sufficient for some state-of-the-art wake-up radios that have an average power consumption of 52 μW [20].

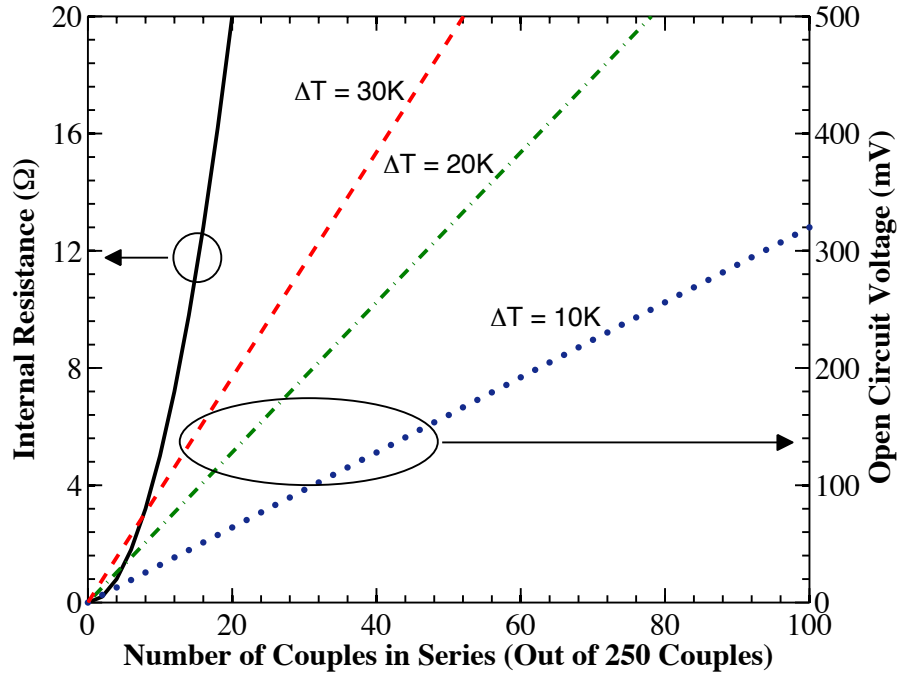


Figure 2. Theoretical calculations showing the trade-off between internal resistance and open circuit voltage. As couples are formed in series, sets of the series couples are placed in parallel to achieve a total of 250 couples.

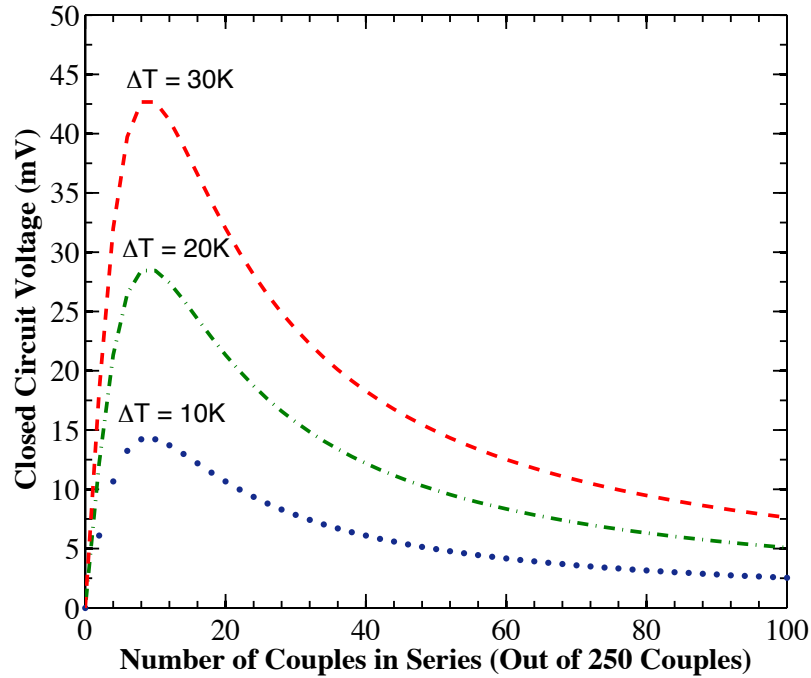


Figure 3. Optimization of the internal connections of the thermoelectric device to achieve the highest closed circuit voltage when connected to the step-up converter.

5.2.2. Experimental

The planar thermoelectric device is fabricated from dispenser printed n-type Bi_2Te_3 and p-type Sb_2Te_3 based polymer composites. Details of the thermoelectric materials and prototype fabrication can be found in [14-15]. A custom-designed, double-layer, flexible printed circuit board (Flex-PCB) was fabricated by PCB Universe, Inc. The flex-PCB consisted of nickel and gold plated copper traces on a flexible polyimide substrate. The elements on the front were connected to the back through vias in the through-thickness direction. The illustration and a photo with both the front and back views of the actual device are shown in figure 4a-b. On each substrate, there are 5 parallel sets of 10 couples in series consisting of 3 mm long elements. This design was chosen to increase voltage generation and reduce device resistance. Five sets of the devices were then stacked and connected in parallel using copper wires through the vias as shown on figure 4c.

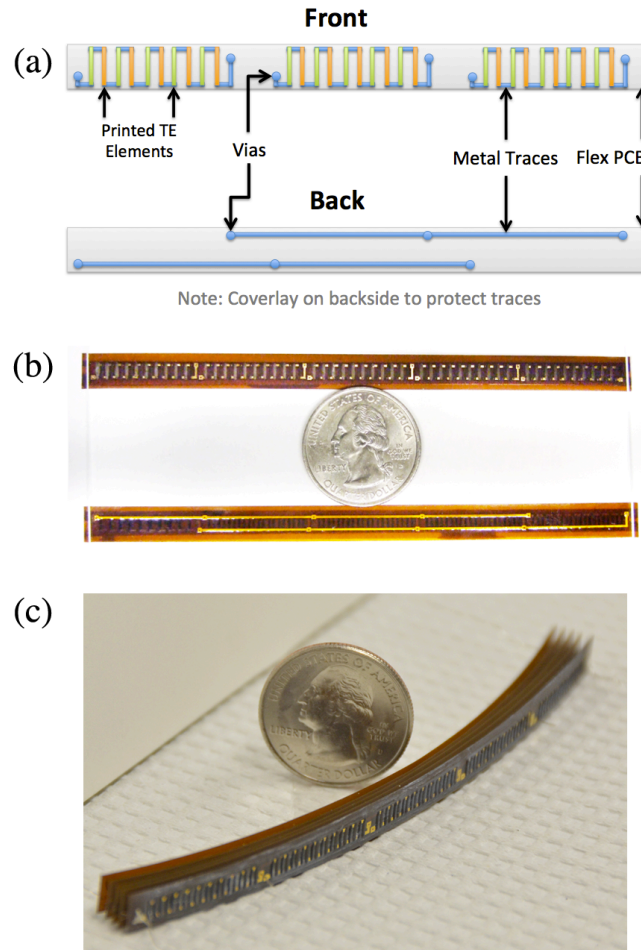


Figure 4. (a) Illustration and (b) photo of printed thermoelectric elements on a Flex PCB substrate. (c) Photo of 5 stacked printed thermoelectric devices in parallel(courtesy of Alic Chen).

5.2.3. Thermoelectric Device Characterization

After the thermometric devices were printed, cured and assembled [14], the performance of the stacked TEG (figure 4c) was characterized using a custom testing apparatus. As shown in figure 5, thermoelectric heater/coolers (9500/127/040 B, Ferrotech Corp.) were mounted onto two aluminum plates to provide surfaces for cooling and heating. The

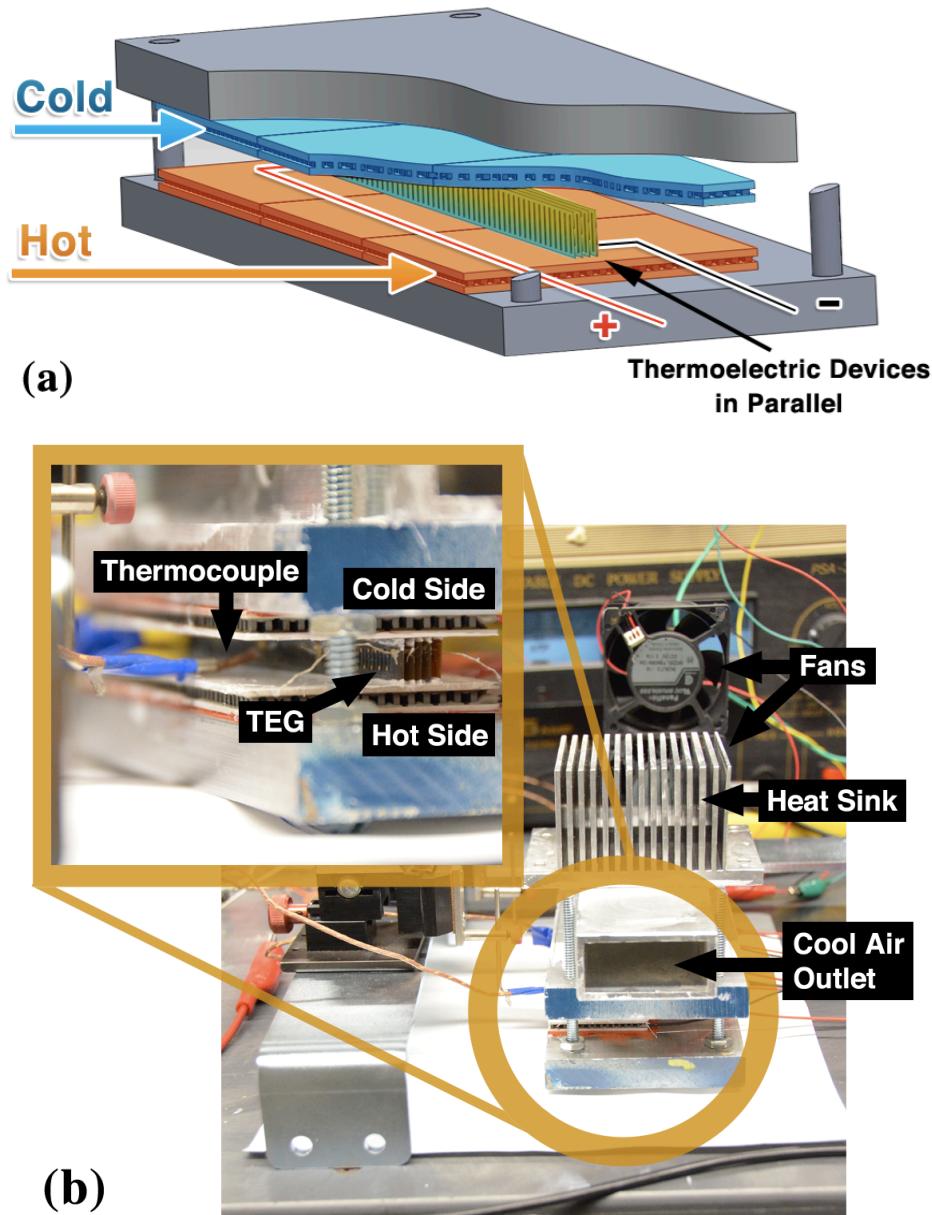


Figure 5. (a) Schematic and (b) photo of a custom built thermoelectric device characterization apparatus. (courtesy of Rich Winslow)

printed TEG was positioned between the plates as a temperature difference was applied across the device. The distance between the two plates was adjusted using screw mounts while the temperatures were monitored using thermocouples. Thermal joint compound (TIM-417, Wakefield Solutions) was applied at the contact interfaces to reduce contact

thermal resistance. Various temperature differences were then applied across the printed TEG. Once the device reached steady state, the open circuit voltage of the device was measured using a digital multimeter (34401A, Agilent Technologies, Inc.). A variable load resistance was then connected in series with the device and voltage measurements were taken at multiple load resistances. The power was then calculated based on the measured voltage and load resistance at various temperature differences. This apparatus was also used for the analysis of the integrated system as later described.

Figure 6 shows the characteristic power curve of the stacked TEG at a temperature difference of 20K. The resistance of each printed set (strip) of thermoelectric devices ranged between 20-24 Ω . The resistance of the stacked device consisting of 5 sets was 4.7 Ω . The maximum power output of the device occurred at matched load resistance, providing a power output of 203.5 μ W at 31.9mV. The power output of this device matches previous models based on characteristics of this materials system [15]. It should be noted that the polyimide borders of the TEG resulted in thermal losses, limiting the temperature difference across the generator. Future work will limit the thickness of the polyimide borders to reduce losses.

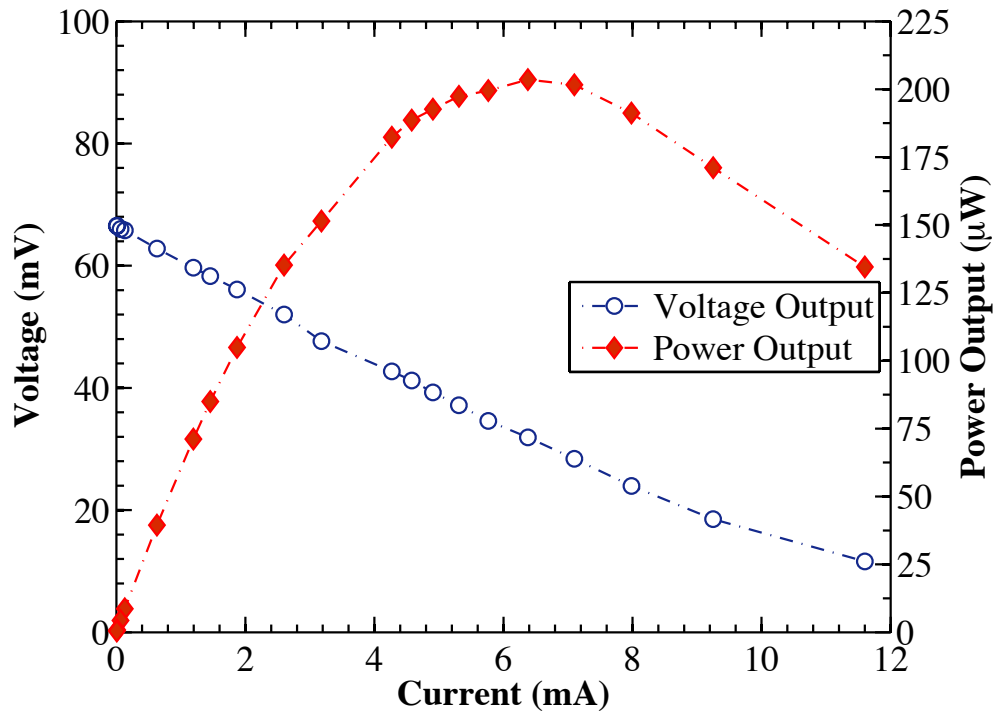


Figure 6. Characteristic curve for the thermoelectric generator with 25 parallel sets of 10 couples in series at $\Delta T = 20$ K.

5.3. Dispenser Printed Micro-Batteries on PCB

5.3.1. Printable Zinc-based Batteries

Previous chapters have been focusing on flexgraphically printed batteries. In this session, the dispenser printed battery chemistry for integration will be briefly introduced. In this

project, a solid-state rechargeable battery was developed consisting of porous electrode materials (zinc and manganese dioxide), separated by a gel polymer electrolyte (GPE). The electrolyte consists of a 1:1 mixture of poly(vinylidene fluoride-hexafluoropropylene) (PVDF-HFP) and 0.5M solution of zinc trifluoromethanesulfonate (Zn+Tf-) salt dissolved in 1-butyl-3-methylimidazolium trifluoromethanesulfonate (BMIM+Tf-) ionic liquid. Both of the zinc and manganese dioxide electrodes are formed with 90 wt% of active materials, 5 wt% of acetylene blacks as well as 5 wt% of PVDF-HFP binders.

5.3.2. Fabrication

Dispenser printing provides a flexible way to fabricate the zinc-based batteries. A variety of substrates can be used for printing including PCBs, thus providing a convenient way for integrating energy harvesting and energy storage systems. Batteries with different patterns can also be designed and printed. A sandwich structure is chosen for its simplicity and large capacity per footprint area. This is due to high surface contact area between each material. Composite inks were first developed for the MnO₂ cathode, gel polymer electrolyte and Zn anode [17] respectively, then printed layer-by-layer via an ink solvent evaporation process between each printing step. A representative cross-section of the printed battery under SEM is shown in Figure 7 [17]. The thickness of a single-layer battery is between 50-100µm. Based on this, multiple layers of batteries can be printed on top of each other to achieve a desired voltage and power output per footprint area thus an efficient utilization of free space on converter PCB is achieved.

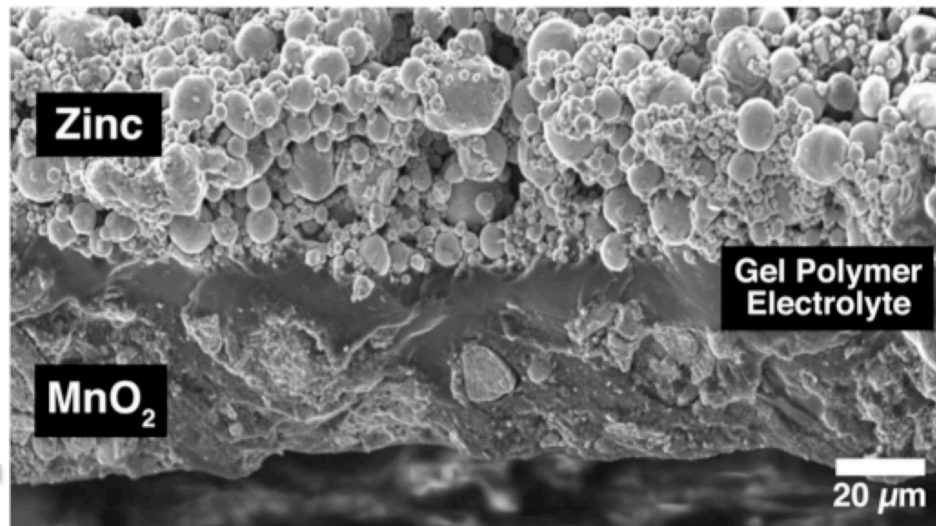


Figure 7. Cross section of the printed battery examined under a scanning electron microscope (SEM) (courtesy of Christine Ho[18]).

5.3.3. Printed Batteries Characterizations

Controlled galvanic charging and discharging tests of the printed batteries were conducted using a custom Ardustat potentiostat/galvanostat [17] [21]. Figure 8 shows the cycling behavior of a printed double-layer battery for integration. The operating voltage ranges from 1V to 3.6V, and the capacity of the battery quickly stabilizes within the first several cycles. The capacity loss in the battery is less than 15% over 30 cycles. At least 70 cycles of stable charging and discharging tested with low losses has been proven.

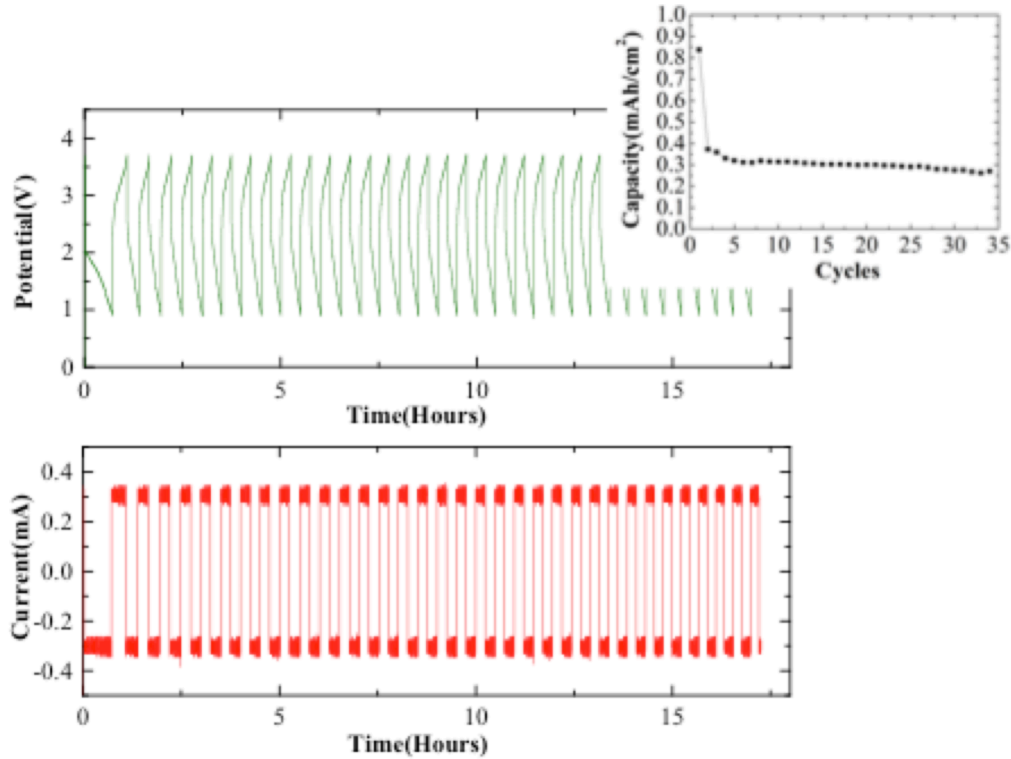


Figure 8. Charge and discharge characterization of a double-layer battery printed in series.

5.4. Integrated Energy Harvesting System

5.4.1. Power Management Introduction

To store the energy harvested from the TEGs in a printed microbattery, a commercial ultra-low-voltage step-up converter circuit (LTC 3108 demo board, Linear Technology Corp.) was used to convert the mV-range voltage input to several volts for charging. The voltage step-up circuit provides four selectable regulated voltage outputs, which are 2.35V, 3.3V, 4.1V and 5V respectively. For charging a single printed Zinc/GPE/MnO₂ battery, a 2.35V output has been selected. The minimum current from this circuit must also be considered due to self-discharging characteristics of the printed battery. For a battery with a footprint area of 1 cm², at least several μ A must be provided for efficient charging. The micro-battery self-discharge rate is still currently being investigated. Both

of the voltage step-up conversion and battery charging/discharging efficiency will be discussed in the following section.

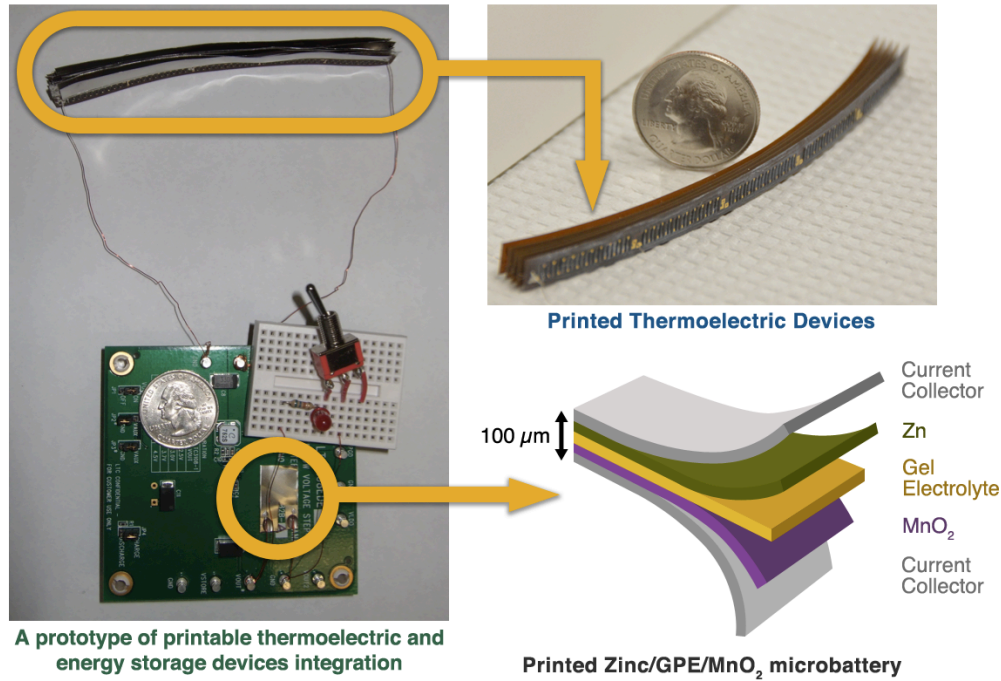


Figure 9. An integrated prototype with a printed thermoelectric device and printed battery on a voltage step-up PCB [18]. A LED was used as the external load for demonstration purpose.

5.4.2. Voltage Step-up Conversion

Prior to charging a printed micro-battery, the efficiency of the voltage step-up circuit was first analyzed for this specific thermoelectric application. Using the thermoelectric testing configuration described in section 2.3, the output of printed TEG was connected to the input of the converter. Next, the output from the converter was connected to various external loads while the voltage across the load was monitored. Figure 10 below shows the output load current and circuit efficiency as a function of load resistance using a printed TEG input with a 20K temperature difference across the elements. The open circuit voltage of the TEG was 65mV while the closed circuit input voltage was 27.1mV at an input current of 4.1mA. The measured closed circuit falls within the range of the estimated closed circuit voltage of 28.4mV as described in section 2.1. The power conversion efficiency reached a maximum of 34% when the external load was 100KΩ. This value matches the expected efficiency of the circuit for this input voltage [19]. The minimum output current was 2μA when the external load was less than 1MΩ. These conversion losses are believed to arise from the operation of the step-up circuit components including the internal capacitors for voltage regulation. The internal resistance of the TEG can be reduced in the future to improve the efficiency. While the power output across a resistive load may be useful for continuous power applications, this

output characterization is not indicative of charging performance of a printed micro-battery. Due to the complex nature of simulating the charging circuitry of a battery, only empirical analysis will be presented in the following section.

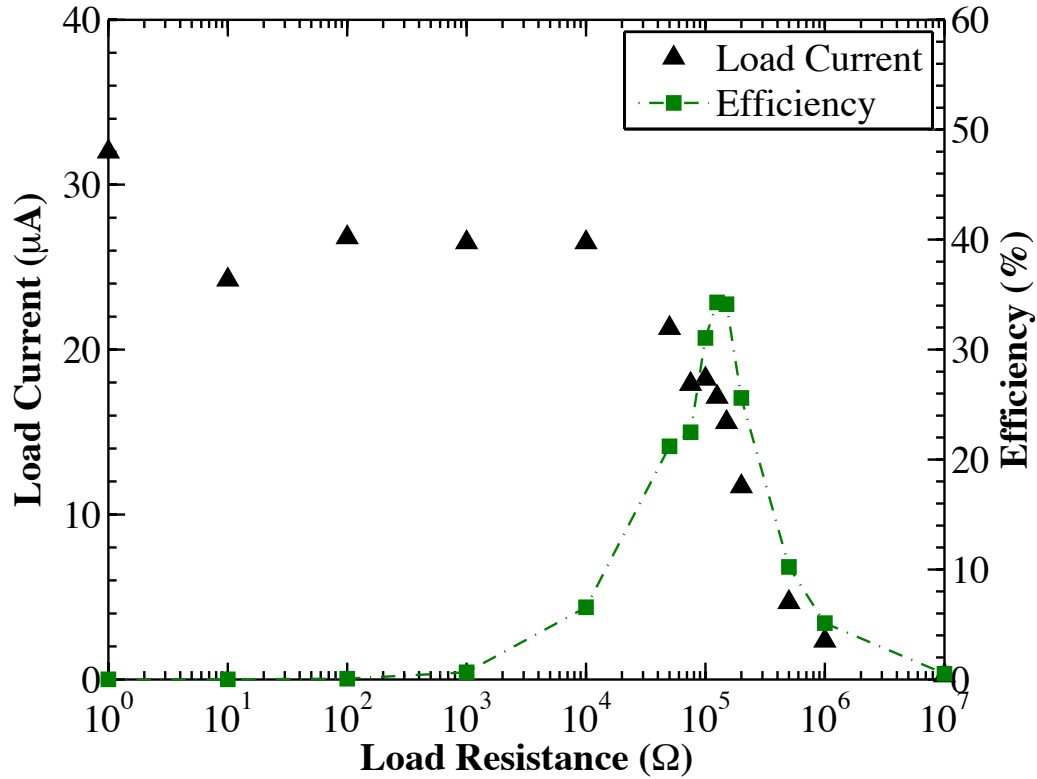


Figure 10. Voltage step-up circuit output current and efficiency at various external load resistances. A printed TEG at a temperature difference of 20K is used as the input to the circuit.

5.4.3. Printed Battery Charging

The voltage regulated power output from the conversion circuit was used to charge a 0.25 cm^2 printed microbattery. Real time charging voltage and current were monitored and recorded using a custom Labview program that controlled a digital multimeter (34401A, Agilent Technologies, Inc.). The battery was first charged from 1.2V to 2V from the converted output of the TEG at an average charging rate of $20 \mu A$ and then discharged at a rate of $30 \mu A$ using an Ardustat. With a controlled temperature difference of 20.3°C , the charging current was maintained at $18 \mu A$, taking 2.5 hours to completely charge the battery. Based on the power input of the TEG, the power conversion efficiency varied between 19.5% and 32.4% corresponding to the voltage level of the battery. Figure 11 shows the combined charge/discharge curves of the battery charged by a TEG and discharged using an Ardustat. The charge/discharge rate and charging time of this battery gives a charge efficiency of 67%. Charging losses likely occurred from the charging process, while the Coulombic efficiency of the printed battery have also played a role.

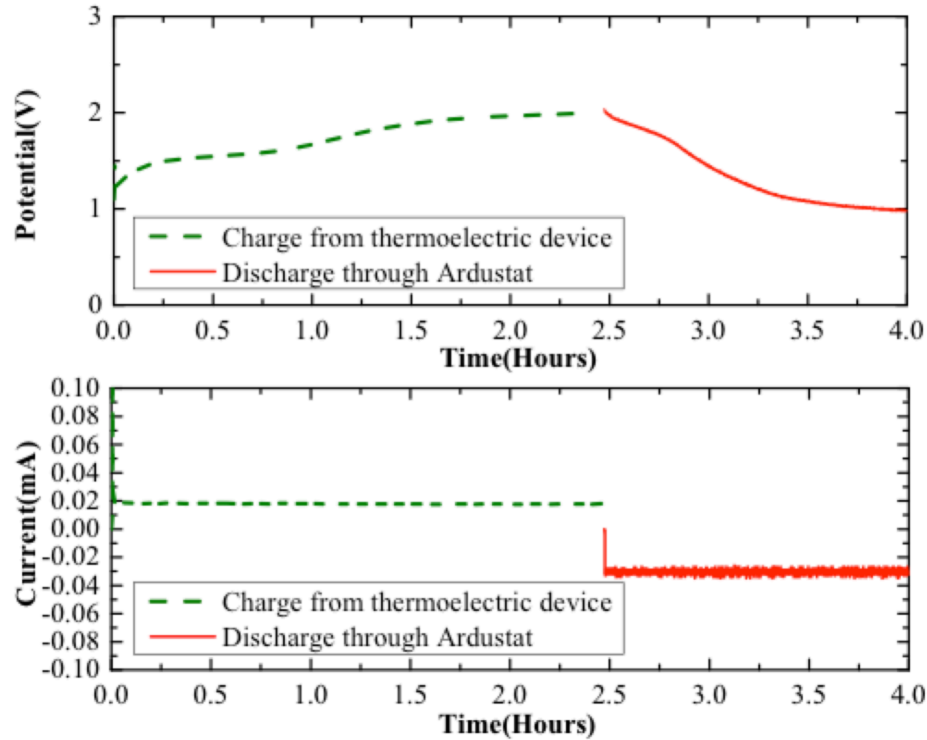


Figure 11. Combined curves of printed battery charging from printed thermoelectric device and discharging through Ardustat.

5.5. Chapter Summary and Future Work

This chapter reported on an integrated energy-harvesting prototype that consists of dispenser-printed thermoelectric energy harvesting and electrochemical energy storage devices with a commercial voltage step-up converter. Parallel-connected thermoelectric devices with low internal resistances were designed, fabricated and characterized. The use of a commercially available DC-to-DC converter was explored to step-up a 27.1mV input voltage from a printed thermoelectric device to a regulated 2.34V output. The voltage step-up circuit efficiency reached as maximum of 32.4% during the battery charging process while the battery charging efficiency was approximately 67%. The prototype presented in this work demonstrates the feasibility of deploying a printable, cost-effective and perpetual power solution for practical wireless sensor network applications. The work of this chapter has been published on Journal of Micromechanics and Microengineering by IOP Publishing.

Future work will include further optimization of parallel thermoelectric devices for reduced thermal losses, application-oriented custom DC-to-DC converters and smart packaging of the integrated energy harvesting system. A scaled up manufacturing by developing flexographic or advanced coating inks for both two devices and circuits would be attractive, because this could potentially lead to a roll-to-roll, entirely printable, self-rechargeable power source solution for all kinds of novel wireless sensor

applications. Further integration with printed sensor systems for various condition monitoring and printed electronics for power management will be the next step.

Chapter References

- [1] E. P. James et al., "An investigation of self- powered systems for condition monitoring applications," *Sens. and Actuators, A*, 2004, 110 171-176.
- [2] J. Wilson et al., "A wireless sensor network and incident command interface for urban firefighting," *Mobile an Ubiquitous Systems: Networking& Services, 2007, MobiQuitous 2007. 4th Annual Int Conf* 1-7.
- [3] M. Tubaishat et al., "Wireless sensor networks in intelligent transport systems," *Wireless Communications and Mobile computing*, 2009, pp. 287-302.
- [4] N. Ota et al., "An application –driven architecture for residential energy management with wireless sensor networks," *Mobile Adhoc and Sensor Systems (MASS), 2006 IEEE International Conference* 1-17.
- [5] A. Milenkovic et al., "Wireless sensor networks for personal health monitoring: issues and an implementation," *Computer Communications*, 2006, 29, pp. 2521-2533.
- [6] A. Nasiri et al., "Indoor power harvesting using photovoltaic cells for lower-power applications," *IEEE Transactions on Industrial Electronics*, 2009, 56, pp. 4502-4509.
- [7] Y. C. Shu and I. C. Lien, "Analysis of power output for piezoelectric energy harvesting systems," *Smart Materials and Structures*, 2006,15, pp.1499-1512.
- [8] I. Startk, "Thermal energy harvesting with thermo life," *Wearable and Implantable Body Sensor Networks, BSN 2006, International Workshop on* 19-22.
- [9] S. Beeby et al., *Energy Harvesting for Autonomous Systems* (Artech House)
- [10] A. Kansalet al. "Power management in energy harvesting sensor networks," *ACM Transactions on Embedded Computer Systems (TECS)- Special Section LECTES'05*, 6, pp. 1-38.
- [11] P. B. Koeneman, I. J. Busch-Vishniac, K. L. Wood, "Feasibility of micro power supplies for MEMS," *J. Microelectromech. Syst.*, 2007, 6, pp. 355–62.
- [12] J. N. Harb, R. M. LaFollette, and L. L. Howell, "Microbatteries for self-sustained hybrid micropower supplies," *J. Power Sources*, 2002, 104, pp. 46–51.
- [13] N. J. Guilar et al., "Integrated solar energy harvesting and storage," *Vary Large Scale Integration Systems, IEEE Transactions on*, 2009, 17, pp. 627-637.
- [14] D. Madan, A. Chen, P. K. Wright, J. W. Evans, "Dispenser printed composite thermoelectric thick films for thermoelectric generator applications," *J. Applied Physics*, 2010, 109, 034904 (6pp).
- [15] A. Chen, D. Madan, P. K. Wright, J. W. Evans, "Dispenser-printed planar thick film thermoelectric generators," *J. Micromech. Microeng.*, 2011, 21, 389698 (8pp).
- [16] C. C. Ho, D. A. Steingart, J. W. Evans, and P. K. Wright, "Tailoring Electrochemical Capacitor Energy Storage Using Direct Write Dispenser Printing," *ECS Transactions*, 2008, 16 (1), pp. 35-47.

- [17] C. C. Ho, K. Murata, D. A. Steingart, J. W. Evans, and P. K. Wright, "A super ink jet printed zinc-silver 3D microbattery," *J. Micromech. Microeng.*, 2009, 19, 094013 (5pp).
- [18] C. C. Ho, J. W. Evans, and P. K. Wright, "Direct write dispenser printing of a zinc microbattery with an ionic liquid gel electrolyte," *J. Micromech. Microeng.*, 2010, 20, 104009 (9pp).
- [19] Linear Technology, *Ultralow Voltage Step-up Converter and Power Manager*, (22pp).
- [20] N. M. Pletcher, S. Gambini and J. Rabaey, "A 52 μ W wake-up receiver with -72 dBm sensitivity using an uncertain-IF architecture," *IEEE J. of Solid-state Circuit*, 2009, 44, pp. 269-280.
- [21] D. A. Steingart, A. Refern, C. C. Ho, J. W. Evans, P. K. Wright, "Jonny Galvo: a small, low cost wireless galvanostat," *ECS Trans.*, 2006, 1, pp. 17-22.

Chapter 6

Discussion and Future Outlook

6.1. Printability

- Anilox roller with larger cell volume: Current flexographically printed cathode films, through one single print utilizing an anilox roller with 15BCM engraved cell volume, had an average thickness of 9 μ m. Therefore multiple prints on one substrate with alignments were needed to achieve the desired film thickness. Utilizing anilox rollers with larger cell volume (up to 70BCM) and different cell shapes would likely address this issue.
- Manufacturing process optimization: Besides the functional ink properties, the printing process parameters significantly influenced the final printing quality. Design of experiments to investigate the effects of the pre-printing, printing and post-printing variables on the precision and repeatability of the roll-to-roll battery manufacturing are worth exploring.
- Slurry electrolyte: Primary research in this thesis was focused on flexographically printing the MnO₂ cathode, Zn anode and Ni current collectors, which are essentially all slurry inks. The ionic liquid electrolyte is a solution instead without solid particles dispersing through it. During flexographic printing, a low pressure or shear stress was able to easily destroy the solution structure and squeeze the solution everywhere on the printing substrate. Adding inert particles (e.g. Alumina) with an optimized amount would form “slurry electrolyte”, which has the potential to make electrolyte printable. The inert particle ratio would enable further optimization of the electrochemical performance, such as ionic conductivity of the electrolyte.
- Hybrid printing and coating process development: To address the issue of gel electrolyte and multi-layer battery printing, a combined printing/coating method in future research could be the potential solution. In roll-to-roll equipment, slot-die coating stations or screen-printing stations can be conveniently integrated with flexographic printing stations for a full device fabrication.

6.2. Electrochemistry

- Fundamental mechanism of zinc ion intercalation into MnO₂: Research was conducted based on electrochemical characterization methods such as cyclic voltammetry, electrochemical impedance spectroscopy and galvanostatic cycling to provide insight into the storage process of zinc ions into MnO₂ cathode. Further research on characterizations of the film materials at different stages of the reaction would be valuable to a deeper understanding about the cathodic reaction mechanism. X-ray diffraction (XRD) and X-ray photoelectron spectroscopy (XPS) measurements are recommended.

- Zinc-based coin cell optimization: The current zinc-based coin cell performance was based on characterizations of cells made from cathode and electrolyte inks, respectively with one single formulation in inert argon environment. Further research on coin cell making and characterizations to find optimized electrodes and electrolyte compositions would be important. Coin cell performance in different working environments (e.g. extremely high and low temperatures) and operating conditions (e.g. high and low c-rate) as well as cell self-discharge behavior would be of great value.

6.3. Applications

- Integration with photovoltaic cells: Research on integration of printable zinc-based batteries and thermoelectric energy harvesting devices were conducted to develop a perpetual power source for wireless sensor network applications. For grid energy storage application demonstration, an integration of the printed battery with a small photovoltaic device (preferable also printable solar cell based on silicon or CIGS inks) would be of good value. Potential integration could be done in dispenser, ink-jet, screen-printing, or even roll-to-roll flexographic printing scale.